Optical readout of single spins for quantum computing and magnetic sensing

im Fachbereich Physik der Freien Universität Berlin eingereichte Dissertation

Rolf Simon Schönfeld

Mai 2011

Betreuer / Erstgutachter:	Dr. W. Harneit
2. Gutachter:	Prof. Dr. U. Alexiev
3. Gutachter:	Prof. Dr. J Wrachtrup

Disputationsdatum: 17.10.2011

Zusammenfassung (German abstract)

Die Fähigkeit, den Quantenzustand einzelner Spins in Festkörpern gezielt zum manipulieren und zu detektieren ermöglicht eine Vielzahl von neuen und faszinierenden technologischen Anwendungen von Nanosonden bis hin zur Quanteninformationversarbeitung. Am Beispiel des Stickstoff-Fehlstellen Defektzentrums in Diamant sind in den letzten Jahren eine großen Zahl von bahnbrechenden Experimenten durchgeführt worden, unter anderem Verschränkung von bis zu drei Qubits, Einzelschuss-Detektion von Kernspinzuständen, selektives Auslesen zweier gekoppelter Zentren und Messungen von magnetischen und elektrischen Feldern mit Nanometerauflösung mit viel versprechender Empfindlichkeit, welche in einigen Fällen die Möglichkeiten der meisten bekannten Techniken übersteigt. Bislang konzentrieren sich aber nahezu alle Experimente auf Defektzentren, welche sich tief im Innern des Diamanten befinden. Dies ist insbesondere bei Nanosonden, aber auch mit Blick auf Skalierbarkeit und den elektronischen Zugriff auf die Quanteninformation von Nachteil. Diese Arbeit konzentriert sich auf Defektzentren, welche sich nur wenige Nanometer unter der Oberfläche des Diamanten befinden. Bei diesen sind die Eigenschaften des Zentrums stark von seiner Umgebung beeinflusst. Im Rahmen der Arbeit wurden einzelne Spins bei Raumtemperatur gezielt kohärent manipuliert und deren Zustand mit Hilfe optisch detektierter magnetischer Resonanzspektroskopie durch ein Konfokalmikroskop detektiert. Das Dephasierungsverhalten und die Phasenrelaxationszeit der Spins wurden untersucht und die primären Dekoheränzquellen ermittelt. Weiterhin wurden die Einflüsse von Wasser, Umgebungsatmosphäre und paramagnetischen Molekülen auf die Kohärenz und Detektierbarkeit von Spins in Nanodiamanten untersucht, sowie Methoden der Entkopplung der Spins von ihrer Umgebung mittels externer Magnetfelder und einer Reihe von "Dynamic Decoupling" (dynamische Entkoppungs-) Pulssequenzen. Zusätzlich wurden Kopplungen an benachbarte Kernspins sowie an paramagnetische Moleküle auf der Oberfläche mittels Doppel Elektron-Elektron Resonanz nachgewiesen.
Anhand eines Stickstoff-Fehlstellen Defektzentrums in einem Nanodiamand haben wir weiterhin den weiterentwickelte Deutsch-Jozsa Algorithmus durchgeführt.
Zum Abschluss präsentieren wir eine neuartige technologische Umsetzung zur Messung magnetischer Felder in Echtzeit mittels eines einzelnen Defektzentrums. Bei Testmessungen von externen Feldern und ortsaufgelösten Messungen an einem magnetischen Mikrodraht wurden Empfindlichkeiten von einigen $\mu\mathrm{T}/\sqrt{\mathrm{Hz}}$ festgestellt.

Abstract

The ability to measure and manipulate the quantum state of a single spin in a solid state system opens up a broad range of powerful applications ranging from nano probes to quantum information processing. Over the past few years, a number of ground breaking experiments have been conducted on paramagnetic nitrogen vacancy defect centers in diamond, including up to 3-qubit entanglement, single-shot-readout of a nuclear spin, selective access of two coupled centers and magnetic, electric and thermographic sensing at the nanoscale with promising properties in some cases exceeding most currently known techniques. Yet, almost all of the experiments conducted so far focus on centers deeply buried in the diamond, which is undesirable especially for sensing applications, but also in terms of scalability and electronic access to the information. In this work we focus on the spin physics of centers only few nanometers below the surface, where the unique properties of the center are strongly influenced by the external environment. We coherently manipulated and detected single spins at ambient temperature by combining optically detected magnetic resonance with single molecule spectroscopy using a confocal microscope. We measured the spin dephasing behavior and the phase relaxation time and examined the primary sources of decoherence. Furthermore, we observed effects of water, atmosphere and paramagnetic molecules on the coherence and readability of spins in nanodiamonds and demonstrated ways to preserve the coherence using external magnetic fields and a number of different dynamic decoupling pulse sequences. In addition, we measured couplings to proximal nuclear spins by continuous wave spectroscopy and to molecules on the surface by double electron electron resonance. Also, we demonstrate execution of the refined Deutsch-Jozsa algorithm on a nitrogen vacancy center in a nanodiamond. Finally, we propose new technological approach for realtime measurements of magnetic fields using a single spin in diamond. In test measurements using external fields and spatially resolved measurements of the field from a magnetic microwire a sensitivity of a few $\mu\mathrm{T}/\sqrt{\mathrm{Hz}}$ was achieved.

Contents

Chapter 1

Introduction

1.1 Zero-dimensional quantum systems

Since the first optical observation of single molecules [1, 2] and single point defects ("quantum dots") in solids [3] in the late 80's observation of the physical properties of zero-dimensional structures has gained considerable interest in various studies of fundamental physics. The development of new techniques like quantum transport [4, 5], single ion/atom traps [6, 7] and optical microcavities [8] and considerable increases in sensitivity of existing techniques open new fascinating possibilities in future applications. Today commercial applications of quantum dots already include light emitting diodes [9], commercial single photon sources for quantum communication, quantum well lasers [10] and fluorescent markers for single molecule spectroscopy [11]. Yet, until now only optic and electronic properties of zero-dimensional systems have been used. In addition to single defect/molecule optics also single spins are of substantial interest. For example, the use of the well-understood physics of spin dynamics can be exploited in a scalable electron spin quantum computer. Although the first proposal of such a computer dates back to the early 80's [12, 13] and experimental proof-of-principle experiments using liquid nuclear magnetic resonance (NMR) [14–19] have been performed in the late 90's, a commercial, scalable version based on solid state nanostructures seems to be out of reach until today. The wide variety of different physical systems discussed as promising building blocks of a future quantum computer include quantum dots in Gallium arsenide [20, 21] and Silicon [22, 23], single nuclei in solid matrices (e.g ^{29}Si in ^{28}Si [24]), trapped ions [25–27] and neutral atoms [7], optical and infrared photons [28] and superconducting circuits [29, 30]. However, none of these systems can fulfill all of the criteria that Di'Vincenzo formulated in 2000 [31] (see section 1.2). These criteria are by consensus deemed necessary for a successful implementation of scalable quantum logics. Moreover, all these approaches require extensive

cooling at least to helium temperature, which, while not representing a technological barrier that cannot be overcome, is still undesirable for broad technical application. In particular, this makes an affordable home version of a quantum computer very unlikely.
In the case of electron spins, the primary reason for cooling lies in their small Zeeman energy. Quantum applications require a substantial spin polarization, which can thermally only be achieved in the sub-Kelvin temperature range. In addition, in solid state systems interaction with optical phonons are one of the major limitations to coherence, which have to be frozen. Thus, for many years, a room temperature access of single spins seemed nothing but a dream.

1.2 Quantum information processing

The strength of quantum computing arises from the usage and perfect control of the dynamics of a set of isolated quantum states. In analogy to a classical bit which binary information can be the "0" or "1" a two level quantum system is referred to as quantum bit (qubit). In contrast to its classical counterpart its state is expressed by the more general form

$$\Psi = \alpha \,|\, 0\rangle + \beta \,|\, 1\rangle \qquad ,$$

where α and β are complex numbers fulfilling the normalization condition

$$\alpha^2 + \beta^2 = 1 \qquad .$$

From this representation it can be seen that any superposition of the eigenstates $|\, 0\rangle$ and $|\, 1\rangle$ of the qubit is also a valid state, although a "strong" measurement of the qubit will immediately result in projection of the qubit into one of its eigenstates. Considering multiple qubits the general laws of quantum mechanics allow the system to form so-called entangled states. These are states which can no longer be expressed by a tensor product of states of the individual qubits forming the system. Operating on entangled states allows execution of logical gates on a much more complex system than just a number of defined bits. Using an easy analogy this can be viewed as operating on many different states at once, which is referred to as quantum parallelism. Today, a number of quantum algorithms which exploit this phenomenon have been proposed, the most prominent being the Deutsch-Jozsa algorithm [32, 33], Shor algorithm [34] and Grover algorithm [35].
In order to reliably create and preserve entangled states, a high coherence (phase control) of the whole quantum system is required, which provides one of the major challenges in the technical realization of quantum computing. David Di'Vincenzo [31] formulated a set of conditions that have to be fulfilled for a quantum system in order to be a candidate for a quantum computer:

1. It must be possible to scale the system up to a deliberately large number of well defined qubits.

2. Initialization of the system into a pure state (e.g. $|00000\ldots\rangle$) is required.

3. The system needs a sufficiently long decoherence time.

4. The system needs an universal set of quantum gates for complete quantum control (e.g. full single qubit control plus CNOT gates).

5. Any qubit can be selectively measured.

Since the proposal of quantum error correction by P. Shor [36], which theoretically allows for infinitely long computation if it is possible to detect and correct errors during operation, the second, third and fifth criterion can be further qualified. It is commonly understood that the decoherence time has to be long enough for application of quantum error correction. On the other hand, not only single qubit but single-shot readout (reliable measurement of the state within its own longitudinal relaxation time) is required to be able to detect errors during the computation. Furthermore, initialization of the auxiliary qubits used for error correction must be possible "on-demand", i.e. at any time during the computation.

1.3 The nitrogen vacancy center in diamond

The nitrogen-vacancy (NV) center is a paramagnetic defect in diamond consisting of a substitutional nitrogen atom next to a vacancy at a regular carbon lattice site. Given the strict requirements for a scalable quantum computer, the electron spin of the NV center represents an extraordinarily well-suited candidate for a quantum bit, since it provides fast and efficient spin initialization by optical pumping [37], as well as readout [38] and coherent manipulation [39] by optically detected magnetic resonance (ODMR). This is combined with very low spin-lattice-relaxation [40] and high phase coherence [41], which is superior even to many low-temperature systems considered as qubits. The primary reasons for this auspicious confluence of favorable properties are due to the unique properties of diamond, namely the combination of extreme hardness (10^4 kg/mm^2), large band gap (5.45 eV), and very low nuclear spin density (98.9 % ^{12}C) [42]. This is why the NV center today matches all required conditions for use as a qubit in a scalable quantum computer. Currently, single spin readout [38], coherent manipulation approaching the quantum error correction threshold [39], spatially controlled single defect creation [43], up to 3-qubit entanglement [44], spin-light coherence [45], single shot readout of a nuclear spin [46] and selective access of two coupled centers [47] have been demonstrated experimentally. Still, the design of a scalable computer proves most

challenging in fabrication, e.g. perfectly controlled single ion implantation might be necessary.
One way to overcome such problems is to build multiple small sub-computers containing few qubits and couple them using photon transfer via optical cavities [48, 49] or plasmons [50]. In such a building block, also molecular components with well defined and desirable properties like the endohedral fullerene $N@C_{60}$ might play a significant role. Moreover, some of these access schemes (i.e. plasmons) require the center to be very close (a few nm) to the diamond surface. Up to now, most experiments have been performed on NV centers deeply buried within the diamond. It has to be expected that shallow centers might suffer from coherence losses due to the imperfect environment. In addition, it is already known that stress leads to a modification in the symmetry of the centers [51]. This results in a change of its physical properties, for example a reduction of the ODMR contrast caused by mixing of spin states. In very small nanodiamonds which are only a few nm in size, even unstable luminescence (blinking) of centers and uncontrolled change of their charge state has been observed [52]. In order to continue on the road to success laid out for the nitrogen vacancy qubit, it is essential to learn more about the physics underlying these effects.

1.4 Magnetic sensing

From the viewpoint of quantum information science, any effect of the environment on a single qubit that cannot be controlled represents a perturbation of the system that has to be avoided. But the opposite view is true as well: if one has a well defined local qubit that will interact with its surroundings, this qubit represents an ultra sensitive probe of that environment. In consequence, new schemes of single qubit readout are often related to a new way of high-resolution sensing. A good example is the superconducting quantum interference device (SQUID) based on a Josephson junction [53], that can be used as a superconducting qubit [29, 30] as well as for measurement of very small currents and magnetic fields [54, 55]. In a similar way, the spin of the NV center can also be used for sensing small magnetic fields. The physical law underlying the measurement principle is the Zeeman interaction, which splits the electron spin sub-levels by an energy proportional to the strength of the magnetic field at the location of the spin. The single spin magnetometer was first proposed by P. Berman [56] in view of the first experimental results in electron paramagnetic resonance (epr) exhibiting single spin sensitivity. With the NV center in diamond recently a system has been found [57, 58], that, in theory provides not only an even better sensitivity [41, 59, 60] than SQUIDS [61], but does so at ambient temperature, which is particulary important for biological sensing. In addition, the size of the NV center (about one diamond lattice constant [62]),

which determines the spatial resolution, is definitely much smaller than a SQUID could ever be.

1.5 Overview and structure of the thesis

This work is separated into five chapters, where some can be read isolated from the content of the others, while some are directly related to each other.
The physical properties of the nitrogen vacancy center in diamond and the single spin ODMR technique are described in chapter 2, where the most fundamental basics of the whole work are introduced.
In chapter 3 we describe the sources of decoherence in nanodiamonds and introduce the concept of dynamic decoupling. Experimental results on nitrogen vacancy centers in nanodiamonds are presented.
The effects of the environment on the nitrogen vacancy center, in particular paramagnetic molecules on the diamond surface are investigated in chapter 4.
In chapter 5 the theoretical basis and experimental realization of the refined Deutsch-Jozsa algorithm on a single nitrogen vacancy center is described.
Finally, in chapter 6 we introduce scanning-probe imaging of magnetic fields using a field-frequency lock on a single spin. Experimental results on the performance of single nitrogen vacancy centers in nanodiamonds are presented and discussed.
A complete summary and conclusions of this work including a short outlook will be given in chapter 7.

Chapter 2

The nitrogen-vacancy center in diamond

2.1 Optical properties of the charged nitrogen-vacancy center in diamond: the origin of the ODMR effect

The nitrogen-vacancy (NV) center is one of more than 500 defects known in diamond [63]. Due to a band gap of 5.45 eV, perfect diamond is highly transparent in the infrared and visible range [64]. Defects (color centers) are responsible for a large variety of colors in diamond. The NV center is a point defect of C_{3v} symmetry that consists of a substitutional nitrogen atom adjacent to a carbon vacancy (see Fig. 2.1). Two stable charge states are known, the neutral NV^0 center exhibiting a zero phonon line (ZPL) at 575 nm and the negatively charged NV^- center having its ZPL at 637 nm [65] (see figure 2.2). Both centers are paramagnetic. The NV^0 has a $S = \frac{1}{2}$ ground state while the NV^- ground state is $S = 1$. Since not only the ground state but also the excited state energy lies within the band gap and since the centers are localized within a few lattice constants, most properties of the center can be well described by quasi-atomic theoretical treatment and molecular orbital (MO) theory [67–69]. Furthermore, ab-initio calculation of the center has been reported [70]. In addition, electronic properties of the NV center were described in a full analytic molecular model very recently [71], which helps understanding the effect of strain and imperfect crystal structure. Still, many properties of the center can be understood using a much simpler picture. In the simplest model, only 5 electrons (6 in the charged case) have to be considered, 3 resulting from the dangling bonds of the nearest neighbor carbon atoms at the vacancy and 2 paired electrons originating from the nitrogen atom. This model

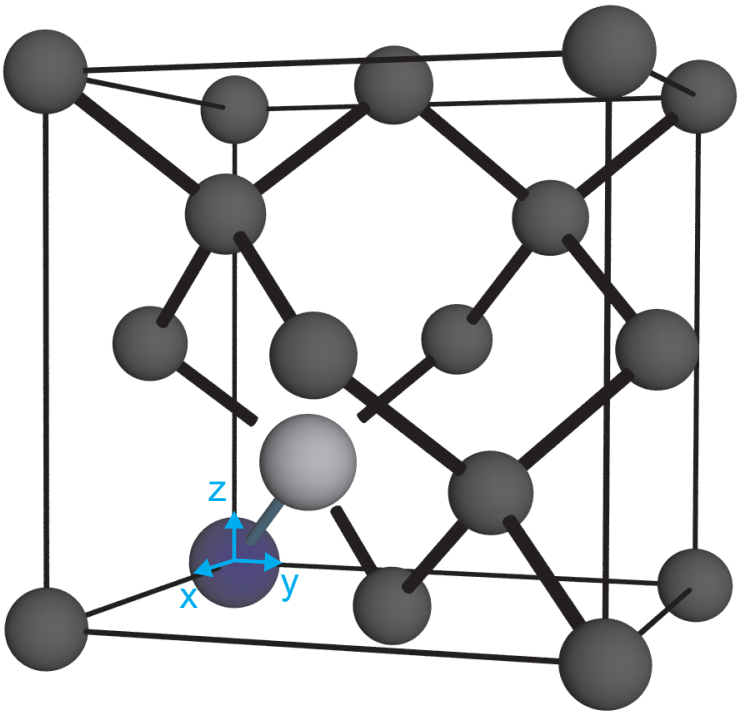

Figure 2.1: Structure of the nitrogen vacancy center in the diamond lattice. Blue: nitrogen atom at regular carbon location. White: vacancy at regular carbon location. Black: carbon atoms. The center is oriented along the ⟨111⟩ axis.

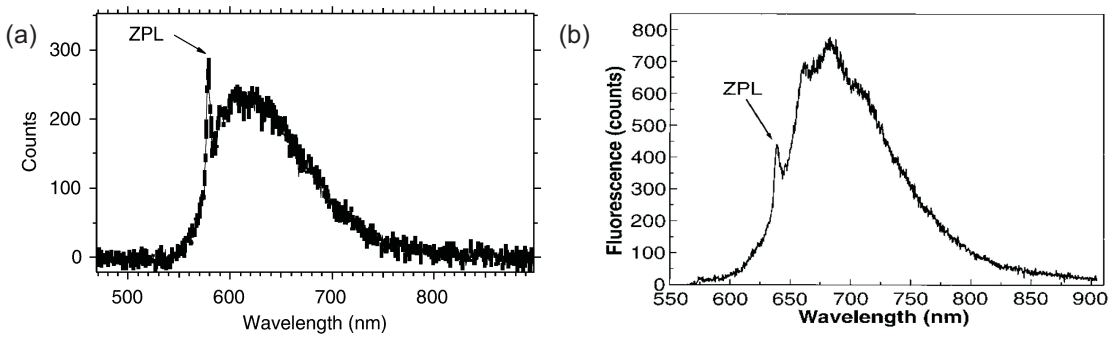

Figure 2.2: Luminescence spectra of (a) NV^0 [66] and (b) NV^- [38] recorded at room temperature. The zero phonon line (ZPL) of the NV^0 is located at 575 nm, while for the NV^- it is redshifted to 637 nm.

can describe most electronic properties of the ground state and excited state, but fails to describe the origin of some most interesting features, e.g. spin projection-dependent inter-system crossing (ISC) into one or more meta-stable singlet levels that can be used to polarize and read out the electron spin. While both charge states can be converted into each other using optical excitation [72, 73] and environmental changes [66, 74–77] the present work exclusively focusses on the charged NV^-. The ground state forms a $^3A_2$ triplet while the lowest lying optically excitable state forms a $^3E_2$ triplet [78]. The spin degeneracy of the triplet states is lifted by zero-field splitting, which is uniaxial corresponding to the center symmetry. However, external strain like in the case of nanodiamonds and near-surface defects can reduce the symmetry and induce an additional parameter to the spin-spin interaction tensor responsible for zero-field splitting [51, 79]. The lowest lying singlet level is located in energy between the two triplet states. However, there are still some questions open regarding the nature of this state and the order of the energy levels of the singlet states. A recent study of infrared absorption and emission of center indicates a system of two states with ^1E and ^1A character between the triplet states [80] (see Fig. 2.3). Direct optical excitations from ground state to one of those states are forbidden and deexcitation from the lowest lying singlet state to the ground state is non-radiative. However, there is experimental evidence that the transition between the two singlet levels is radiative and infrared light is emitted exhibiting a ZPL at 1042 nm [80].

2.2 Dynamics and steady state under continuous wave double resonance excitation

The ODMR effect, which describes the strong difference in luminescence dependent on the projection of the spin along the zero-field splitting axis (z) can be understood qualitatively by considering that the optical excitation and emission inside the triplet system conserves S_z to an high extent, while at the same time a highly S_z-dependent inter-system crossing towards at least one longer living singlet level is possible. At steady state laser irradiation, this will eventually lead to a strong spin polarization, which effectively increases the emission rate, because it reduces the probability to enter the metastable singlet level.

In order to explain and analyze the continuous wave ODMR effect on a quantitative basis one can simplify the full term diagram shown in Fig. 2.3 to a 5-level model (see fig. 2.4) and find the equilibrium state under constant excitation by solving the rate equations for the occupation probability of the levels. A simple model that neglects spontaneous spin-lattice relaxation ($T_1 \to \infty$), thermally in-

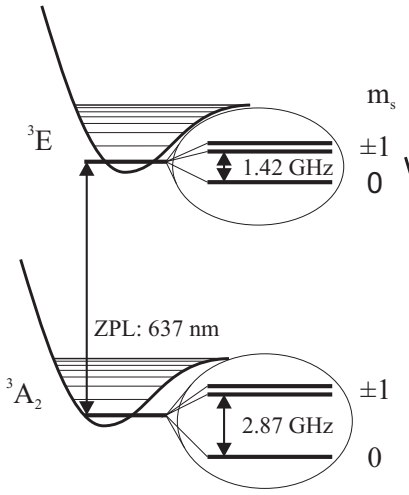

Figure 2.3: Jablonski diagram of the NV^- center showing the triplet ground and first excited state as well as the known singlet levels. In addition, the electrostatic potential and vibronic sub-levels are displayed to define the zero phonon line (ZPL) using the Franck-Condon principle. The spin sub-levels are enlarged in proportion to the optical energies.

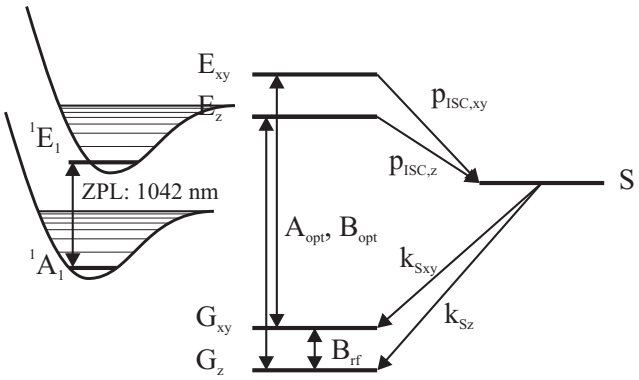

Figure 2.4: Simplified diagram related to a 5-level model. A, B are the Einstein coefficients for spontaneous emission and stimulated absorption/emission of the allowed optical and spin transitions, p_{ISC} are the intersystem crossing probabilities and k_S are the decay constants of the metastable singlet level S.

duced transfer of population from the singlet system back to the excited state, and excitation of forbidden optical transitions results in the equations given in 2.1 for the population of the ground state G, the excited state E, and the singlet state S.

$$\begin{aligned}
\dot{G}_z &= -\left(\rho_{\mathrm{L}} B_{\mathrm{opt}} + \rho_{\mathrm{rf}} B_{\mathrm{rf}}\right) G_z + \left(A_{\mathrm{opt,z}} + \rho_{\mathrm{L}} B_{\mathrm{opt}}\right) E_z + \rho_{\mathrm{rf}} B_{\mathrm{rf}} G_{xy} + k_{Sz} S \\
\dot{G}_{xy} &= -\left(\rho_{\mathrm{L}} B_{\mathrm{opt}} + \rho_{\mathrm{rf}} B_{\mathrm{rf}}\right) G_{xy} + \left(A_{\mathrm{opt,xy}} + \rho_{\mathrm{L}} B_{\mathrm{opt}}\right) E_{xy} + \rho_{\mathrm{rf}} B_{\mathrm{rf}} G_z + k_{Sxy} S \\
\dot{E}_z &= -\left(A_{\mathrm{opt,z}} + \rho_{\mathrm{L}} B_{\mathrm{opt}} + p_{\mathrm{ISC},z}\right) E_z + \rho_{\mathrm{L}} B_{\mathrm{opt}} G_z \\
\dot{E}_{xy} &= -\left(A_{\mathrm{opt,xy}} + \rho_{\mathrm{L}} B_{\mathrm{opt}} + p_{\mathrm{ISC},xy}\right) E_{xy} + \rho_{\mathrm{L}} B_{\mathrm{opt}} G_{xy} \\
\dot{S} &= -\left(k_{Sxy} + k_{Sz}\right) S + p_{\mathrm{ISC},xy} E_{xy} + p_{\mathrm{ISC},z} E_z
\end{aligned} \tag{2.1}$$

Here $A_{\mathrm{opt,\ xyz}}$ and B_{opt} refer to the Einstein coefficients of the optical transitions between the respective levels while B_{rf} refers to the Einstein coefficient for

induced transitions between the spin levels of the ground state. $\rho_{\mathrm{L,rf}}$ is the radiation density of the incident laser and microwave field, respectively. p_{ISC} and k are the inter-system crossing rate and inverse singlet lifetime, respectively.
The approximation $A_{\mathrm{rf}} = 0$ is reasonable considering that T_1 is very long in diamond (more than 1 s at room temperature [41]). Also optical excitation of the metastable state can be neglected, yet one should note that this can induce systematic errors at higher laser power. While thermal repopulation of the excited triplet state does occur at room temperature with a rate of 1 MHz[81], at continuous optical excitation this cannot be distinguished from inter-system crossing and optical re-excitation via the ground state. In order to find the occupation probability at steady state condition one has to set all equations to zero. In addition, the normalization condition

$$A_z + A_{xy} + E_z + E_{xy} + S = 1 \tag{2.2}$$

has to be fulfilled. To further simplify the analytic result one can use that $k_{\mathrm{Sxy}} \approx k_{\mathrm{Sz}} := k$, $A_{\mathrm{opt,z}} \approx A_{\mathrm{opt,xy}} := A_{\mathrm{opt}}$ (13 ns vs. 23 ns [82]) and $p_{\mathrm{ISC},z} \ll p_{\mathrm{ISC},xy}$ (12 kHz vs. 4 MHz [40]).

All remaining physical parameters in this equation can be accessed experimentally, but vary slightly between individual centers, especially in the case of imperfect crystals exhibiting internal strain. A_{opt} and k can be determined for single centers by measuring the second order autocorrelation function $g^{(2)}(t)$ (see, e.g. [83]). They are related to the antibunching and bunching time constants at low excitation power. Additionally, p_{ISC} can also be determined from the bunching time in the limit of very high excitation power [83]. $\rho_{\mathrm{rf}} B_{\mathrm{rf}}$ can be derived from Rabi nutation experiments[1] (see section 2.4.4) and $\rho_{\mathrm{opt}} B_{\mathrm{opt}}$ can be determined by optical saturation experiments or power broadening of ODMR lines. In case of a monochromatic source it is also given by the laser power times absorption cross section σ of the center at given wavelength, divided by the spot area. At the diffraction limit one gets

$$\rho_{\mathrm{opt}} B_{\mathrm{opt}} = \frac{P_L \sigma}{\pi \left(\frac{\lambda}{2}\right)^2} \quad . \tag{2.3}$$

The absorption cross section is however also dependent on the orientation of the center. Thus, a representative independent variable is given by the number of photons within the cross section, or the relative laser power P/P_S, where P_S is the saturation power.

[1] Note that the Rabi frequency is *not* equivalent to the excitation rate since the latter describes the *non-coherent* regime.

inverse radiative lifetime	A_{opt}	80 MHz	*this work*
inverse singlet lifetime	k	33 MHz	*this work*
inter-system crossing rate	p_{ISC}	4 MHz	[84]
absorption cross section at 532 nm	σ	10^{17} cm^2	[85]

Table 2.1: Physical parameters of the NV^- center

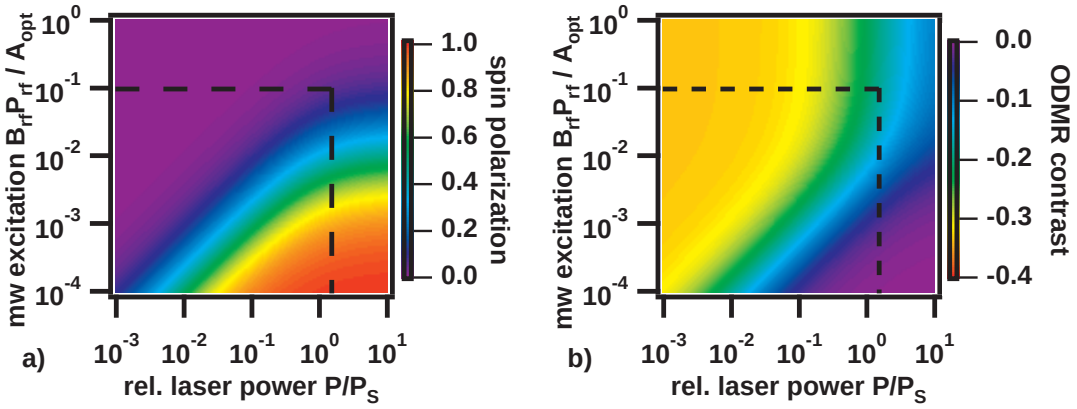

Figure 2.5: Calculated spin polarization (a) and ODMR contrast (b) dependence on microwave and laser power. The dashed lines mark the experimental range of the setup described in section 2.4

Solving the equations we find for the spin polarization of the ground state at given microwave and laser excitation

$$\frac{G_z - G_{xy}}{G_z + G_{xy}} = -\frac{\rho_{\mathrm{L}} B_{\mathrm{opt}} p_{\mathrm{ISC}}}{4A_{\mathrm{opt,z}}\rho_{\mathrm{rf}} B_{\mathrm{rf}} + \rho_{\mathrm{L}} B_{\mathrm{opt}}(4\rho_{\mathrm{rf}} B_{\mathrm{rf}} + p_{\mathrm{ISC}}) + 4\rho_{\mathrm{rf}} B_{\mathrm{rf}} p_{\mathrm{ISC}}} \quad . \tag{2.4}$$

The result using physical parameters from table 2.2 is shown in figure 2.5a. It can be seen that, at negligible microwave excitation, close to perfect spin polarization of the center can be realized at high laser power, which is indeed experimentally observed [37]. This efficient polarization process is an important key to the observation of a single spin at room temperature, since at thermal equilibrium the spin state population difference is only 0.05 %.

The second property required for spin readout is a difference in the luminescence intensity of the different spin levels. The spontaneous emission from the center is determined by the excited state population times A_{opt}. The stimulated emission is usually experimentally invisible in continuous wave experiments since it appears at the same wavelength as the excitation light and is typically blocked by a longpass filter. The absolute difference in spontaneous emission between

on-resonance and off-resonance is given by

$$\left([E_{xy} + E_z]_{\rho_{\mathrm{rf}}=0} - [E_{xy} + E_z]_{\rho_{\mathrm{rf}}\neq 0} \right) A_{\mathrm{opt}} \quad . \tag{2.5}$$

At zero microwave excitation one finds for the luminescence

$$[E_{xy} + E_z]_{P_{\mathrm{rf}}=0} A_{\mathrm{opt}} = \frac{A_{\mathrm{opt}} \rho_{\mathrm{L}} B_{\mathrm{opt}}}{A_{\mathrm{opt}} + 2\rho_{\mathrm{L}} B_{\mathrm{opt}}} \quad . \tag{2.6}$$

This is consistent with the theoretical expectations for $p_{\mathrm{ISC}} = 0$. Under resonant microwave excitation the luminescence is given by a more complicated term. The analytic result for the luminescence under microwave excitation as well as an expression for the relative ODMR contrast is listed as appendix A. The calculated magnitude of the ODMR contrast using the mentioned physical parameters is graphically shown in figure 2.5.

As a result, we are now able to compare power-dependent experimental data

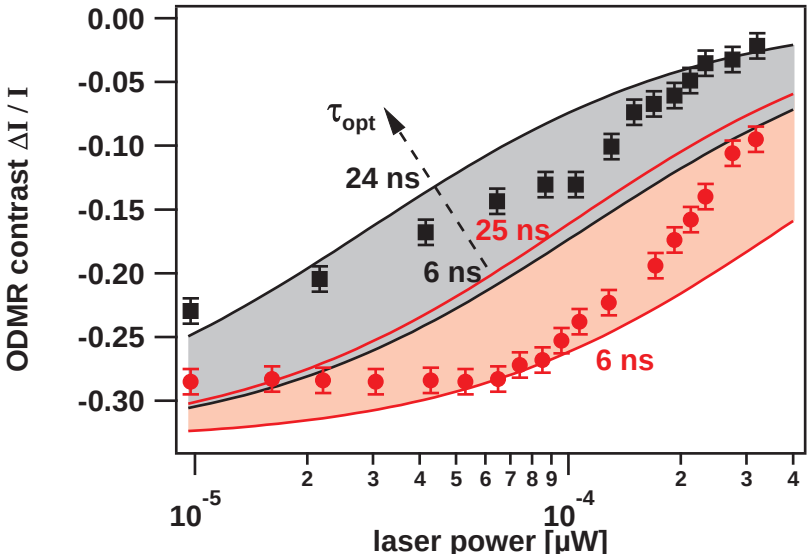

Figure 2.6: Dependence of ODMR contrast on optical and microwave excitation power. Red (lower traces): 30 dBm output power ($\nu_{\mathrm{Rabi}} = 2.7$ MHz). Black (upper traces): 20 dBm output power ($\nu_{\mathrm{Rabi}} = 810$ kHz). The shaded areas mark the calculated contrast within the range of observed values of the fluorescence lifetime, which was not measured for this center.

with our model. Figure 2.6 shows the dependence of the ODMR contrast on the laser and microwave excitation power at resonance frequency. The power was varied using optical and rf attenuators. Unfortunately not all physical parameters

were accessible for the particular center investigated, since autocorrelation measurements were not available. Still, one can plot the theoretical predictions of the model for the whole range of parameters typically observed. It was observed that the fluorescent lifetime seems to have the most important effect and varies strongly between different centers (we observed $\tau_{opt} = 6 \ldots 33\,\mathrm{ns}$).
While the experimental data lie within the range of values that can be described by the model, there are some deviations. First, it is observed that the model predicts a maximum ODMR contrast of 35 % at low laser power, while actually no more than 30 % was experimentally observed. This can be attributed to relaxation processes, e.g. spin-lattice relaxation, which prevent effective spin polarization at very low excitation power. Note that in nanodiamonds T_1 is much shorter than predicted for bulk diamond (at the order of $10^{-4}\,\mathrm{s}$, for details see section 3.1.3). Furthermore it is observed that the ODMR contrast decreases more strongly at high laser power than predicted. This deviation can be explained by excitation of forbidden transitions and lifetime reduction of the excited levels due to non-radiative processes that have not been accounted for in our model.
In conclusion, we have introduced a simple model which is able to describe the observation of spin polarization and ODMR quite accurately for optical excitation within one order of magnitude around the saturation power. Predictions from the model can be used to find a convenient "set point" for an ODMR experiment that offers maximum contrast and photon output. In addition, it is also possible to to deduce transition rates from power-dependent measurements, which was not shown in this particular case, since without parallel measurement of the second order autocorrelation function the system still contains too many dependent variables. Another important conclusion that can be gained from our results is that a single shot readout of the electron spin is not possible via this method, since even under optimal conditions the ODMR contrast cannot exceed 35 %, although the spin is almost completely polarized. Thus, optical destruction of the spin information by re-polarization is faster than readout by photon detection, though recently it has been shown experimentally, that by exploiting nuclear spin levels the contrast can be enhanced by a factor of 2 [84].

2.3 Spin properties of the charged nitrogen-vacancy in diamond

The full Spin Hamiltonian of the ground state of a charged NV center isolated from its environment in an external field reads

$$\mathbf{H} = \vec{S}\mathbf{D}\vec{S} + \vec{B}\mathbf{g}_e\mu_B\vec{S} + g_N\mu_N\vec{B}\vec{I} + \vec{S}\mathbf{A}\vec{I} + \vec{I}\mathbf{Q}\vec{I} \quad . \tag{2.7}$$

Here, $\vec{S}$ and $\vec{I}$ are the electron and nitrogen nuclear spin, respectively. Note that the orbital angular momentum of the ground state is quenched [51] so that spin-orbit coupling has no influence on the spin dynamics and can be neglected. The first term expresses the zero-field splitting induced by spin-spin exchange interaction. It becomes nonzero for $S \geq 1$ and broken spherical symmetry. For $S = 1$ the zero-field splitting tensor $\mathbf{D}$ can be expressed in the principal axis system by two parameters D and E.

$$\mathbf{D} = \begin{pmatrix} \frac{1}{3}D + E & 0 & 0 \\ 0 & \frac{1}{3}D - E & 0 \\ 0 & 0 & -\frac{2}{3}D \end{pmatrix} \tag{2.8}$$

At low fields ($\ll 0.1$T) the Hamiltonian is dominated by this interaction since the C_{3v} (axial) symmetry results in a strong zero-field splitting of $D = 2.87$ GHz between $|0\rangle$ and the $|\pm 1\rangle$ states. The latter are close to degenerate ($E = 0$) in the absence of crystal strain. The next two terms in equation 2.7 express the electron and nuclear Zeeman interaction. The only nuclear spin which is always present resides on the nitrogen nucleus, and is typically $I = 1$ for ^{14}N with 99.6% abundance. The hyperfine interaction with this nucleus defined in the fourth term is nearly isotropic [43]

$$\mathbf{A} = \begin{pmatrix} A_\perp & 0 & 0 \\ 0 & A_\perp & 0 \\ 0 & 0 & A_\parallel \end{pmatrix} \approx 2.2\text{MHz} \qquad \begin{matrix} A_\parallel = 2.4\text{MHz} \\ A_\perp = 2.1\text{MHz} \end{matrix} \tag{2.9}$$

revealing a nonzero electron spin density at the nitrogen site. The anisotropic part arises from a small contribution of dipolar spin-spin interaction. The final term in the Hamiltonian is attributed to the existence of a quadrupole interaction in the nucleus. This was found to be 5.04 MHz [86]. When driving allowed electron paramagnetic resonance transitions obeying the selection rule ($\Delta m_S = \pm 1$, $\Delta m_I = 0$) the quadrupole term is constant and can be ignored.
The physics underlying low field optically detected electron paramagnetic resonance (epr) experiments on single spins is very similar to the one known from common epr but for four substantial differences:

1. In randomly oriented centers (e.g. in nanocrystals) the orientation of the magnetic field is usually not perpendicular to the main quantization axis given by the crystal axis. Moreover, the magnetic field is not parallel to the microwave propagation vector ($\vec{k}$), thus the condition $\vec{B}_1 \perp \vec{B}_0$ is not given. Any discrete nuclear or electron spin present in the near surrounding of the center will further complicate the geometric situation since dipolar coupling between the spins is dependent on their orientation.

2. Another consequence of randomly aligned small magnetic fields is that close to zero field the Zeeman energy may not be proportional to the magnetic field. In addition a magnetic field might influence the size of the ODMR effect since it creates mixing between the $\mathbf{S}_x$, $\mathbf{S}_y$ and $\mathbf{S}_z$ states [87, 88].

3. Since the spin system observable in ODMR is $|\mathbf{S}_z|^2$ no free induction decay (FID) or Hahn echo can be observed. However, phase-dependent information can be obtained by introducing an additional $\frac{\pi}{2}$ microwave pulse at time t before detection. Sweeping this pulse in time can completely reconstruct the echo, but multiple measurement cycles are needed to obtain this information.

4. In contrast to ensemble measurements, inhomogeneous magnetic fields and microwave power distribution will not have any effect on a single localized spin. The presence of "inhomogeneous line broadening" and "spin dephasing" has to be explained by uncertainty of the precession frequency due to slow random fluctuations of the local field. Averaging over multiple experimental cycles at slightly different frequencies will result in a comparable effect. This effect can be eliminated in an analogous way, e.g. by spin echo experiments.

In the next paragraph we will focus on these differences while for basic spin physics we have to refer to the standard epr textbooks [89–92].

The condition $\vec{B}_1 \perp \vec{B}_0$ usually allows transformation of the system into the rotating frame. This is the typical way to solve the Bloch equations which describe spin motion under influence of non-static magnetic fields. In addition to an external magnetic field B_0 also internal fields contribute to the local effective field. For example, local fields can be induced by another spin, like in the case of hyperfine or zero-field splitting. In the special case of zero external field only the internal components remain. Neglecting relaxation the Bloch equations can be written:

$$\frac{d\vec{M}(t)}{dt} = \gamma \vec{M}(t) \times \vec{B}(t) \tag{2.10}$$

Without loss of generality we assume that static magnetic field points along the z axis and B_1 is modulated along an arbitrary direction in the x-z plane (e.g. linear polarized waves). The sum of static and modulating (microwave driven) magnetic field gives

$$\vec{B}(t) = \vec{B}_{loc} + \vec{B}_1(t) = \begin{pmatrix} 0 \\ 0 \\ B_{loc} \end{pmatrix} + \begin{pmatrix} B_{1x}(t) \\ 0 \\ B_{1z}(t) \end{pmatrix} = \begin{pmatrix} B_1 \cos\phi \cos(\omega t) \\ 0 \\ B_{loc} + B_1 \sin\phi \cos(\omega t) \end{pmatrix} . \tag{2.11}$$

The angle ϕ defines the deviation from perpendicular symmetry. From this expression it can easily be seen that the modulated field can always be separated into a perpendicular and a parallel component. Thus, transformation into the rotating frame and separating the linear polarization into two circular polarized waves results in

$$\vec{B}(t) = \begin{pmatrix} B_1 \cos\phi \cos(2\omega t) \\ B_1 \cos\phi \\ B_{loc} + B_1 \sin\phi \sin(2\omega t) \end{pmatrix} \tag{2.12}$$

This gives rise to a static B_1 component perpendicular to z which drives spin transitions, a fast oscillating component (at twice the Larmor frequency) that is usually neglected because it is too fast for being observed and a non-static field component along the z axis coming from the non-perpendicular field alignment. As long as the condition $B_1 \ll B_0$ is fulfilled (or in other words in the case of zero field, as long as the Rabi frequency does not exceed the Larmor frequency of the spin transition in question) this component also results in no observable effect since fast Larmor frequency fluctuations will be averaged to zero. Thus the only effect to be taken care of is that the driving frequency (Rabi frequency) depends on an effective microwave field

$$B_{1,\text{eff}} = B_1 \cos(\phi) \qquad , \tag{2.13}$$

and can in worst case become zero for centers aligned perpendicular to the $\vec{k}$ vector.

Aside from the necessity of an additional $\frac{\pi}{2}$ "detection" pulse there is only one important difference between observing $|\mathbf{S}_z|$ and the rectangular spin projections $\mathbf{S}_x$ and $\mathbf{S}_y$. When applying nonselective microwave pulses driving both transitions the nutation frequency behaves differently. Usually, a reduction of the Rabi frequency by a factor of $\sqrt{2}$ due to the spin-1 hamiltonian is expected. Instead, by measuring the absolute of $\mathbf{S}_z$, one will observe a frequency which is increased by a factor of $\sqrt{2}$. This is due to the fact that we cannot distinguish between $|\, m_S = 1\rangle$ and $|\, m_S = -1\rangle$ states, which both give a minimum in luminescence, thus twice the frequency is observed when driving both transitions. The presence of additional spins will be discussed in detail in section 2.5.1 and section 3.1.1, and is a substantial part of our experimental studies.

2.4 ODMR measurements on individual NV^- centers in nanodiamond

2.4.1 Nanodiamond sample preparation

For most experiments, we used high temperature high pressure (HTHP) nanodiamonds of type Ib with a size distribution between 0 and 50 nanometers (mean diameter 25 nm, Microdiamant MSY). Diamond of type Ib includes a high amount of nitrogen (up to 500 ppm) and structural defects, and hence the formation of nitrogen vacancy centers is very likely. Still, only some of the particles contain a center and the probability of observing multiple centers in the same diamond is small. This allows observation of single centers using optical techniques if the nanodiamonds are dispersed on a surface so that their average distance is much larger than the optical wavelength.
In order to prepare such a pattern a highly diluted suspension of nanodiamonds in water was dispersed onto a glass plate using a spin coating device. The glass plate was cleaned using a multiple step procedure of solvents, acid and/or plasma etching (see table 2.2) in order to reduce the luminescent background as well as to terminate the glass surface by hydrophilic groups.

After this treatment, 50 μl of the nanodiamond suspension were dropped onto the glass substrate and, after a 20 second waiting period for settling, spincoated for 5 seconds at 100 revolutions per minute (rpm), then one minute at 5000 rpm. Figure 2.7a shows an atomic force microscope (AFM) image of the dispersed nanodiamonds while figure 2.7b shows the corresponding confocal fluorescence image. The bright spots are single NV centers, which was verified measuring the second order autocorrelation function $g^{(2)}(\tau)$ of the incoming photons. (see Fig. 2.7c). For an ideal single photon emitter, only one photon can be emitted at a time,

procedure	**agent**	**duration**
ultrasonic bath	acetone	10 minutes
ultrasonic bath	ethanol	10 minutes
ultrasonic bath	methanol	10 minutes
plasma etching	argon	10 minutes (optional)
plasma etching	oxygen	10 minutes
	or	
chemical etching	hydrofluric acid (1 %)	1 minute

Table 2.2: glass substrate treatment

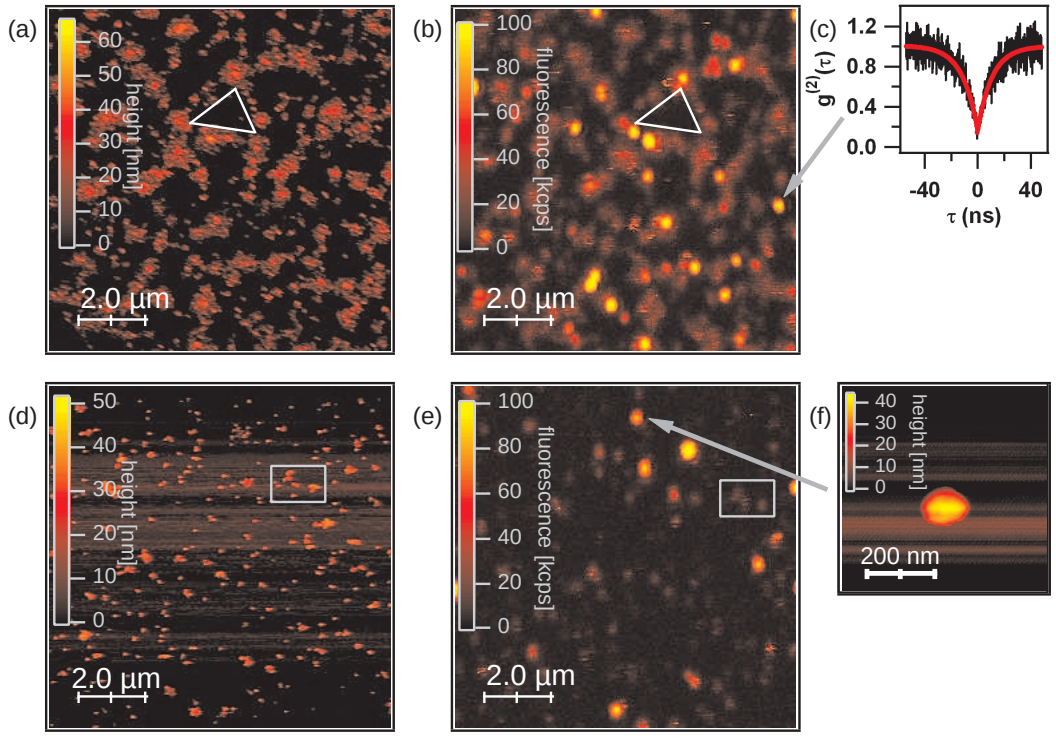

Figure 2.7: Simultaneous non-contact-AFM (NC-AFM) and confocal microscopy (CM) images. Line frequency 1 Hz. (a) NC-AFM of unprocessed nanodiamonds on a glass substrate. (b) CM image. The triangle is a guide to the eye for comparison of (a) and (b). Luminescence spots above 100 kcps indicate single centers. (c) Verification by measurement of the autocorrelation function. Radiative lifetime $\tau = 11.2 \pm 0.6$ nm. (d) NC-AFM image of nanodiamonds diluted by a factor of 3 after centrifuging. (e) Corresponding CM image. The rectangle is a guide to the eye. (f) NC-AFM image of a single fluorescent nanodiamond of 30 nm total height. All measurements have been conducted at Universität Stuttgart with assistance of G. Balasubramanian.

thus $g^{(2)}(0)$ has to be zero. In practice, if $g^{(2)}(0)$ drops below 0.5 with a time constant matching the range of fluorescent lifetimes expected, a single NV^- center is present. The remaining structured luminescent background in the confocal image comes most likely from a deagglomeration agent contained in the as-delivered nanodiamond suspension. For subsequent measurements this agent was removed by centrifugation (10 minutes at 10000 rpm) of the suspension and replacement of 2/3 of the liquid phase by deionized water. This procedure was repeated 5 times in total. Directly before spincoating the resulting suspension was rehomogenized in an ultrasonic bath for 10 minutes to prevent cluster formation of nanodiamonds. AFM measurements (see figure 2.7d and 2.7f) revealed no change of the size distribution, which indicates that even the smallest nanodiamonds have settled to the ground during centrifugation.

2.4.2 The confocal fluorescence microscopy detected pulsed magnetic resonance setup

One of the initial perspectives of this work was the observation of couplings of paramagnetic molecules to NV centers. Some attempts regarding this topic have been done prior to this work by K. Hübener and C. Oelmüller, but the desired coupling was not yet detected. Some of the initial investigations performed in this work were done using the existing setup (see Fig. 2.8) which has been described in the corresponding theses [93, 94]. However, it became evident that the limitations of continuous wave spectroscopy, e.g. a spectral resolution of $\sim$10 MHz are too severe in order to achieve this goal. Pulsed magnetic resonance allows for a better resolution, since it is not limited by optical and inhomogeneous broadening, but by the intrinsic coherence time T_2. Coherent manipulation of the NV^- spin was first demonstrated by F. Jelezko in 2004 [39], whose support and expertise in building up the setup is gratefully acknowledged. Due to technical reasons the complete setup had to be replaced by a new setup shown in Fig. 2.9, and is described in the following paragraph.

The basic concept underlying the optical part of the setup is a standard confocal fluorescence microscope first described and patented by Marvin Minsky in 1957 [95]. While we will briefly introduce the basic principles, for a more detailed study we have to refer to one of the great number of textbooks available on the topic [96–98]. A list of reviews is provided by Olympus Corp..

In a confocal setup the incident beam enters a wide aperture microscope objective. The fluorescence excited by the laser exits the objective and is separated from the excitation beam (e.g. by a beam splitter or dichroic mirror), then it is focussed into an small aperture pinhole or directly detected using a small area

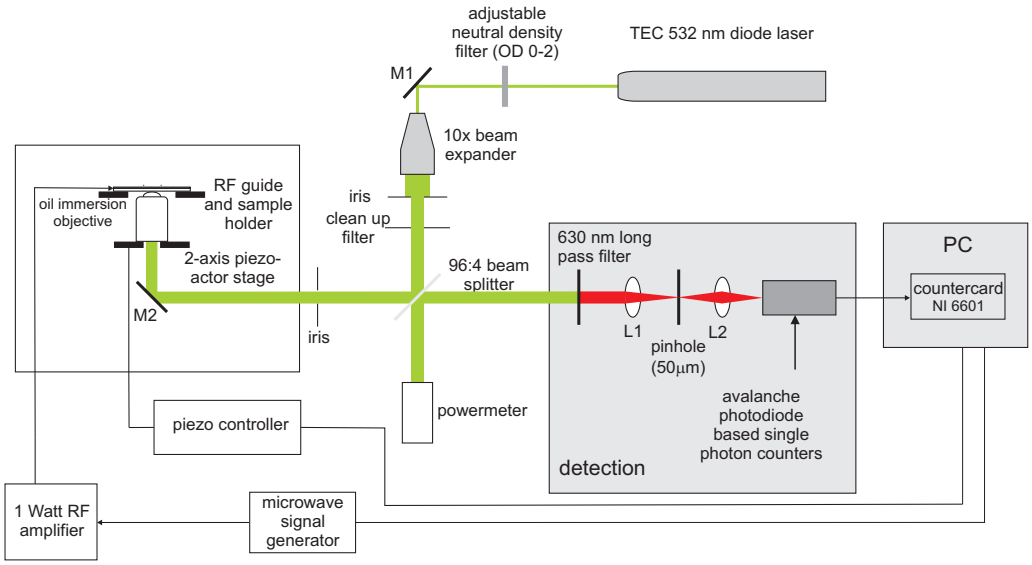

Figure 2.8: Experimental setup for confocal fluorescence microscopy detected continuous wave magnetic resonance spectroscopy built by K. Hübener and C. Oelmüller [93, 94]

detector. The reason for using a pinhole is that light emitted outside of the focal plane will be focussed in front or behind the pinhole and will be blocked by it (see Fig. 2.10). Only light from sources within the focal plane and backscattered light is able to pass the pinhole. The key advantage of this approach is that the microscope can focus and detect not only in two but three dimensions. Stray light is strongly suppressed and the optical resolution r_{conf} is given by the wavelength λ of the incident beam and the numerical aperture $\mathrm{NA} = n\sin(\theta)$ (n is the refractive index) of the objective.

$$r_{\mathrm{conf}} = 0.44\frac{\lambda}{NA} \qquad [99] \tag{2.14}$$

Equation 2.14 is valid only for an infinitely small pinhole. For larger pinholes, necessary to let pass a finite amount of light, the prefactor becomes slightly larger. The resolution perpendicular to the plane is also influenced by the size of the pinhole and typically larger by a small factor.

In order to observe undisturbed spin dynamics the laser must not continuously excite the system. On the other hand, pulsed sources tend to exhibit fluctuations in intensity of the individual pulses. In addition, a single NV$^-$ center is not able to emit more than one photon at once, which would result in inefficient excitation

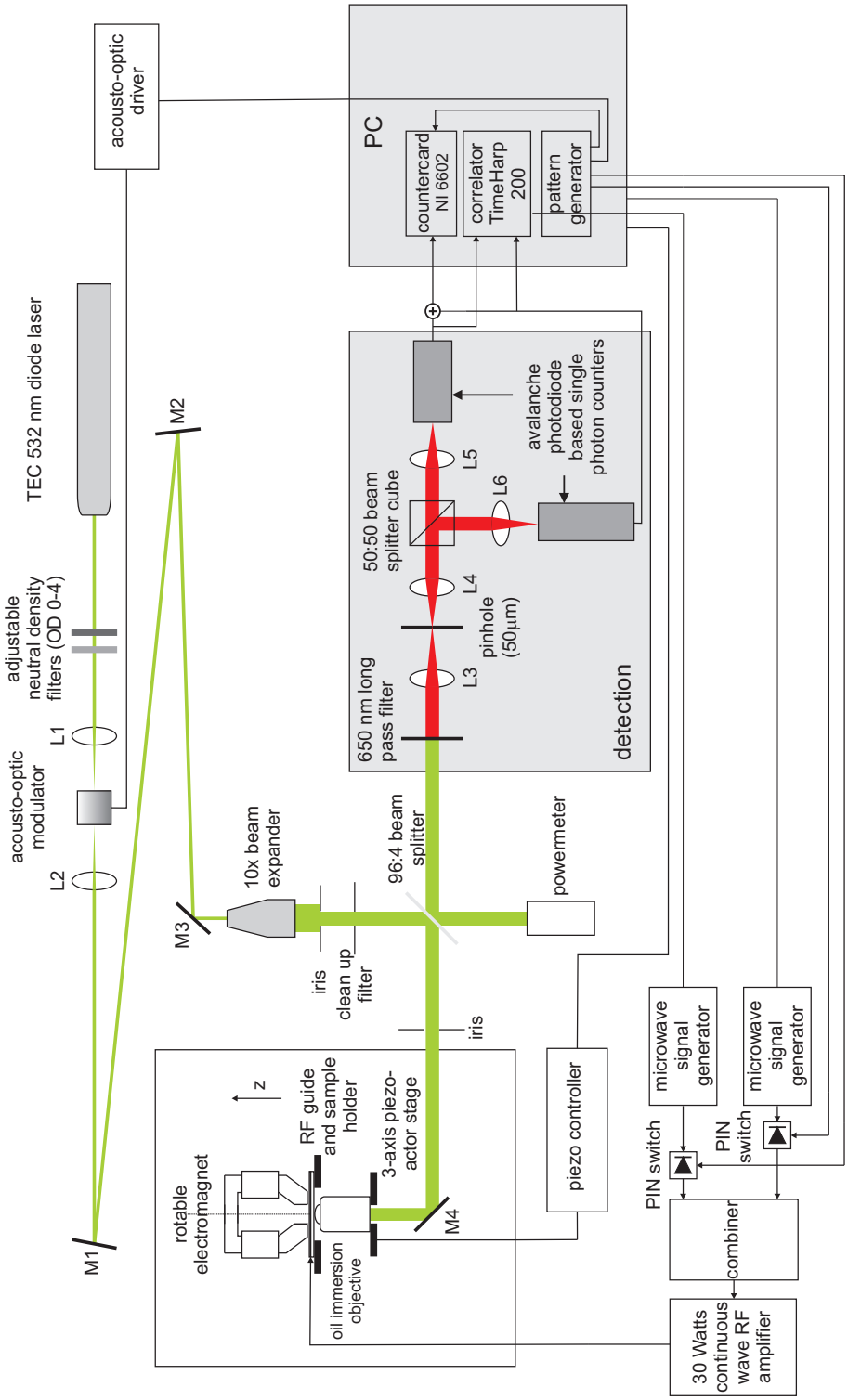

Figure 2.9: Experimental setup for confocal fluorescence microscopy detected pulsed magnetic resonance spectroscopy.

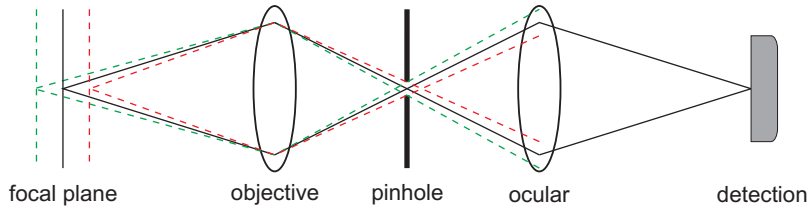

Figure 2.10: Simplified principle of a confocal microscope. Light sources outside of the focal plane are refocussed at different spots along the optical pathway. A pinhole located at the second focus spot will suppress most of the light from outside the focal plane.

by pulsed sources. Thus, a fast chopped continuous wave laser is the best choice for excitation.

In our setup we use a thermoelectrically cooled diode pumped solid state laser (GMP TECGL-30, 532 nm, 30 mW) whose power can be continuously attenuated by up to three orders of magnitude using a set of adjustable neutral density filters. An acousto-optical modulator (AOM3200-146, Crystal Technology, Inc.) is used to to deflect the beam onto the sample with $\propto$ 15 nanoseconds switching time allowing for laser pulses with variable length and duty cycle. The beam is deflected by 3 mirrors for maximum spot separation. The light deflected onto the sample during the "off" cycle due to power leakage of the AOM driver was about 0.2 %. Behind a 5x beam expander (Thorlabs) the homogeneous center area of the beam passes a clean up filter (width 10 nm) and is guided onto an oil immersion objective (Olympus PlanApo 60x N.A. 1.42, work distance 0.17 mm) mounted to a three-axis piezo stage (piezosysteme jena, PXY200,PZ100). The fluorescence light is separated from the excitation pathway using a 96:4 beam splitter (LINOS). This way the excitation beam is further attenuated while most of the fluorescence light enters the detection chamber. After a 650 nm high pass filter (Thorlabs), needed to block the scattered laser light and to suppress luminescence from the glass substrate and the NV^0, the beam is focussed onto a 50 micron pinhole. Behind the pinhole the beam is parallelized, split by a 50:50 beam splitter (Thorlabs) and focussed onto two single photon counting modules (SPCM-ACRH14, Perkin Elmer/Laser Components) based on avalanche photo diodes. The signals from the two detectors is split between a 80 MHz timebase counter card (National instruments NI6602) and a correlator card (Picoquant TimeHarp200) which allows for dead time free 40 ps time resolution measurements of the second order autocorrelation function.
The microwave is generated in separate channels by two sine generators (Anapico

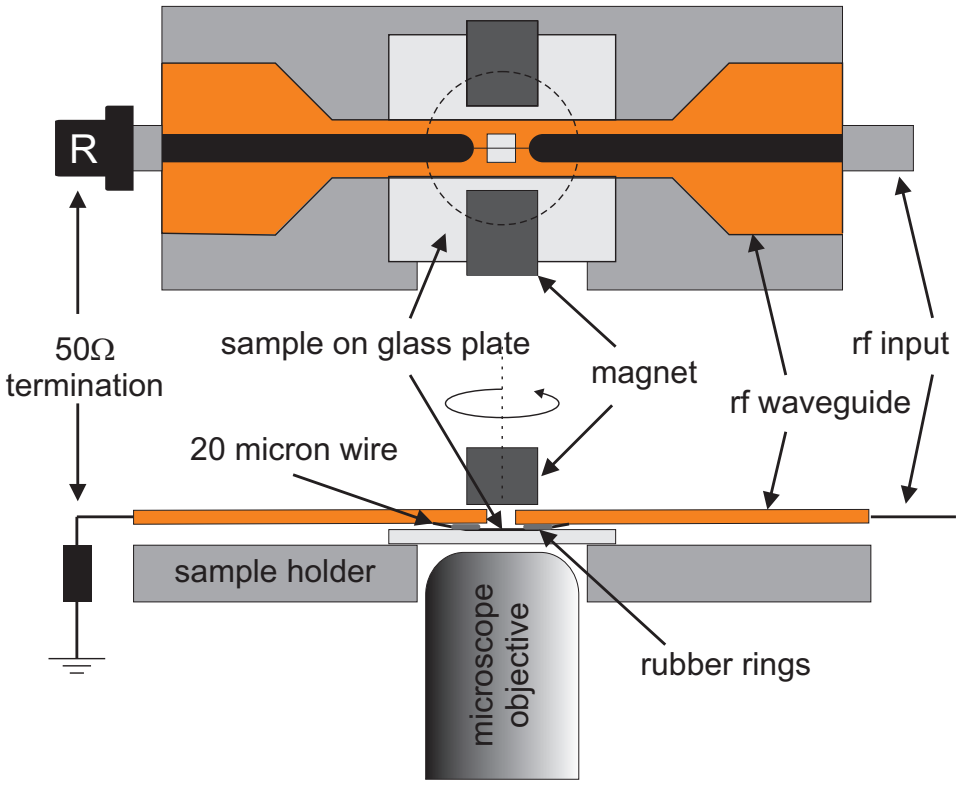

Figure 2.11: Sample holder for ODMR on nanodiamonds dispersed on glass including the microwave guide connected to a 20 μm thick copper wire acting as antenna. upper part: top view, lower part: side view

APSIN3000 and APSIN6000) and combined after two pin switches (Minicircuits ZASWA-2-50DR) at the input of a continuous wave amplifier (MILMEGA,30W/17W two band, bandwidth 0.8 GHz to 4.2 GHz). A strong magnetic field component of the microwave is generated at the sample using an uncoated 20 micron copper wire that acts as an antenna (see figure 2.11). Compared to a microwave resonator, a strip line antenna has the advantage of flat frequency response, which allows for frequency sweep experiments over many octaves. Close to the antenna the B_{ac} field strength can be calculated from the Biot-Savart law

$$B_{\mathrm{ac}} = \frac{\mu_0 I_{ac}}{2\pi d} \quad , \tag{2.15}$$

where d is the distance to the wire and I_{ac} is the current through the wire that can be calculated by the microwave power P_{rf} and the impedance Z of the wire

using

$$I_{ac} = \sqrt{\frac{P_{\mathrm{rf}}}{Z}} \quad . \tag{2.16}$$

Assuming zero losses and a perfect impedance matching, theoretically a maximum microwave field of about 5 mT would be achievable at point zero distance to the wire. Practically, about a factor of 10 lower field amplitudes were realized. The timing is controlled by a 400 MHz pattern generator (Spincore PulseBlasterESR-PRO) which triggers the counter card, AOM driver and pin switches. A home-built removable electromagnet [100] that can be rotated around the observation axis can create an external magnetic field at the location of the sample of up to 0.3 T.

2.4.3 Observation of CW ODMR on NV$^-$ centers

Continuous wave ODMR on single NV$^-$ centers is realized by selectively exciting a single point source and measuring its luminescence using the optical focus. In our setup we achieved a lateral resolution of about 280 nm. To find out whether the luminescence comes from a single NV$^-$ center, the second order autocorrelation function of the incoming photons was measured. In early experiments, where fast photon correlation was not not available, we used the symmetry and size of the luminescence spot, luminescence intensity and stability as well as the shape of the ODMR spectrum as a measure to determine wether a single NV$^-$ center is present or not. While the shape and intensity of luminescence is a rather weak criterion due to the low resolution of the confocal microscope compared to the size of the nanodiamonds and the broad range of fluorescence lifetimes found, the stability is a much better criterion. Under high power laser excitation most light sources tend to bleach or blink immediately. In this sense, the extraordinary photostability of the NV$^-$ center [83] is a very prominent feature. Using a 650 nm longpass filter allows to effectively suppress luminescence coming from the neutral NV^0 center. If spin resonance at about 2.88 GHz can be observed, it is apparent that at least one NV$^-$ center is present. In nanodiamond, the D tensor varies slightly between different centers ($D \approx 2.875 \pm 0.02\,\mathrm{GHz}, E \approx 0 \ldots 0.02\,\mathrm{GHz}$), so that every center shows a characteristic fingerprint. In addition, since the Zeeman splitting of the spin at low field depends on the angle between the field and the center axis, it is very unlikely that two centers have the same splitting at nonzero field. One should note that this is true only for centers in nanocrystaline materials, since in a single crystal only 4 orientations along the $\langle 111 \rangle$ axes are possible. Figure 2.12a shows the ODMR spectrum of a single NV$^-$ center at zero and nonzero magnetic field. In addition to reduced Zeeman splitting random field orientation results in an effective partial quenching of the signal due to mixing of the spin states [88].

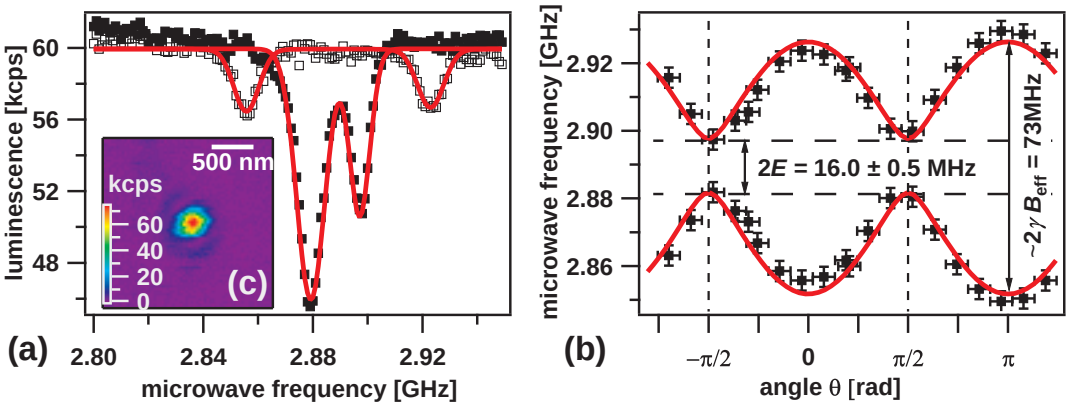

Figure 2.12: (a) cw ODMR spectrum measured at 1 Watt microwave power with (empty squares) and without (filled squares) application of a small static magnetic field ($\sim$ 50 G). (b) ODMR Peak positions measured by CW ODMR at 30dBm as a function of field orientation. E was determined from the peak positions at zero field (dashed lines). The effective field calculated from the maximum splitting was 1.3 mT. The solid red lines represent a simulation by numerical Hamiltonian diagonalization using the EASYSPIN 3.1.0 MATLAB package [101]. (c) CM image of the NV^- center.

Since the Zeeman splitting depends on the angle between the external field and the center axis, the orientation of the center can be determined by maximizing the Zeeman splitting. The maximum splitting only occurs at $B||D$. Aligning a strong field with the center axis is also an elegant method for magnetic field calibration because if the electron g factor and non-axial splitting E are known, the external magnetic field strength can be calculated from the field splitting. Figure 2.12b shows the dependence of the splitting on the angle θ between field and center axis. The solid curve corresponds to the result calculated by numerical Hamiltonian diagonalization using the Easyspin 3.1.0 MATLAB package [101]. The deviation between experiment and calculation is attributed to experimental errors, a mismatch of the rotation axis of the magnet with the observation spot being the most prominent systematic error. The mismatch leads to a slightly different field magnitude between 0 and π at the location of the center.

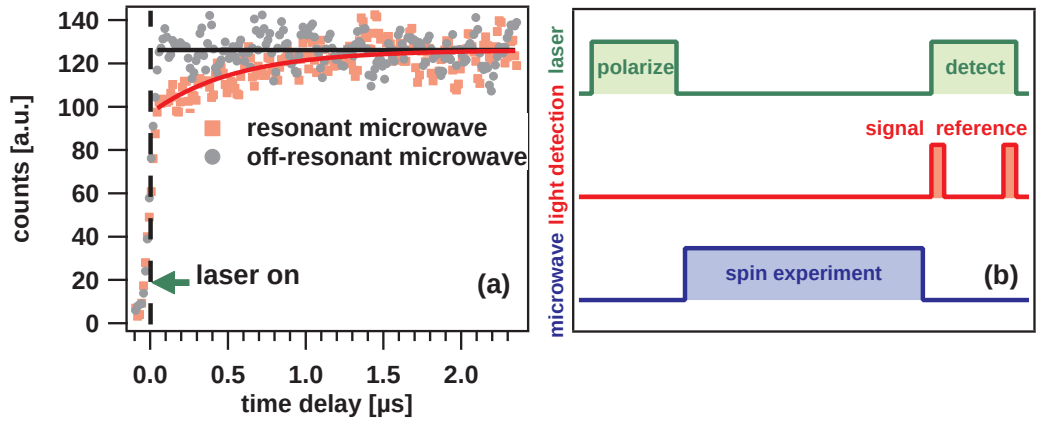

Figure 2.13: (a) Luminescence response of a NV center on the laser recorded by boxcar averaging of 75 ns width. The rise time of the laser is much smaller than the boxcar width. The repetition rate of the laser pulses was 100 kHz, their duration 3 μs . Off resonance, the center stays spin polarized and luminescence is constant while on-resonance the polarization is destroyed between the laser pulses within T_2^* and recovers exponentially with a 320 ns time constant. (b) Concept of pulsed spin readout. The population of the S_z state is given by signal/reference. Technically, the readout laser pulse acts as polarizer for the next experiment.

2.4.4 Observation of coherent dynamics of a single spin

In order to determine the spin projection S_z at a given time by the luminescence intensity, it is important to account for the fast re-polarization of the spin. As a result, after a very short time, typically less than a microsecond, the spin information is lost. Thus, a fast gated detection synchronized with the laser is necessary. Figure 2.13 shows the luminescence response to a square laser pulse in the cases that the center was either spin polarized by previous long time illumination or depolarized (saturated) by a resonant long high power microwave pulse of about 5 microseconds length. For this particular laser power ($\sim 50\mu$W) and center orientation, a time constant of 320 ns was derived for re-polarization of the spin system. Consequently, in most experiments a 300 to 500 ns long detection window at the beginning of the laser pulse was used. A second window of equal length was applied at the end of the laser pulse, where the center was completely re-polarized. The luminescence measurement from this window was used as reference to normalize the data. The coherent dynamics of a single spin is shown in figure 2.14. The decay behavior of the Rabi oscillations is slightly different in different centers. In some centers it is mono-exponential, while in others it is described better with a

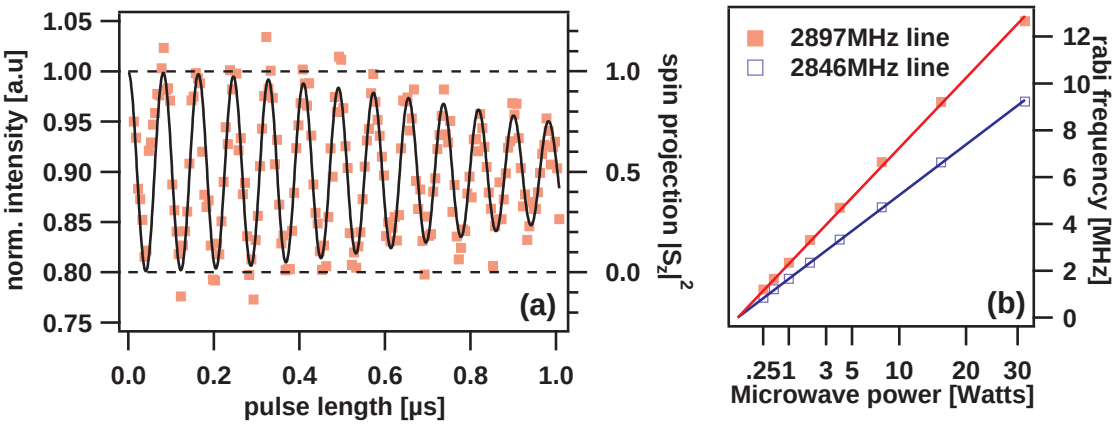

Figure 2.14: (a) Spin Oscillations of the $|0\rangle \rightarrow |+1\rangle$ transition exhibiting a Rabi frequency of 12.21(1) MHz at maximum microwave power (33 Watts). This corresponds to an effective B_1 field of about 4.4 G. The power dependence of the driving frequency of both transitions exhibits a square root law. The effective field acting on the $|0\rangle \rightarrow |-1\rangle$ line is smaller by 40 % (b).

squared-exponential law. The decay constant T_2^* is typically in the order of one microsecond, which is only slightly shorter than what was reported in high quality bulk diamond (1.4 μs [102] to 4.5 μs [41]). The sources of dephasing will be discussed in more detail in section 3.1.1.

In order to suppress dephasing, standard echo techniques can be applied, the simplest being the Hahn echo sequence. Here, differences in the Larmor frequency can be compensated by rotating the spin vector by π at given time τ. After a time 2τ spin vectors with different (but constant) precession frequency between different experimental shots will be in phase again. The spin echo cannot be measured directly, but the perpendicular magnetization has to be projected to the eigenstates of S_z by another $\pi/2$ pulse. In the standard Hahn echo sequence all microwave pulses have the same rotational axis (phase). The reconstructed echo for different times τ resulting from the Hahn echo sequence is displayed in figure 2.15. Note that the centers from figure 2.14 and 2.15 are different. The echo intensity is in general given by

$$I(\tau) = I_0 \exp\left(-\left(\frac{2\tau}{T_2}\right)^{\alpha}\right) \tag{2.17}$$

A decay constant T_2 can thus be derived, which is longer than T_2^*, and typically referred to as coherence time or phase memory time. Again, from the exponent

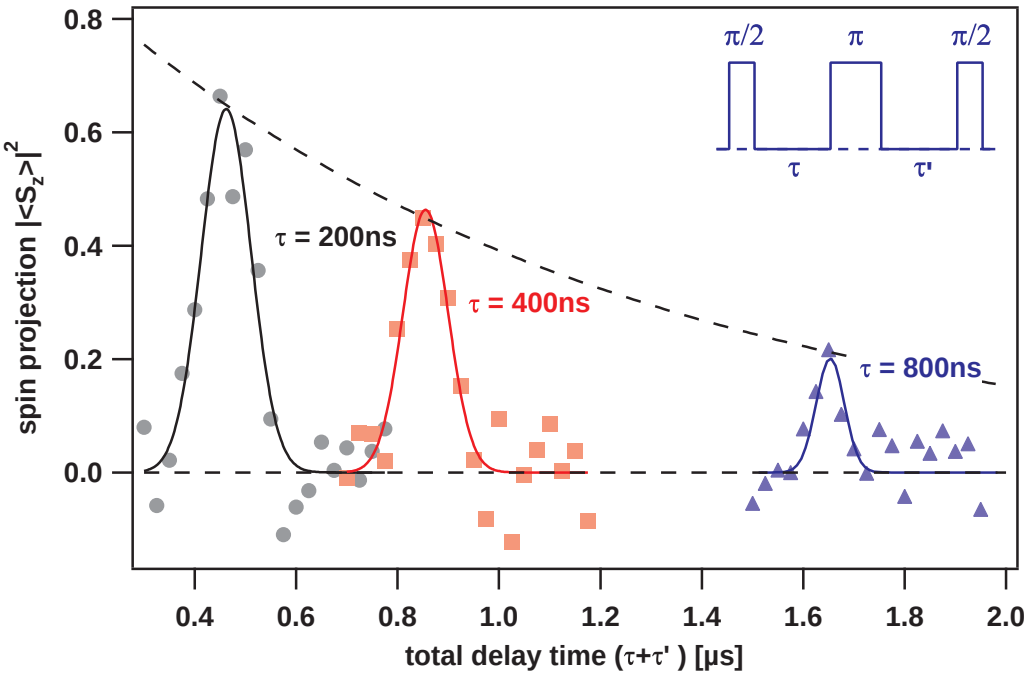

Figure 2.15: Spin Echo reconstruction at different values of τ. The inset shows the corresponding microwave pulse sequence. The length of the π-pulse was 110 ns. The envelope indicates an Echo decay time vs. $(\tau + \tau\prime)$ of 1.3 μs.

α the nature of the decoherence process can be derived, which will be extensively discussed in more detail in section 3.1.1.

2.5 NV^- centers coupled to proximal nuclear spins

The direct environment of the nitrogen vacancy center is very poor of nuclear spins due to the very high abundance (98.9 %) of carbon-12, which nucleus has $I = 0$. In addition, from DFT calculations [70] it is known that the spin density of the NV^- is very localized, basically within one lattice constant. Thus, if any hyperfine interaction is observed it arises from distinct proximal nuclear spins. This can be either carbon-13 ($I = 1/2$) or nitrogen-14 ($I = 1$). An observation of carbon-14 or nitrogen-15 is very unlikely due to the small natural abundance, although the latter has been observed in centers generated by ^{15}N ion implantation [103]. Since substitutional nitrogen defects also provide an electron spin of $S = 1/2$, which will exhibit a different and typically much stronger coupling to an NV^- center than a nuclear spin [104], hyperfine interaction to ^{14}N is only observed for the host nitrogen atom of the NV^- center. By coincidence, the coupling to the host nitrogen is weaker than the coupling to carbon-13 for many possible locations. This is why hyperfine interaction of the NV^- electron spin to proximal ^{13}C nuclear spins may often dominate the spectrum. As a result, spectra of different NV^- centers can look quite different from each other.

2.5.1 Theory of NV^- centers coupled to distinct spins

The full Hamiltonian of NV^- centers coupled to other spins reads

$$\mathbf{H} = \mathbf{H}_{\text{int}} + \mathbf{H}_{\text{ext}} \tag{2.18}$$

with H_{int} being the Hamilton operator of an isolated center (see equation 2.7) and

$$\begin{aligned}\mathbf{H}_{\text{ext}} =& \sum_n \gamma_N \vec{B}\mathbf{g}_n\vec{I}_n + \sum_m \gamma_m \vec{B}\mathbf{g}_m\vec{S}_m \\ &+ \sum_n \vec{S}\mathbf{A}_n\vec{I}_n + \sum_m \vec{S}\mathbf{T}_m\vec{S}_m \\ &+ \sum_{n>n'} \vec{I}_{n'}\mathbf{Q}_{n'n}\vec{I}_n + \sum_{m>m'} \vec{S}_{m'}\mathbf{R}_{m'm}\vec{S}_m\end{aligned} \tag{2.19}$$

including all terms due to other spins. The first two terms define the electron and nuclear Zeeman interaction of the surrounding spins respectively, the next two terms define their interactions to the NV^- spin (namely the hyperfine and electron spin-spin interactions) and the last two terms define the intrabath interactions of nuclei and electrons respectively. All surrounding electron spins are considered spin $\frac{1}{2}$, so no additional zero-field interactions come into play. Considering the fact that the zero-field splitting of the NV^- electron spin is much larger than any other term it defines the main quantization axis and thus direct spin flips

are forbidden. In the following we will also assume that the internal hamiltonian includes only an axial symmetric zero-field splitting tensor ($D \neq 0, E = 0$).
Since in the case of nanodiamonds the NV$^-$ axis usually points at a random direction, which is initially unknown, the angle between the spin vector and any small external magnetic field typically differs from zero. When considering only couplings to single nuclear spins the electron spin terms (2 and 4) and the intrabath terms (5 and 6) can be neglected. In this case, the Hamiltonian can be written in terms of secular ($||$) terms which commute with S_z^2, and non-secular ($\perp$) terms:

$$\begin{aligned} \mathbf{H}_{(||)} &= \mathbf{H}_{\mathrm{el}(||)} + \mathbf{H}_{\mathrm{nuc}(||)} + \mathbf{H}_{\mathrm{dip}(||)} \qquad \text{and} \\ \mathbf{H}_{(\perp)} &= \mathbf{H}_{\mathrm{el}(\perp)} + \mathbf{H}_{\mathrm{nuc}(\perp)} + \mathbf{H}_{\mathrm{dip}(\perp)} \end{aligned} \tag{2.20}$$

with

$$\begin{aligned} \mathbf{H}_{\mathrm{el}(||)} &= DS_z^2 - \gamma B_z S_z \\ \mathbf{H}_{\mathrm{nuc}(||)} &= -\gamma_N B_z I_z \\ \mathbf{H}_{\mathrm{dip}(||)} &= S_z \sum_\nu A_{z\nu} I_\nu \\ \mathbf{H}_{\mathrm{el}(\perp)} &= -\gamma \left(B_x S_x + B_y S_y\right) \\ \mathbf{H}_{\mathrm{nuc}(\perp)} &= -\gamma_N \left(B_x I_x + B_y I_y\right) \\ \mathbf{H}_{\mathrm{dip}(\perp)} &= \sum_\nu \left(S_x A_{x\nu} + S_y A_{y\nu}\right) I_\nu \end{aligned} \tag{2.21}$$

Typically, the non-secular terms including S_x and S_y are neglected, which corresponds to the so-called secular approximation commonly used in high field epr [89, 105]. In our case, the large zero-field splitting does not allow for this procedure. Instead, for small fields the non-secular terms can be considered as a small perturbation to the secular Hamiltonian. By application of second-order perturbation theory the influence of perpendicular magnetic fields can be derived by calculating the Hamiltonian for all electron m_S subspaces ([102]). Without going into detail (see [102], Supporting Material), as a nontrivial result from the calculation it is observed that transverse field components lead to dependencies of the effective field felt by the nucleus on $|S_z|$ of the NV$^-$ center spin, which is in some sources referred to as pseudo-nuclear Zeeman effect [89, 102, 106]. The splitting by the nuclear and pseudo-nuclear Zeeman interaction can be expressed by the form

$$\Delta E = \left(\gamma_e \frac{A_\perp}{D}\right) B_\perp \qquad [106] \tag{2.22}$$

where $A_\perp$ is the perpendicular component of the hyperfine tensor, and $B_\perp$ is the perpendicular field. As result, an effective g factor of nearby ^{13}C nuclei about up

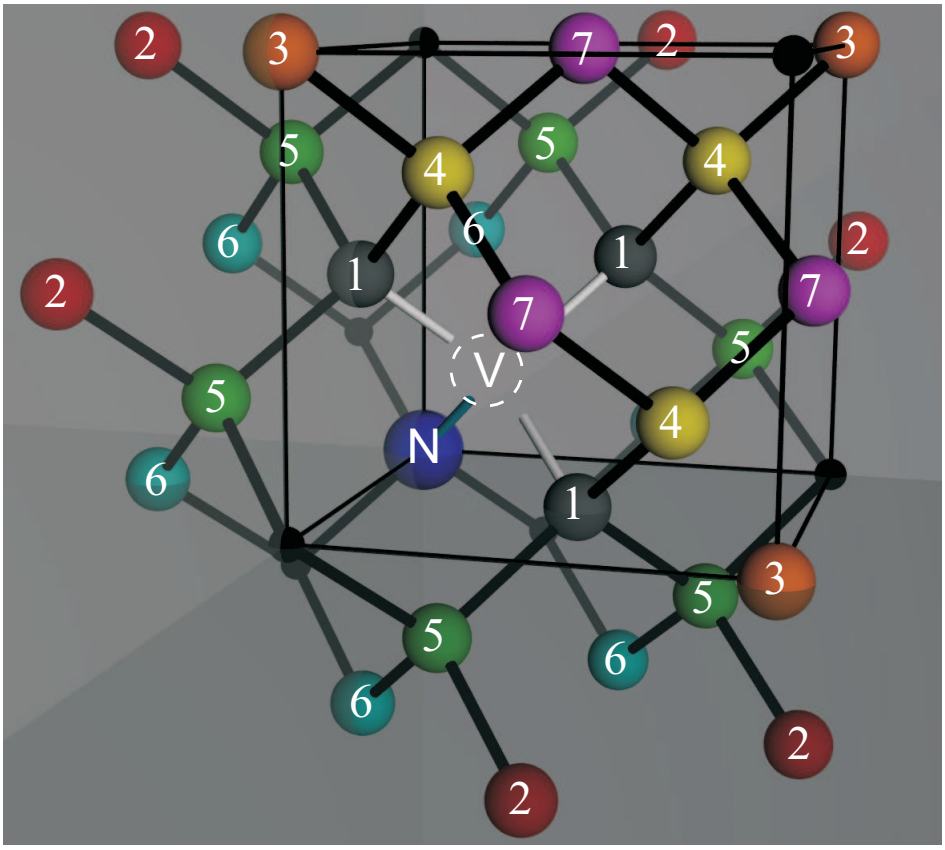

Figure 2.16: Possible sites of ^{13}C near the NV^- center. The numbers are ordered according to absolute interaction strength (disregarding sign), not by proximity.

to twenty times higher compared to the natural g factor was observed at perpendicular field [102]. Also, intrabath interactions are strongly enhanced at zero field [105].

2.5.2 Observation of couplings to distinct nuclear spins

The interaction to the three carbon 13 atoms closest to the vacancy is well know (130 MHz [107]) and has been studied extensively [44, 106, 108]. Very recently [62], precise assignments of coupling strength to nuclei at other locations have been made, which match theoretical predictions for some locations made earlier [109]. Figure 2.16 shows the the NV center and its possible neighboring carbon sites. From the natural abundance of carbon-13 (1.1 %) it can be deduced that about 3.3 % (6.4%, 18.1% , 30 %) of the centers are coupled to one of the first (second, third, fourth) shell of equivalent centers.

Table 2.3: Proximal ^{13}C sites, distance and hyperfine interaction strength according to ref. [62]

site #	A_{exp} [MHz]	distance [nm]	total # of sites
1	130	n.a.	3
2	13.72(3)	0.39	6
3	12.75(1)	0.39	3
4	-8.6(3)	0.25	3
5	-6.46(3)	0.25	6
6,7	4.15(3)	0.29	6,3

We have observed a wide variety of different couplings to carbon-13. Since the angle between the NV axis and the target nucleus cannot be manipulated it is difficult to distinguished the isotropic part of the interaction (contact term) from the anisotropic part (dipolar term), although they can in principle be identified by careful orientation-dependent measurement of the pseudo-nuclear Zeeman interaction (see eqn. 2.22). In figure 2.17 we show as an example the spectra of two centers coupled to one and two nuclei located in the second shell, respectively (red atoms in figure 2.16). Interactions up to the fourth shell are also observable with the resolution provided by standard optically broadened CW ODMR.

In order to observe smaller couplings, the resolution has to be enhanced. In particular, resolving the splitting due to the nitrogen nucleus (2.2 MHz) is required for proper identification of line broadenings or even smaller splittings. For this it is necessary to reach the limit given by homogeneous broadening ($1/T_2^*$). There are basically two ways to avoid power broadening. The conceptually simpler solution is to decrease laser and microwave power considerably. It can be seen though, that in order to achieve a resolution of 1 MHz, which is required to observe the hyperfine interaction to the nitrogen nucleus, the optical excitation rate has to be two orders of magnitude lower than what the radiative live time (80 MHz) would usually allow without saturating the center. Aside from limited photon statistics, the spin polarization of the center is then reduced due to the smaller ratio of pumping rate (repolarization) to spin relaxation rate (causing depolarization, see section 2.2). Hence, the signal becomes very small. Still, this resolution can be achieved within reasonable measurement time (see. fig. 2.18a). Using this approach we have been able to resolve line splittings of the nitrogen-14 hyperfine lines as small as 1.15 MHz (fig. 2.18b), but the total acquisition time was much larger than expected from photon shot-noise.

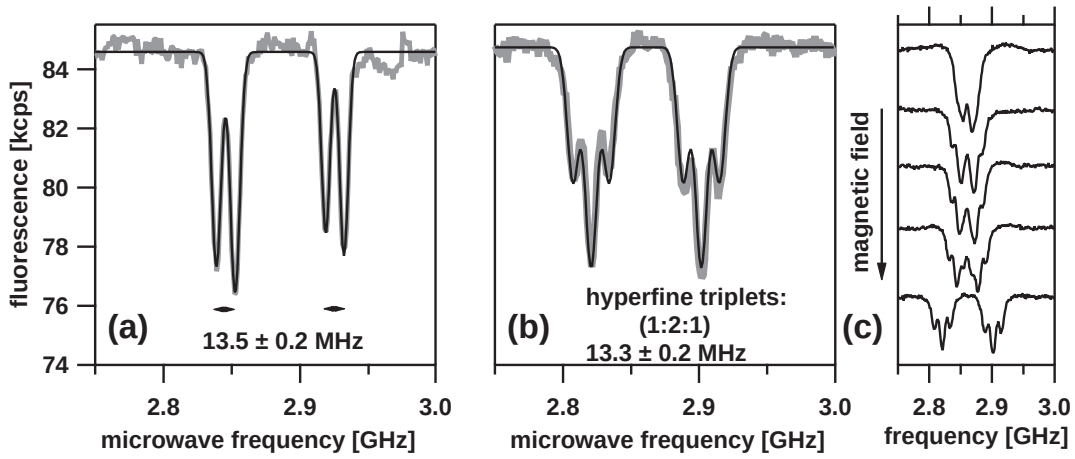

Figure 2.17: Continuous wave measurement of a NV center coupled to (a) one and (b) two ^{13}C nuclear spins. The size of the isotropic hyperfine splitting indicates that the nucleus is located in the second carbon shell around the NV center. laser power: 50 μW, microwave power: 30 dBm.

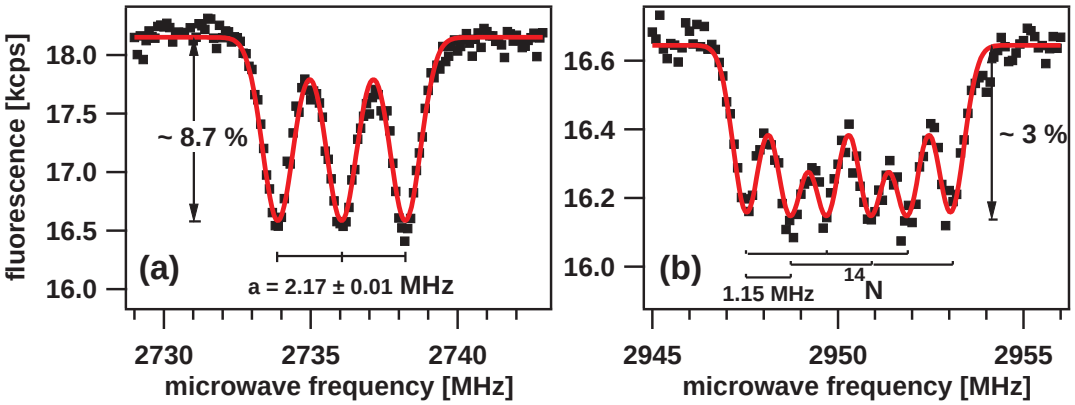

Figure 2.18: (a) High resolution continuous wave measurement of the $|0\rangle \rightarrow |-1\rangle$ transition peak revealing a triplet resulting from the hyperfine coupling to the host ^{14}N nucleus (FWHM 0.85 MHz). laser power: 2 μW., microwave power: 15 dBm. acquisition time: 400 minutes. (b) same measurement on a different center revealing a ^{14}N triplet that is additionally split by 1.15 MHz into doublets by an unknown source. laser power: 3 μW., microwave power: 10 dBm. total acquisition time: 10 minutes per point.

Faster acquisition of spectra at the resolution limit given by homogeneous broadening can be realized by separating optical and microwave excitation in time. Most importantly, this will avoid optical broadening of the epr lines due to laser excitation. In addition, better spin polarization can be achieved by the laser, and the ODMR contrast can be maximized by setting the microwave excitation length to effectively invert the spin population (π pulse), which will ideally increase the contrast by a factor of two when compared to continuously equilibrating the spin levels. Of course, these advantages are accompanied by a slight loss in photon statistics due to less-than-unity duty cycle of detection, which is on the other hand compensated by a reduction of noise due to the higher sampling rate, if reference measurements as explained in section 2.4.4 are taken. This technique is also limited by T_2^* which constrains the maximum length of the microwave pulse. The resulting spectrum (see fig. 2.19) is identical to a CW spectrum, but can be acquired 10 times faster with the same signal-to-noise ratio.

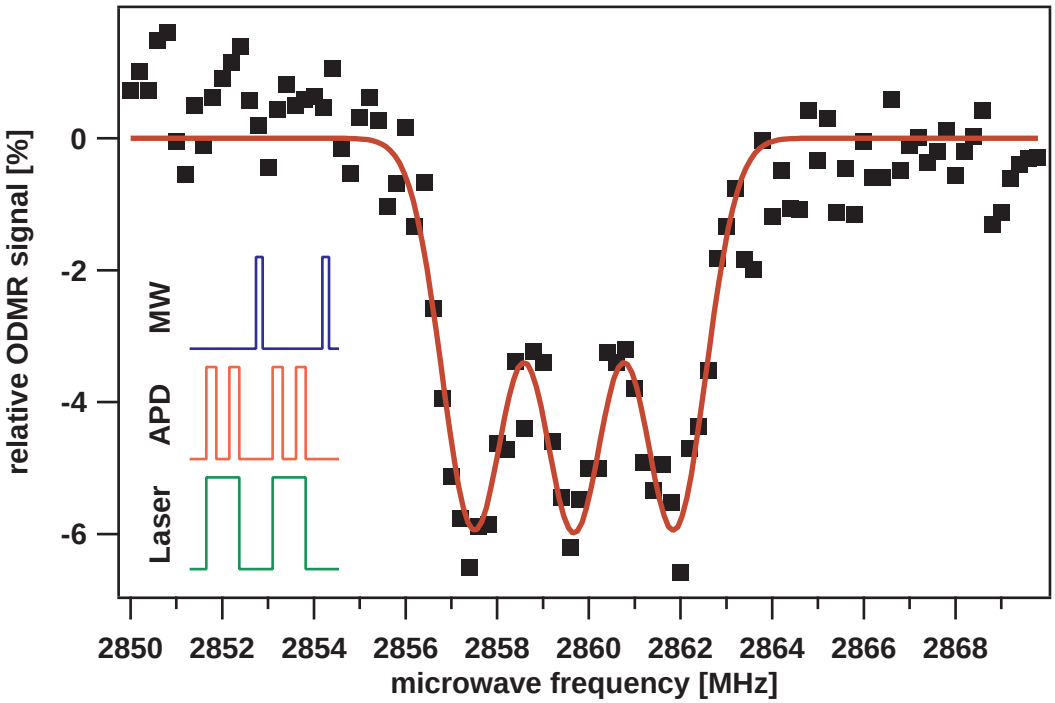

Figure 2.19: Spectrum of an NV$^-$ center (different from the one shown in fig. 2.18, but with comparable signal strength) measured by a sweeping π pulse experiment, also revealing the ^{14}N hyperfine triplet ($A = 2.18 \pm 0.01$ MHz). laser power: 50 μW, microwave power: 15 dBm. π pulse length: 680 ns. acquisition time: 20 minutes.

2.6 Coherent dynamics of nuclear spins coupled to the NV^- center

In order to identify the spin that is coupled to the NV^- center without doubt, one can measure the nuclear Zeeman interaction to determine the magnetic moment and gyromagnetic ratio of the spin. From equation 2.22 it arises that for field alignment parallel to the center axis the pseudo-nuclear Zeeman effect vanishes and the effective gyromagnetic ratio approaches its natural value for pure Zeeman interaction only ($\gamma(^{13}\mathrm{C}) = 10.71\,\mathrm{MHz/T}$). Unfortunately, the nuclear Zeeman interaction cannot be measured by CW spectroscopy of electron spin transitions only. In addition, the gyromagnetic ratio of most nuclei is very small compared to the epr line width. Fortunately, spin echo techniques provide an efficient solution to the problem. Given a sufficiently long coherence time T_2, the echo amplitude is modulated by coherence transfer of the refocussing pulse into forbidden transitions. This effect is commonly known as ESEEM (electron spin echo envelope modulation) [89]. It has to be noted that for single spins and in particular in case of the NV^- center this observation has been been termed "collapse and revival" by the community [102]. The major reason of the difference in terms is related to the fact that in the case of single spins one can consider the resulting dynamics as periodic entanglement and disentanglement of an electron and a nuclear spin. Despite this, in the following the more general word ESEEM will be used.

According to Childress *et al.* [102] the electron spin echo modulations of the $|\,m_S\rangle \rightarrow |\,m'_S\rangle$ transition can be described by the function

$$S(\tau) = 1 - \frac{\left|\vec{B}_{m_S} \times \vec{B}_{m'_S}\right|^2}{\left|\vec{B}_{m_S}\right|^2 \left|\vec{B}_{m'_S}\right|^2} \times \sin^2\left(\frac{\omega_{m_S}\tau}{2}\right) \sin^2\left(\frac{\omega_{m'_S}\tau}{2}\right) \quad . \tag{2.23}$$

Here, $\vec{B}_{m_S}$ and $\vec{B}_{m'_S}$ are the effective field vectors felt by the nucleus, which are given by the sum of the external field, the additional field mediated by the electron spin, and the dipolar field of the electron spin. The first two terms can be combined by defining a m_S-dependent effective gyromagnetic ratio $g_{\mathrm{eff}}(m_S)$:

$$\vec{B}_{m_S} = \frac{g_{\mathrm{eff}}(m_S)}{g_N}\vec{B}_{\mathrm{ext}} + \vec{B}_{\mathrm{dipol}} \tag{2.24}$$

Furthermore, ω_{m_S} and $\omega_{m'_S}$ are the precession frequencies of the nucleus, which are given by

$$\begin{aligned} \omega_0 &= \gamma_N |\vec{B}_0| \\ \omega_{\pm 1} &= \gamma_N |\vec{B}_1| \pm ||\mathbf{A}|| \approx \sqrt{\mathrm{Tr}(\mathbf{A}^2)/3} \quad . \end{aligned} \tag{2.25}$$

From these equations it can be seen that it is possible to observe not only the overall hyperfine interaction strength, which for large hyperfine coupling is roughly given by $\omega_{\pm 1}$, but the effective gyromagnetic ratio from ω_0 as well. It has to be noted, though, that the depth of the modulation is given by the orientations of the effective fields and can become zero for certain angles. This is in particular the case for external fields aligned to the center axis and only vanishing contribution of the dipolar interaction.

An example of ESEEM of the spin echo of an NV^- center coupled to a ^{13}C nucleus is displayed in figure 2.20a. The faster modulation at $\omega_1 = 2\pi \times 4.9(2)$ MHz is not visible due to the time sampling rate of 1 MS/s. The dependence of ω_0 on field angle and strength is shown in figure 2.20b. At aligned field (0°) the modulation amplitude was very small, indicating a minor dipolar component to the overall hyperfine interaction. Within error margins given by the orientational error, the gyromagnetic ratio was identical to $\gamma(^{13}C)$. A perpendicular hyperfine component of 4.4(2) MHz was taken from the pseudo-nuclear component of the effective gyromagnetic ratio (see fig. 2.20, inset). Assuming an axial hyperfine tensor we conclude that $A_{\parallel} = 5.9(3)$ MHz. The limit for observing frequencies was given by T_2, which varied strongly at different field strength and orientation (for detailed explanation, please refer to section 3.1.1).

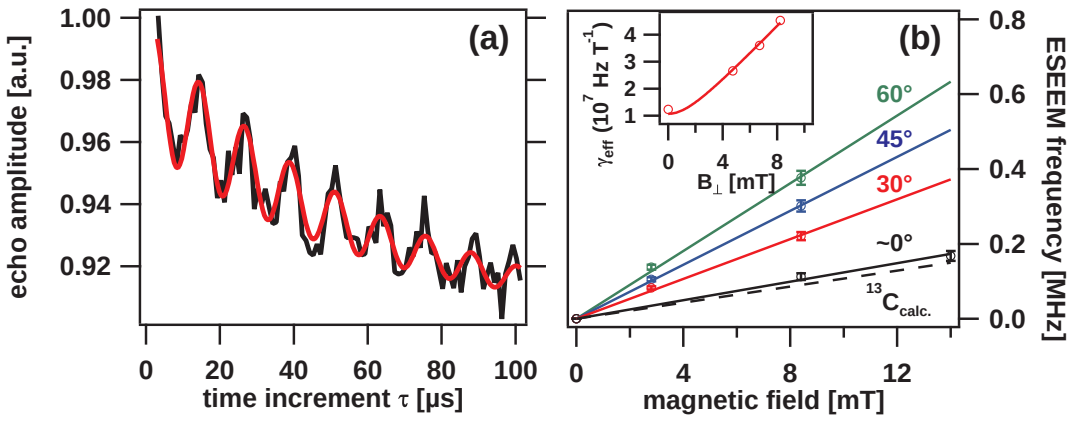

Figure 2.20: (a) Electron spin echo envelope modulation at 2.4 mT, 30°. (b) Frequency dependence on magnetic field strength and orientation. If the field is aligned along the NV center axis, the effective gyromagnetic ratio approaches the value known for carbon-13 (10.7084×10^7 Hz/T, dashed line). The inset shows the dependence of the effective gyromagnetic ratio on the strength of the perpendicular field. From the fit, according to eqn. 2.22 $A_{\perp} = 4.4(2)$ MHz can be derived.

2.7 Summary and discussion

In summary, with the setup described in this chapter we are able to coherently manipulate and measure the spin projection of the electronic ground state of NV^- defects in dispersed nanodiamonds onto its main quantization axis given by zero-field splitting. From autocorrelation measurements it was verified that we access a single defect center. Our optical resolution of 280 nm FWHM corresponds to the optical diffraction limit and the maximum spin nutation frequency achieved was about 10 MHz. An optical contrast of up to 30 % was observed. This can be understood with the help of a 5-level model. While using the model we are able to predict the contrast within error margins of a few percent, overidealizing assumptions, like neglecting spin-lattice relaxation, forbidden processes, and optical excitation of forbidden transitions lead to systematic deviations at very low or high excitation power. Still, the model has proven helpful in choice of an appropriate power "set-point" of the ODMR experiment. Extending the model by including additional processes (e.g. spin-lattice relaxation, optical excitation of forbidden transitions and thermal repopulation of the excited triplet state via the singlet level) might lead to a better understanding of the effect, but for exact predictions such a model will require detailed knowledge of even more physical properties, which will vary strongly in the case of a strained environment like a nanodiamonds. Thus, any more detailed model will probably have an advantage only in the case of defect centers buried deeply in unstrained crystals like single-crystaline diamond.
Using optically detected standard epr techniques like cw spectroscopy and Hahn echo we were able to observe and identify couplings to nearby nuclei, in particular nitrogen-14 and carbon-13. The spectral resolution was ~ 10 MHz for high power cw spectroscopy, ~ 1 MHz for $1/T_2^*$ limited spectroscopy, and ~ 100 kHz for echo techniques limited by a rather short T_2 in nanodiamonds compared to bulk. Coherent dynamics of single nuclei were observed as echo modulations (collapse and revival of the echo) and could be described invoking spin anisotropy induced by perpendicular magnetic fields and dipolar hyperfine coupling. By detailed analysis of the modulation frequency dependence on field strength and orientation the type of nucleus and the main axis hyperfine tensor components were determined.

Chapter 3

Decoherence processes and dynamic decoupling

3.1 Decoherence and relaxation of the NV^- spin

3.1.1 Introduction

One of the most important tasks and challenges in quantum information is the preservation of coherence of the quantum systems used. If coherence is lost the quantum system becomes indistinguishable from a classical system and the advantages of quantum information can no longer be exploited. In order to overcome decoherence, quantum error correction [36] (QEC) can be applied, which is able to completely compensate for information losses. Still, general and complete QEC requires a large minimum of gates ($\geq 10^4$) during which coherence must be preserved. In many materials currently explored in the context of quantum information (e.g. III-V semiconductors) the problem of decoherence is the most limiting factor in applicability.
The sources of decoherence are numerous and depend on the quantum system used. In the case of spins in general and electron spins in the particular case that will be discussed here, anything that unintentionally couples to the spin states ranging from phonons to other spins in the environment, as well as randomly fluctuating magnetic fields will lead to decoherence.
One usually distinguishes energy conserving dephasing of the spin due to a uncertain or randomly fluctuating precession frequency, from longitudinal relaxation that projects the spin into one of its eigenstates and hence changes the energy. Irrespective of the mechanism, any irreversible dephasing can be in general described by the spin-spin relaxation time T_2, while longitudinal relaxation is described by the spin-lattice relaxation time T_1. Since the latter process annihilates the phase of the spin, spin-lattice relaxation ultimately limits coherence and in general for a

single spin the equation

$$\frac{1}{T_1} \leq \frac{1}{T_2} \tag{3.1}$$

applies.
In terms of spin coherence, diamond is an excellent material for multiple reasons. First, due to the extraordinary hardness of the material resulting in a large Debye temperature (2200 K [110]), even at room temperature ideally no optical phonons are present, which normally contribute strongly to spin-lattice relaxation. Furthermore, due to the large band gap very few conduction electrons are present that can induce spin flip-flop processes. This is especially true in the case of single crystalline undoped electronic grade diamond, where T_1 is extraordinarily long (more than 1 s at room temperature [41]). Moreover, the ground state of the NV^- center possesses a large zero-field splitting that dominates the spin precession frequency and thus detunes the spin transitions from other electron spins, making this process inefficient in absence of other like spins. As a result, even in nanodiamonds longitudinal relaxation can in first order be neglected as a source of decoherence. Another important property is that natural diamond consists of about 99 % of carbon-12, a nucleus without spin and thus without a magnetic moment. This represents a great advantage to III-V semiconductor materials where T_2 is typically in the order of nanoseconds [111] due to the fact that typical elements in the III and V groups have magnetic nuclei. This value is outperformed even by the nanodiamond samples discussed above, where already the inhomogeneously broadened lines can exhibit a width of less then a Megahertz, which implies that $T_2 > 1\,\mu$s. In the case of isotopically enriched diamond with very low defect concentration, a T_2 of 2 ms at room temperature was recently observed [41], which is the highest coherence of any electron spin system at room temperature known.

Since isotope enrichment is expensive and nuclear spins are the known source of decoherence in electronically pure diamond, finding a way to decouple NV^- centers from the surrounding nuclear spin bath is of great technical importance. Furthermore, for some applications, in particular when using nano-crystals or near-surface centers, a dirty electronic environment might not be avoidable. In consequence, decoupling from other sources than nuclear spins can be necessary. Of course, in order to find effective ways to do so, a better understanding of the processes underlying T_2 is crucial.

3.1.2 Relaxation theory of the NV^- spin

The relaxation of NV^- centers in electronically pure bulk diamond has been studied in great detail over the past few years. Sufficient theoretical modeling has been

achieved by the disjoint cluster approach [105]. The fundament of the approach is based on the Hamiltonian provided in section 2.5.1. The only source of decoherence considered are ^{13}C nuclear spins with natural abundance. When numerically summing over a large number of nuclear spins, it is assumed that groups of nuclei form strongly coupled clusters which are only weakly interacting with their environment. This approximation greatly reduces the computational effort. Numerical predictions of this model provide an excellent match with the modulation and decay behavior of the spin echo [102]. An analytic description of the modulations, which describes the coherent dynamics has already been presented in section 2.6. Here we focus on the decay which is caused by decoherence.

According to standard relaxation theory [112], the echo intensity $S(\tau)$ can always be described by

$$S(\tau) \propto \exp\left(-\left(\frac{2\tau}{T_2}\right)^{\alpha(\tau)}\right) \quad , \tag{3.2}$$

where the exponent $\alpha(\tau)$ is determined by the correlation function

$$\langle m(0)m(\tau)\rangle_\tau \tag{3.3}$$

of the decoherence process $m(\tau)$ (e.g. by the spin bath dynamics). In simple cases, e.g. when the correlation function is $\sim \exp(-\tau/\tau_C)$, the exponent α becomes constant. One such case is given by a weakly interacting nuclear spin bath, where $\alpha = 4$ is expected [105]. Stronger interacting nuclear spins will eventually lead to relaxation being dominated by nuclear spin flip-flop processes. This is described by the standard theory of spectral diffusion [113]. For small times τ comparative to the correlation time τ_C, which is given by the nuclear dipolar spin-spin interaction, decoherence follows a squared exponential law ($\alpha = 2$). For long times τ compared to τ_C spectral diffusion theory predicts that $\alpha(\tau)$ approaches 0.5.

3.1.3 Decoherence in nanodiamonds

We have measured the decay of the spin echo of NV^- centers in nanodiamonds by using the Hahn echo sequence as introduced in section 2.4.4. First, T_1 was measured in order to distinguish spin flips from dephasing. Experimentally, the spin population was inverted by a selective π pulse (length: $\sim$ 100 ns) after optically polarizing the spin for 3 microseconds. Subsequently, after a time τ the spin polarization was measured using the pattern described in section 2.4.4. A

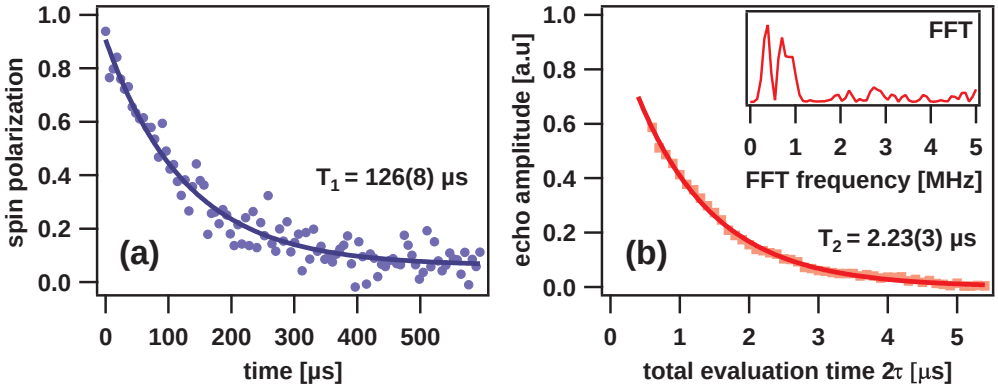

Figure 3.1: (a) Decay of the spin polarization by spin-lattice relaxation. (b) Decay of the coherence measured by Hahn echo. Aside from a mono-exponential decay a slight modulation can be observed (see fast Fourier transform, inset)

typical decay curve is shown in figure 3.1a. In all centers, a mono-exponential decay exhibiting a decay constant between 80 and 200 μs was observed.

The corresponding Hahn echo decay curve recorded at zero field is shown in figure 3.1b. For T_2 values between 1.2 and 8.4 microseconds have been found, which indicates that effects from longitudinal relaxation can be neglected. Surprisingly, all Hahn echo decay curves showed a mono-exponential decay behavior as well. On some decay curves, we found ESEEM, which could in some cases be attributed to ^{13}C (see section 2.6). When applying an aligned external magnetic field, the phase relaxation time increased up to a factor of twenty (see figure 3.2a), but aside from a higher modulation frequency, the decay behavior still stayed mono-exponential.

Discussion

While T_1 is shorter than expected for diamond, we have to consider carefully the effect of residual laser light which unintentionally re-polarizes the spin. In our setup, we observed that during the "off-phase" the AOM crystal still deflects light onto our sample. Optimizing the optical pathway, we achieved an on:off power contrast of 500:1. Extrapolating from a polarization rate of 350 ns at full illumination as was measured earlier (see section 2.4.4), one can expect that optical repumping during the "off-phase" occurs with a time constant of 175 microseconds, which is in the same time order as the values measured for T_1. Thus, our setup is not suited to measure longer time constants. For an undisturbed measurement of longer values of T_1 and T_2 it is necessary to add multiple AOM stages and fiber

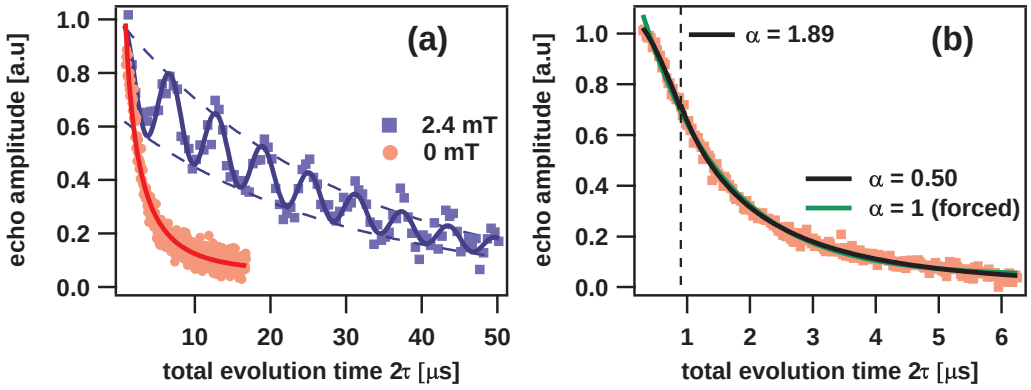

Figure 3.2: (a) Hahn echo decay at zero field (lower trace) and at 2.4 mT external magnetic field (upper trace). The decay constants are $2.4 \pm 0.2\,\mu$s and $30 \pm 5\,\mu$s. Strong echo modulations ($k \approx 50\%$) are observable upon application of a magnetic field. The decay is roughly mono-exponential in both cases, but upon careful examination, a different behavior of type $\exp(-(2\tau/T_2)^\alpha)$ is observed (b).

optics, as has been done in other studies[1]. However, considering the short values for T_2 measured, we can still neglect this effect when investigating dephasing in our samples.

For nuclear spin mediated decoherence of single NV$^-$ centers in crystals with natural carbon isotope abundances, a relaxation time $T_2 > 400\,\mu$s and a decay exponent α between 3 and 4 is reported [102, 105]. This is both in stark contrast to our findings in nanodiamond, which strongly indicates that another decay mechanism is present that cannot be described by nuclear spins *only*. In our samples this mechanism seems to strongly dominate decoherence. To underline our experimental findings, we have to note that similar mono-exponential decays have been reported (but not discussed) before for nanodiamonds (see, e.g., [39]). On a related note, the long time coherence decay of P:Si qubits with natural ^{29}Si content sometimes shows a very similar behavior, which was also reproduced by joint cluster expansion calculations [114, 115], but a sophisticated microscopic model still has to be developed for our case.
Please note that neglecting decoherence from nuclear spins in our samples should not be done in any case. For example, due to the enhancement of the precession frequency of nearby nuclei by the pseudo-nuclear Zeeman effect (see section 2.6), nuclear spin diffusion is strongly dependent on the magnetic field orientation. As

[1] e.g. [41], F. Jelezko: private communication

a result, it was reported for bulk diamond that at perpendicular field T_2 drops to a few ten μs [116]. Thus, even in our samples nuclear spin diffusion might limit coherence at higher misaligned fields. Since we mostly observe a fast mono-exponential decay even for parallel fields (see figure 3.2a), we have to conclude that in this case decoherence is dominated by an additional physical process present in our samples, which also has not been treated before.

From the epr literature mono-exponential decay of coherence is mainly known from the case of instantaneous diffusion [89], which requires that the refocussing microwave pulse (π pulse) flips a second spin, e.g. by driving a forbidden epr transition ($\Delta S = \pm 1,\ \Delta I = \pm 1$). We consider this mechanism possible, but unlikely, since it is most effective for like spins, the presence of which can be excluded in our sample. We therefore consider another explanation. Looking carefully at some of our echo decay curves (e.g. figure 3.2b), we observe a slightly increased exponential behavior ($1 < \alpha < 2$) at the beginning, while the long time behavior can be described better with a square root exponential ($\alpha = 0.5$). As stated earlier, this matches the theory of spectral diffusion [112], where the correlation time within the bath (e.g. flipping rate) approaches the decoherence time.

It was shown very recently that in diamond with a high defect concentration (many electronic impurities) mono-exponential curves are observed for magnetic fields aligned with the center axis, while a square-root exponential decay is observed for perpendicular field orientation [116]. Unfortunately, since these observations are made on ensembles of NV^- centers, the authors attribute this effect to an average over a quasi-Lorenzian distribution of different coherence times. Seemingly, this explanation can not easily be applied to single centers, but as a matter of fact it is still possible considering time averaging.
The presence of slowly fluctuating interactions *within* (note: not with) the spin bath can lead to a distribution of spin flip-flop rates, resulting in varying values for T_2 between different experimental shots. Averaging in time over this distribution can, again, lead to a different (and faster) relaxation behavior.

Conclusions

In conclusion, we have found a new decoherence process in our samples that is much stronger compared to the inherently present decoherence induced by nuclear spin diffusion. Without external magnetic field, T_2 is limited to a few microseconds, while a small parallel magnetic field is able to prolong coherence by a factor of 20. The decay behavior can be described by spectral diffusion and is very similar to the one observed for NV^- ensembles in electronically impure bulk diamond [116].

This decoherence mechanism strongly limits the performance of "dirty" diamonds in quantum applications. However, a dirty environment cannot always be avoided. In consequence, it is important to see if decoherence can be overcome, e.g. by dynamically decoupling the spin from the surrounding spin bath.

3.2 Dynamic decoupling

3.2.1 A brief introduction to dynamic decoupling

From the definition of the spin-lattice and spin-spin relaxation time it can be concluded that, if an experimental pulse sequence is applied that preserves coherence by decoupling from random noise sources, also T_1 and T_2 can increase to a certain extent. As a result, starting from the early days of magnetic resonance, multiple proposals were made which focussed on prolonging relaxation time by dynamically decoupling (*DD*) a spin from various environmental influences. The simplest approach, which forms the basis of other techniques, consists of a single refocussing pulse (Hahn echo), and is today considered as the standard for T_2 measurements since it typically decouples from experimental imperfections like inhomogeneous magnetic fields. Its effect has already been discussed in the previous chapters.

The next complex approach is a periodic repetition of refocussing π pulses that was first applied by H.Y. Carr and E.M. Purcell in 1954 [117] in the context of nuclear magnetic resonance (*NMR*). In its original realization all pulses have the same rotational axis (same phase) in the Bloch sphere. It was soon found that variation of the phase ϕ resulted in better pulse error correction, leading to the more modern periodic Carr-Purcell- Meiboom-Gill (*CPMG*) sequence [118]. Further development of pulse sequences for increased resolution in NMR lead from periodic dynamic decoupling (*PDD*) sequences like CPMG to optimal control theory [119] where amplitudes and phases of the pulses are varied deliberately in order to iteratively find a configuration which minimizes dephasing. Application of optimal control theory to epr is still suffering from many technological problems due to greater effort in controlling microwave pulses compared to radio frequencies. This is why traditional approaches of dynamic decoupling using analytically calculated sequences are still of great importance in epr.
Lately, various pulse sequences have been proposed and experimentally demonstrated to dynamically decouple spin systems from a noisy environment[120–124]. The benefit of these methods compared to PDD depends strongly on the nature of the dephasing process. The traditional CPMG sequence is known to reduce the effects of a number of processes, most notably nuclear spin diffusion induced by hyperfine interaction [118]. The theoretical limit of CPMG is given by the effect of a train of subsequent pulses with vanishing inter-pulse delay which are phase-

shifted in plane by $\pi/2$ (*'Y pulses'*) against the initial pulse (*aka 'X'*). This is called spin locking [125] and the decoherence time approaches the rotating frame relaxation time $T_{1,\rho}$ [125]. The applicability of PDD has very recently been verified for NV centers in ultra-clean bulk diamond as well [126–128].
Newer concepts propose non-periodic refocussing patterns for increased performance compared to PDD. Two of the newest approaches are concatenated dynamic decoupling (*CDD*) [120, 129] and Uhrig dynamic decoupling (*UDD*) [130]. Both pulse patterns have dedicated strengths and weaknesses in decoupling from the environment. CDD is based on recursive concatenation of elementary dynamic decoupling sequences in order to increase their efficiency, each concatenation or recursion level removing errors left uncorrected by the previous level. While this hierarchical error correction can be pushed up to arbitrary precision even for realistic bounds on bandwidth and strength of control pulses [131], a disadvantage is given by the exponentially increasing number of pulses at rising recursion level. On the other hand, Uhrig analytically developed an optimal pulse spacing that will allow to achieve the largest decoupling effect from an unknown source of decoherence by using a minimal number of pulses. In the N-pulse UDD sequence of total duration T, the kth π pulse is placed at $t_k^{(N)} = T \sin^2(\frac{\pi}{2}\frac{k}{N+1})$.
To describe the effect of dynamic decoupling (DD), we follow *Hall et al.* [60, 132] and describe all interactions as an effective time-dependent magnetic field $B_{env}(t)$, which may be decomposed as a Taylor series in t:

$$B_{env}(t) = \sum_{k=0}^{\infty} a_k t^k, \quad \text{where } \forall\, k : a_{k+1} t < a_k. \tag{3.4}$$

The Hahn echo sequence removes the effect of static field on the system, which is the first term ($a_0 = 0$), and reduces all the other terms. The CPMG (or PDD) pulse sequence corrects in principle only for phase errors (T_2 processes), while CDD and UDD can be made to correct for spin-flips (T_1 processes) as well if pulses of different phases (including Z, which can be realized as composite pulses) are used [133]. As stated in the last section, for an NV^- center in bulk diamond, spin-lattice (T_1) relaxation is quite ineffective due to the rigidity of the diamond lattice. Thus, decoherence can be understood in terms of T_2 processes due to interaction with the spin bath, be it nuclear [105] or electronic [134]. In the nano-diamonds, we find $T_1 \gtrsim 100\,\mu$s, far in excess of $T_2 \lesssim 20\,\mu$s. Therefore, and in order to enable quantitative comparisons, we have used here the single-phase versions of the DD sequences as well, which correct only for pure dephasing.
In order to remove the nth term from eqn. 3.4, at least $(n+1)$ π pulses are needed [132]. Similarly, a CDD sequence of recursion level ℓ can cancel all terms up to $\ell = k$, albeit with a number of pulses growing as roughly $N \sim 4^\ell$ [120, 135]. However, as errors are inherently introduced with each pulse, the UDD sequence

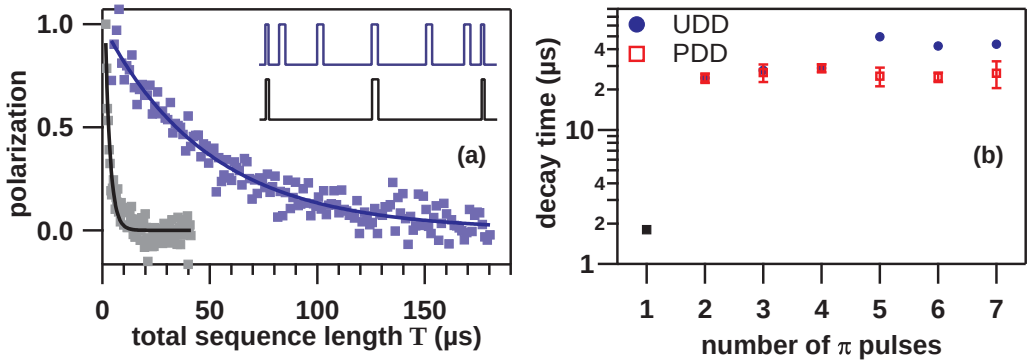

Figure 3.3: Comparison of coherence preservation by PDD and UDD pulse sequences. (a) Decay curves for UDD5 and UDD1 (= Hahn echo) as a function of total sequence length T; the inset shows the corresponding microwave pulse sequences. (b) Decay times obtained from fits in (a) as a function of the number of π pulses.

promises better performance in practice since it requires a much smaller number of pulses.

3.2.2 Experimental results on nanodiamonds

The experiment was performed using the setup described in section 2.4.2. The sample (MSY by Microdiamant, nominal diameter 25 nm) was prepared as described in section 2.4.1, followed by an additional surface oxidation step by heating at air at $T = 400\,^{\circ}\mathrm{C}$ (for details, see section 4.1) for sample A. In addition, a slight modification was added to the microwave setup. For proper execution of the CPMG ('PDD$_y$') sequence, a secondary microwave channel was constructed that was phase-shifted by 90° using a mechanically tuned delay line ('Y channel'). We have investigated the effect of dynamic decoupling at zero static magnetic field ($< 0.1\,\mathrm{mT}$). In addition, control experiments under application of a small (~ 10 mT) constant parallel field have been performed.

Figure 3.3 shows the effect of PDD and UDD pulse sequences on center A. Similar to the Hahn echo, all decay curves showed approximately mono-exponential decay. It can be seen clearly that for both sequences a massive increase of coherence by a factor of 10 is observed already at the second recursion level[2]. This means

[2]Note: UDD/PDD1 is a Hahn echo, while PDD2 and UDD2 are equivalent to each other.

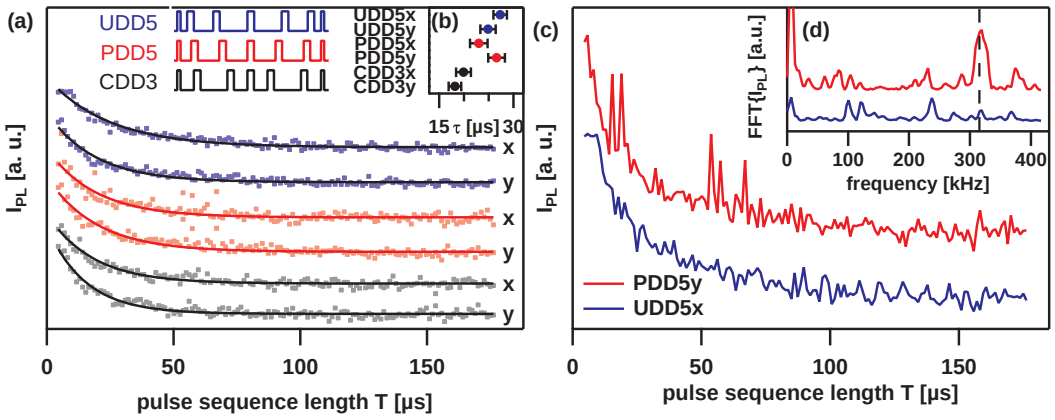

Figure 3.4: Comparison of UDD, PDD and CDD at different rotational axes (x,y) of the refocussing pulses (a) coherence decay curves, the inset shows the corresponding pulse timing. (b) mono-exponential decay constants derived from (a). (c) Spin modulation effects on the two optimal sequences PDD5y (upper traces) and UDD5x (lower traces). (d) Modulus of the fast Fourier transform of the decay curves (c). Note that no modulation effects are expected for UDD5.

that a second refocussing pulse has an effect somewhat similar to the application of a magnetic field along the center axis (see section 3.1). At higher recursion levels one notes that UDD increases the T_2 by another factor of two, while PDD seems to saturate for higher levels. In addition, a slight even-odd asymmetry is observed in the case of UDD, which can be attributed to accumulation of unwanted echoes such as stimulated and refocused echo that may interfere with the wanted primary echo [102]. This effect can in principle be compensated e.g. by phase cycling, which we verified for simpler sequences (UDD3,4).
Comparing naively the effects of UDD_x and PDD_x, the latter seems to be less effective. One has to consider, though, that the best effect for PDD is expected for Y phase refocussing pulses. In this case PDD is equivalent to the CPMG sequence. Using X pulses only, the sequence will suffer strongly from pulse errors which are corrected for CPMG. On the other hand, UDD was optimized for constant phase. Thus, UDD_x is expected to provide better decoupling than UDD_y. Owing for this fact, we made a control experiment on another center using both 'X' and 'Y' phases for PDD as well as UDD. In addition, the CDD technique with the same number of refocussing pulses was also implemented with both phases. The resulting decay is displayed in figure 3.4a.

As expected, UDD_x performs better than UDD_y and PDD_y better than PDD_x. Furthermore, it seems that the better versions of UDD and PDD are equivalent

in performance in this case, while CDD seems to be less effective for any phase. We observe that UDD works usually slightly better for most centers. This was observed for several samples, even though they had quite different decay times. In addition, the samples investigated also had rather different scaling behavior with the number of pulses; while for some samples, sequences up to $N = 8$ could still improve the decay time, this was not the case for other samples (we remark here that our pules are quite "soft" ($\sim 100\,\mathrm{ns}$) in comparison to other works). The most extreme case was one NV^- center for which even $N > 3$ was worse than $N = 3$ (data not shown) no matter which pulse sequence was applied.
The mono-exponential behavior observed for all decay curves holds even for NV^- centers with aligned fields and clear ^{13}C-ESEEM signatures in the Hahn echo decay (see e.g. fig. 2.20), which are of course suppressed by dynamic decoupling in the general case. In another sample with an unmodulated Hahn echo decay, modulation effects could be 'distilled' with the regular PDD sequence (see fig. 3.4b).

Discussion

Experimental work has shown that UDD outperforms PDD for trapped ions [123] as well as for solid state γ-irradiated malonic acid [124]. Since the NV^- center in nano-diamonds is a solid-state system embedded in a particularly noisy environment, it is important to experimentally investigate which dynamic decoupling scheme is optimal for an extension of coherence. This was done quite recently for the case of clean bulk diamond with a well-behaved nuclear [127] or electronic [126] spin bath, and it was found that the UDD sequence does not perform as well as the PDD sequence. A disappointing performance of CPMG was reported for nanodiamonds [76], where it could only enhance the T_2 times by a factor of two. This seems to limit the usefulness of nano-diamonds in quantum technological applications such as magnetometry.
These recent results are in stark contrast to our findings, which show that both PDD and UDD can significantly prolong T_2 for nanodiamonds at zero external magnetic. Our results lead to the conclusion that UDD performs as well as, or even slightly better than, the periodic CPMG dynamical decoupling (PDD). We attribute these differences to the different nature of the spin environment in nanodiamonds as discussed earlier. Oscillatory decay curves are observed for periodic sequences with $N = 5$, suggesting that a part of the spin bath recouples coherently under dynamic decoupling, leading to 'revivals' similar to the situation in bulk diamond [127]. It is noteworthy that even the simple PDD_x was recently found to perform better than UDD for clean diamond by Ryan et al. [127].

Conclusions

In conclusion, we have experimentally investigated that UDD and PDD sequences on NV^- centers in nanodiamond shows a clear effect of preserving electron spins coherence for small numbers of refocussing pulses ($N < 8$) at zero static magnetic field. At larger numbers of pulses, T_2 seems to converge far below the limit given by T_1. The source of decoherence which is responsible for this limit is unknown. For most centers, UDD showed a slightly better performance than PDD at constant phase for the same number of pulses. Both findings seem to be in stark contrast to recent published results [76, 126, 127], but might be explained by the difference in samples and experimental conditions. Since only *Nayednov et al.* [76] did experiments on nanodiamonds, but obviously not in zero field, the striking effect of second-order dynamic decoupling couldn't be observed. Regarding nanodiamonds, the difference of the spin bath in our samples compared to bulk diamond has already been broadly discussed in section 3.1. Now, the results of dynamic decoupling support this conclusion. In bulk diamond, PDD was reported to be significantly better at decoupling than UDD by several authors [76, 126, 127]. This was attributed to the fact that the fluctuations of the described spin baths have a "soft cut-off", a situation for which UDD is known not to be optimal [136]. Moreover, both types of sequences may suffer from pulse imperfections, which can be avoided in case of PDD by shifting the refocussing π pulses in phase by $\pi/2$ relative to the bracketing $\pi/2$ pulses. UDD, on the other hand, is a sequence designed for ideal pulses and has been claimed to be less robust to pulse imperfections [126]. This can be easily understood for sequences with a large number N of pulses as the delays between the first (or the last) pulses get ever shorter. One should note that in both reports the superiority of PDD over UDD became most evident at $N > 64$. The best coherence gained by UDD5 was $T_2 = 53.6\,\mu$s, which is of great importance for the technical applicability of nanodiamonds, be it as a nano-probe magnetometer or as a part of quantum information technology.

3.3 Summary and outlook

We observed that T_2 in nanodiamonds is much shorter than reported for most types of bulk diamond. At zero field, T_2 is extraordinarily low (a few μs). A small magnetic field can increase coherence by a factor of 10, with little impact of the field orientation. The same effect can be achieved by second-order dynamic decoupling. At higher and well-aligned fields as well as when using higher level dynamic decoupling, we observe no further increase of coherence, which indicates the presence of an additional source of decoherence, that constrains T_2 to a maximum of a few 10 μs. The decay behavior is roughly mono-exponential under all

conditions, although slight deviations between short- and long-time behavior could be observed, which still allows to assign the decay mechanism to spectral diffusion.

Our results suggest that the spin bath in nanodiamonds may be significantly different from the bulk situation. Here, the two widely discussed baths for single crystalline diamond are the nuclear (^{13}C) bath, predominant in ultrapure samples, and the (substitutional N) electron spin bath, which may be in part unavoidable if conversion of implanted N to NV^- centers is not complete. For the case of nanodiamonds additional decoherence sources, e.g. at the crystal surface might be considered. In order to distinguish intrinsic from extrinsic sources, it is possible to manipulate the diamond surface and environment, which will be discussed in chapter 4.

Chapter 4

Investigation of the NV^- center environment via optically detected magnetic resonance

As described in the previous chapters, the extraordinary spin coherence and optical properties of the NV^- center in diamond allow for efficient spin polarization and detection via ODMR [37–39]. In consequence, construction of magnetic field probes [41, 57, 58, 137] and quantum information devices [44, 47, 108, 138, 139] from single NV^- centers has been demonstrated experimentally.

For both kinds of application, centers located only a few nanometers beneath the diamond surface ('*shallow*' centers) are of specific interest. In particular, a magnetic field probe that hosts a single spin should be as small as possible to achieve optimal spatial resolution combined with minimal probe-sample distance. This is especially true for magnetic resonance imaging of cells using small nanodiamonds [137]. In the case of quantum information devices, shallow centers allow more degrees of freedom in device architecture. Coupling to plasmons [50, 140], microoptical cavities [140, 141], superconducting flux qubits [142], and molecular qubits are just a few examples from the broad range of possibilities where shallow centers are needed.
Despite this, only few studies exist that focus on physics of shallow NV^- centers and their interaction with the environment, most of them focussing on luminescence properties. In particular, it has been observed that shallow NV^- centers can be neutralized to NV^0 by charge transfer, depending on the surface termination [66, 74, 75, 77]. Regarding spin physics it is only known that decoherence of the NV^- is strongly enhanced[1]. In order to enhance coherence of shallow NV^- centers, it is important to understand the effects of external modifications on the spin.

[1] F. Jelezko: private communication

Motivation: a molecular-solid hybrid quantum computer

Ultimately, if all sources of decoherence outside the diamond can be deactivated, e.g. by perfect environment control, it might be even be possible to build hybrid quantum spin devices which couple to defined external spins, for example molecular qubits. One such device would be a quantum computer, consisting of tailored molecules to encode multiple spin qubits (e.g. from endohedral fullerenes [143], see section 4.2.2), which are coupled to single NV$^-$ centers in diamond acting as readout bus [144]. The advantage of such a device lies in its presumably easier construction compared to a 'diamond-only' quantum computer. This is because, despite the outstanding properties of the NV$^-$ center regarding application in quantum information, for large scale quantum computing a great number of technical difficulties remains to be solved [138]. One of the most critical demands is the controlled generation of single defect with sub-nanometer precision. While this might technically not be impossible and successful approaches towards high precision single ion implantation have been made [43, 145], there is still a long way to go. On the other hand, molecular qubits (for example paramagnetic molecules) do not have this problem since molecular chemistry leads to much better defined systems. Unfortunately, up to now no molecular qubit candidate is known that offers a working single spin readout. Thus, combining the advantages of both systems seems to be a logical choice. The study presented in this chapter will present steps towards this specific goal.

4.1 Influence of the atmosphere on decoherence of near-surface centers

4.1.1 Control of the nanodiamond surface

For experiments probing the environment it is important to start from a defined diamond surface. Compared to bulk diamond, this is even more critical in the case of small nano-particles, where large strain is present in addition to all possible surface orientations. Note that even single electron spins, e.g dangling bonds, can result in decoherence and should ideally be avoided. In order to achieve this, after preparation of nanodiamonds as described in section 2.4.1 another cleaning step was applied that results in an oxygen terminated surface. For oxidation of the surface, either acid cooking [77] or heating in an oxygen containing atmosphere can be applied [146]. The latter approach takes advantage of the fact that sp^2

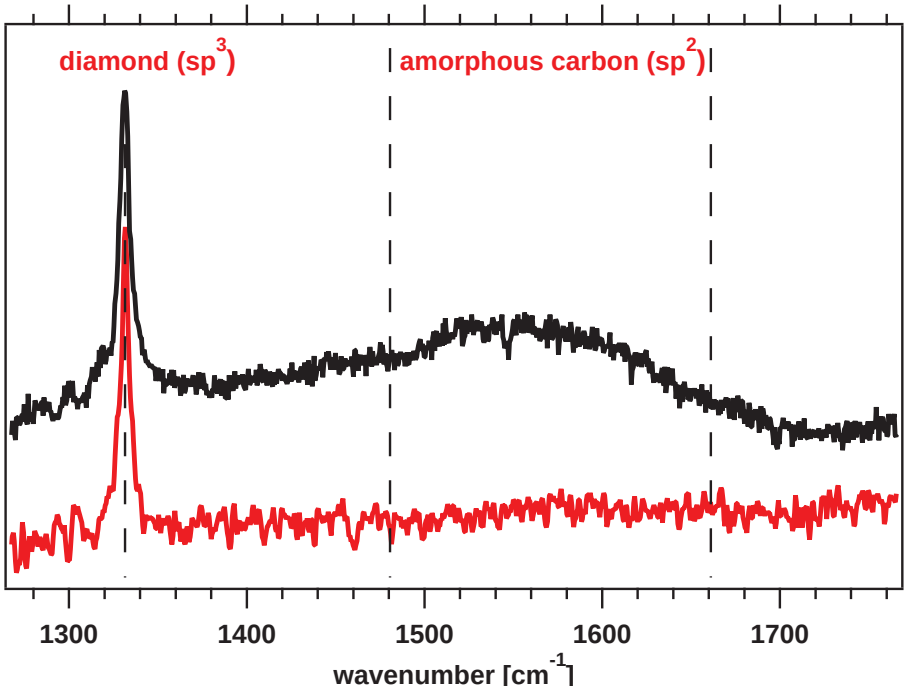

Figure 4.1: Raman measurements of nanodiamond sample. Excitation wavelength 514 nm. Top graph: untreated sample. Aside from the diamond peak, which occurs at 1332 cm^{-1}, the spectrum shows a broad peak at 1560 cm^{-1} that can be assigned to amorphous carbon. Bottom graph: Oxidized sample after treatment at air for four hours at 450 °C. No peak at 1560 cm^{-1} was found at different sample spots and excitation wavelengths (488, 514 and 633 nm). Measurements have been performed by C. Casiraghi (FU Berlin).

carbon can be oxidized at lower temperature than diamond [147].
For the experiments reported in this chapter, the samples were heated for two to four hours at 400 to 450 °C at ambient conditions. Comparing the Raman spectra of the nanodiamonds (see figure 4.1) it can be seen that in addition to the sharp peak at 1332 cm^{-1} which corresponds to sp^3 carbon, as expected for diamond, a broad peak at ~ 1550 cm^{-1} is present in the untreated sample, but disappears after the heating process (note that the absolute intensities/areas cannot be directly compared). This peak can be assigned to amorphous (sp^2 type) carbon. While intrinsic amorphous carbon cannot be excluded it is more likely that this signal results from a cover layer of the nanodiamonds.
The spin-spin relaxation time T_2 was measured using a standard Hahn echo sequence before (after) the treatment on a different set of centers at zero field and

ambient conditions. Averaging the decay constants of 10 centers before and after oxidization, a decay constant of $T_2 = 4.2\ (3.8)\ \pm 1.5\,\mu$s was found. So, no significant change in T_2 was observed as a result of the oxidization. Still, since the amorphous carbon might form a passivation layer between the diamond and the surface of the nano-particle, and thus increase the distance of externally added spins to the NV^- centers, the amorphous carbon was removed for subsequent environmental studies.

4.1.2 Influence of the atmosphere

Before studying the effect of adsorbed molecules on the surface, we first have to investigate the effect of the atmosphere on the NV^- center. This is very important since most investigations on NV centers are performed at ambient conditions. On the other hand, molecular oxygen has a triplet ground state and is usually considered as a strong relaxant in epr [89]. The same holds for water, which is always present in the environment.
In order to study the influence of the surrounding atmosphere on T_2, the glass substrate was covered by a plastic flow cell with 1 mm gas entry and exit ports connected to a 1 meter capillary exhaust (I.D. 0.7 mm, see fig. 4.2). The flow cell was equipped with a 20 micron antenna, rf connectors and an optical window at the top to reduce scattered light from the laser. In order to seal the cell, a thin polytetrafluoroethylene (PTFE) foil was placed between the cell wall and the sample. We used nitrogen and oxygen gas which could be humidified at will by a bubbling the gas through a heated water vessle. The gas flow rate was monitored by observing the change in the objective focus induced by bending of the sample due to the pressure. For the experiment, the flow rate was set as low as possible, while still being able to observe a nonzero (~ 100 nm) change in focus. Taking into account the diameter of the cell (10 mm) and the thickness of the glass (120 μm) it can be deduced that pressure changes can be neglected.

Figure 4.3 shows consecutively the measurements of the phase relaxation time constants of 4 representative NV^- centers out of 10 investigated on the oxidized sample. It was observed that about half of the centers showed no significant response to the atmosphere (e.g. NV03, NV04), while the others responded more strongly (e.g. NV01, NV02). In all centers showing a response, the relaxation time increased whenever a gas stream was applied, regardless of which gas was employed. Surprisingly, looking briefly at our data, it may seem that oxygen has a stronger effect on most centers than nitrogen, which is the opposite from what is expected. On the other hand, it has to be noted that the experiments were all performed in the same order, going from air to nitrogen to oxygen. Test measurements in air after the oxygen measurement revealed a decrease of the relaxation time, proving

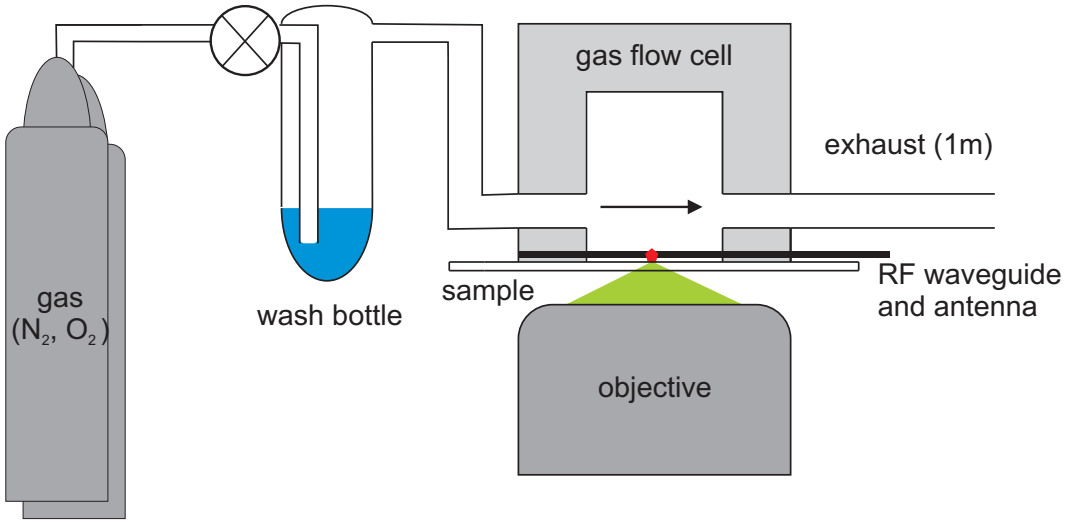

Figure 4.2: Experimental setup (not to scale) for studies on nanodiamonds in different atmosphere. A gas flow cell can change the atmosphere to air (gas inlet through exhaust), nitrogen and oxygen. The gases can be humidified and heated through a wash bottle which is inserted / removed at purpose.

the effect was completely reversible. Yet, if the measurement was performed only a few minutes after the change of atmosphere, the relaxation time was still slightly higher compared to the first measurement.

These observations lead us to suspect that the effect might be related not to the nature of the gas, but the humidity of sample, since water as well as dissolved oxygen in water can also lead to strong relaxation [148]. This was verified by using humidified gas. The result is displayed in figure 4.4. It can be seen that in addition to the slow time constant a faster decay component is present. This significantly reduces T_2 by more than a factor of two from 8.4 ± 0.2 to 3.2 ± 0.2 microseconds. Thus, compared to ambient conditions ($T_2 = 3.6 \pm 0.1$ μs) decoherence induced by wet gas is is even slightly stronger.

Surprisingly, a short time after wetting, the ODMR effect of the center vanished irreversibly. This can only be explained by a kind of chemical reaction. One possibility is that the water induced a - probably photoinduced - change of the charge state from NV^- to NV^o, which has been reported earlier for centers in small ($\sim$ 5 nm) nanodiamonds [52]. Other possibilities are quenching of the ODMR

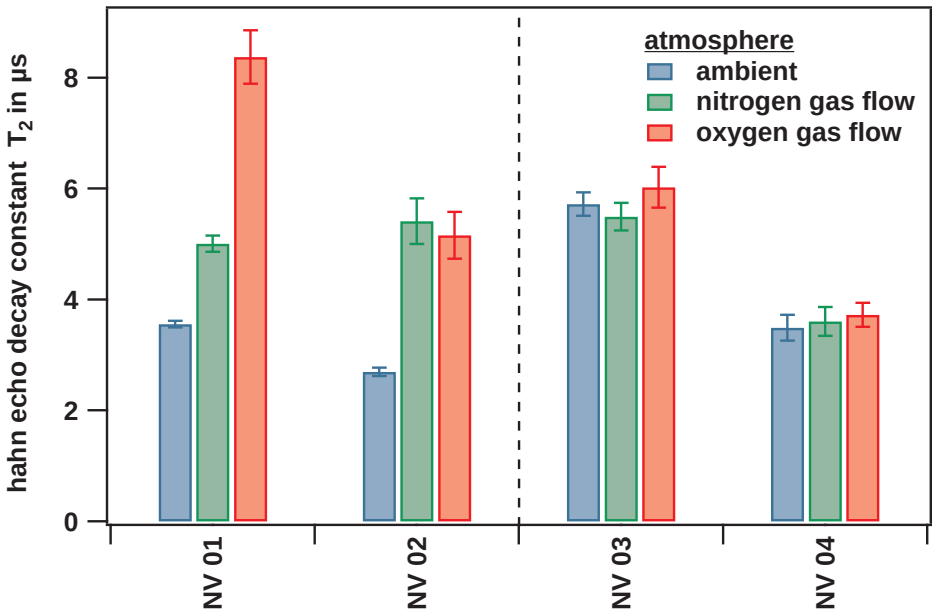

Figure 4.3: Echo decay constants of 4 selected centers out of 10 measured at different atmosphere. Some centers (e.g. NV01 and NV02) show an increase in coherence up to a factor of 2. Others (e.g. NV03 and NV04) show no significant response to atmospheric changes. The atmospheric changes are plotted in chronological order from left to right.

signal due to spin mixing, as observed for broken symmetry [88], or strong line broadening due to massive decoherence that reduces the ODMR intensity below our detection limit.

Due to the quenching of the ODMR signal it was not possible in this instance to make a control experiment using wet nitrogen to obtain any information if the water itself, or dissolved oxygen, is the source of decoherence. This is certainly an interesting area for further studies.

In conclusion we have shown that humidity is a relevant factor in the phase relaxation of surface-near nitrogen vacancy centers. It seems that at ambient conditions a small layer of water automatically forms on the surface that can affect the spin relaxation of the centers. This represents an easy way to find surface-near centers, which should provide useful also in the case of shallow implanted centers in bulk diamond.
About half of the centers in our nanodiamonds (25 nm mean size) do not respond to atmospheric changes and have to be considered as "deep centers". Yet, the

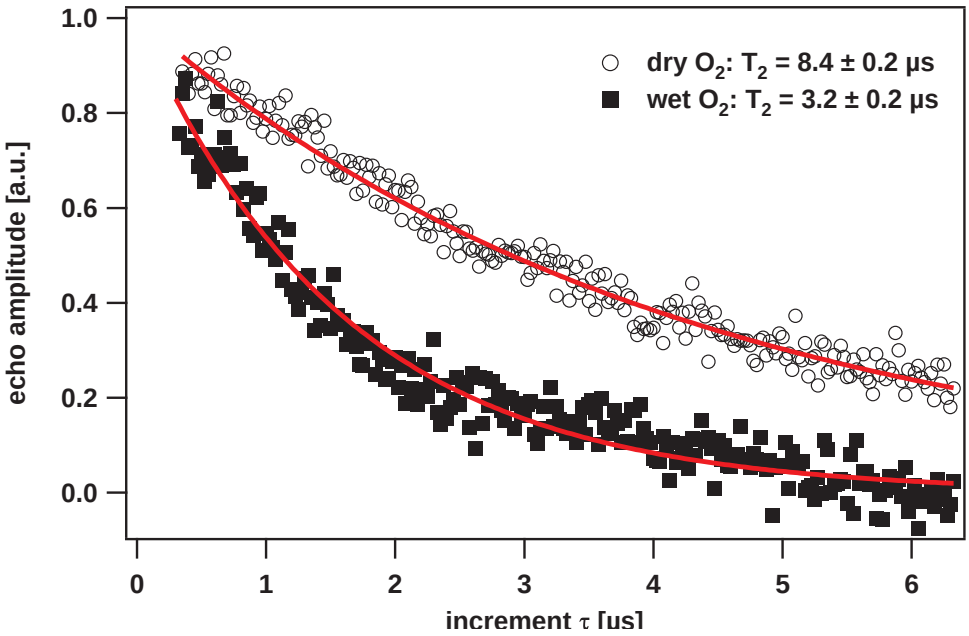

Figure 4.4: Influence of humidity on phase relaxation of NV01. After the the wet measurement the ODMR signal of the center was suddenly no longer observable.

rest of the centers do show an observable response (up to a factor of 2) to surface drying and can be considered as good candidates for coupling experiments or surface probes. Still, even in the case of deep centers or dry atmosphere, relaxation was still much shorter (< 10 μs) than observed in electronically clean bulk diamond. Furthermore, the response of different centers to the atmosphere was not correlated with their initial T_2. Thus, aside from the strong effect from water, there are still other sources of decoherence present. Observing similarly short T_2 for supposedly shallow and deep centers, it is more likely that these sources are electron spins inside the nanoparticle than on the surface.
This is also supported by our relaxation studies (section 3.1.1). There, we have learned that we have a spin-rich environment surrounding the NV center, and the relaxation process is most likely spectral diffusion. Since we know that it is sufficient to increase intrabath interactions to reduce the relaxation time, additional spins which mediate the interactions can be considered a sources of decoherence. Thus, one can assume that either protons or a high concentration of oxygen is responsible for decreased coherence of the spin of nitrogen vacancy centers next to the diamond surface.

4.2 Effects of paramagnetic molecules adjacent to NV^- centers

Since an overlap of the wave functions of a molecule and a (localized) solid state defect seems very unlikely, the strongest interaction between the spins of both systems will be the magnetic dipolar interaction.
For small spin quantum numbers, like in the case of NV^- centers and molecular radicals, this interaction becomes very small at distances larger than a few nanometers. It follows the equation

$$\mathbf{H}_{12} = \vec{S}_1 \mathbf{T}_{12} \vec{S}_2 \tag{4.1}$$

where the $\vec{S}_1$ and $\vec{S}_2$ are the spin vectors of the NV^- center and the radical respectively. Considering only the zero-field interaction of the NV^- center and a small magnetic field the total Hamiltonian can be solved omitting non-secular terms since the resonance frequencies are very different. Then the dipolar splitting energy E_{12} can be written as

$$E_{12} = S_1 T_{12} S_2 = T_{12}^{(0)} \left(3\cos(\theta_{12}) - 1\right) S_1 S_2 \tag{4.2}$$

with θ_{12} being angle between the center axis and the axis crossing the center and the molecule. $T_{12}^{(0)}$ has the form

$$T_{12}^{(0)} = \frac{\mu_0}{4\pi} \frac{\hbar \gamma_1 \gamma_2}{r_{12}^3} \approx \frac{52 \text{ MHz}}{r_{12}^3/[nm]^3} \tag{4.3}$$

where μ_0 is the magnetic constant, $\hbar$ is Planck's constant, γ_1 and γ_2 are the gyromagnetic ratios of the spins and r_{12} is the distance between the spins.
Taking into account an optically broadened line with a typical FWHM of 10 MHz like in the case of continuous wave ODMR one can conclude that in order to observe a coupling between the spins the molecule has to be within about 3 nm even at optimal angle θ_{12}. At optimal resolution, using low excitation power as displayed in figure 2.18, a splitting of 1 MHz can be observed. Since the dipole-dipole interaction follows an r_{12}^{-3} law, a direct observation of a line splitting requires an optimal configuration. Yet, line broadening, echo modulations or decoherence are also possible effects, which can be investigated despite of broadened lines.

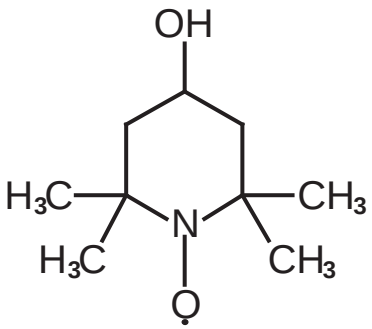

Figure 4.5: Chemical structure of 4-hydroxy-2,2,6,6-tetramethylpiperidine 1-oxyl (TEMPOL)

4.2.1 Centers coupled to multiple TEMPOL molecules

Using an ensemble of paramagnetic molecules acting as a spin bath instead of a single spin promises to be a good test bed for checking if a coupling between the NV^- center and paramagnetic molecules is possible and to rule out that the distance between the spins is too large. In order to derive an expression, we neglect the angular function from equation 4.3 and replace it with an appropriate average value. The nitroxide radical TEMPOL (see figure 4.5), which has a stable spin of 1/2, provides convenient properties because it is one of the smallest spin labels available. In addition, it is stable at room temperature and absorbs/emits only weakly within the visible spectrum [149], and it is soluble in water, which allows for a good coverage of the hydrophilic nanodiamonds and glass substrate. In order to distinguish an NV^- center coupled to TEMPOL from other centers coupled to intrinsic spins, it is necessary to observe the change in the spectrum in situ, since statistics over many centers would be too time consuming. For this purpose the spectra from a set of about 10 centers were measured before adding TEMPOL dissolved in deionized water ($c = 0.1$ g/l) using a syringe. After a 20-minute waiting period needed for the water to evaporate, only a slight homogeneous increase in luminescence was observed in the fluorescence microscope (see figure 4.6). NC-AFM measurements (see figure 4.7) of a test sample also revealed no additional structure after addition of TEMPOL, but a slight smoothing of the sample was observed in the height contrast. Reference measurements indicate that an effect from the tip can be excluded. From the sample area (1 cm^2), volume and density of TEMPOL ($\rho = 0.912$ g/cm^3) the thickness of the film should be approximately 15 nanometers. Thus, it can be concluded that the TEMPOL forms a homogeneous layer on the sample.

When comparing the cw ODMR spectra taken before and after addition of TEM-

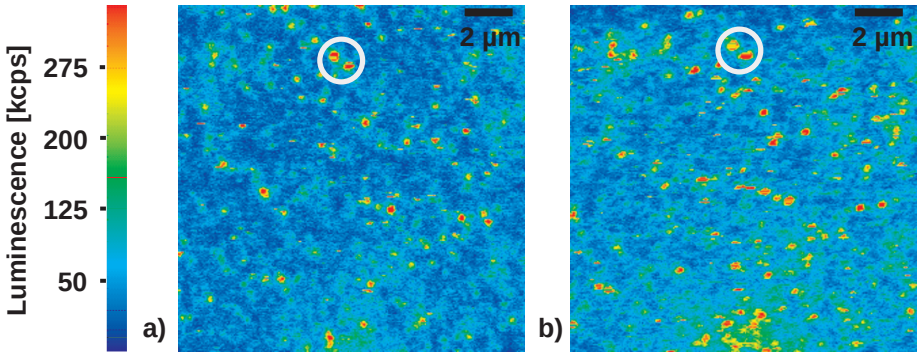

Figure 4.6: Fluorescence image of a nanodiamond sample before (a) and after (b) addition of 10 μl of TEMPOL in deionized water ($c = 0.1$ g/l). The white circles represent a guide to the eye.

POL a significant change was observed only on some ($\sim 50\%$) centers (see figure 4.8). In none of the cases a broadening of the lines was found. On the other hand, in about half of the centers a reduction of the ODMR effect was observed, ranging from slight decrease to complete quenching. This effect was accompanied by a reduction of luminescence. Yet, the luminescence did in no case drop below the former level at spin resonance before addition of TEMPOL.

Discussion

There are multiple ways of explaining the reduction ODMR contrast and luminescence. Since the effect was only observed on some of the centers, an experimental error (i.e. a change in the position of the microwave antenna) can be excluded. Looking at the 5-level model (see section 2.2), an increase of the inter-system crossing rates of the excited state S_z level to the ^{1}A state would explain a reduction of light due to reduced spin polarization. This would also lead to a decreased ODMR contrast. On the other hand, the same effect would be expected in the presence of an electron spin bath that should reduce the spin-lattice relaxation time T_1 due to spin flip-flops. There are two arguments against the latter explanation. First, these flip-flops are not energy-conserving due to the zero-field splitting of the NV$^-$ center which makes them highly inefficient. More significantly, since the ODMR lines are already broadened under the laser excitation, a strong decrease of T_1 should be observable in the line width. This indicates that an increased inter-system crossing induced by spin mixing might indeed take place. Unfortunately, since this experiment was performed on the setup shown in figure 2.8, a more

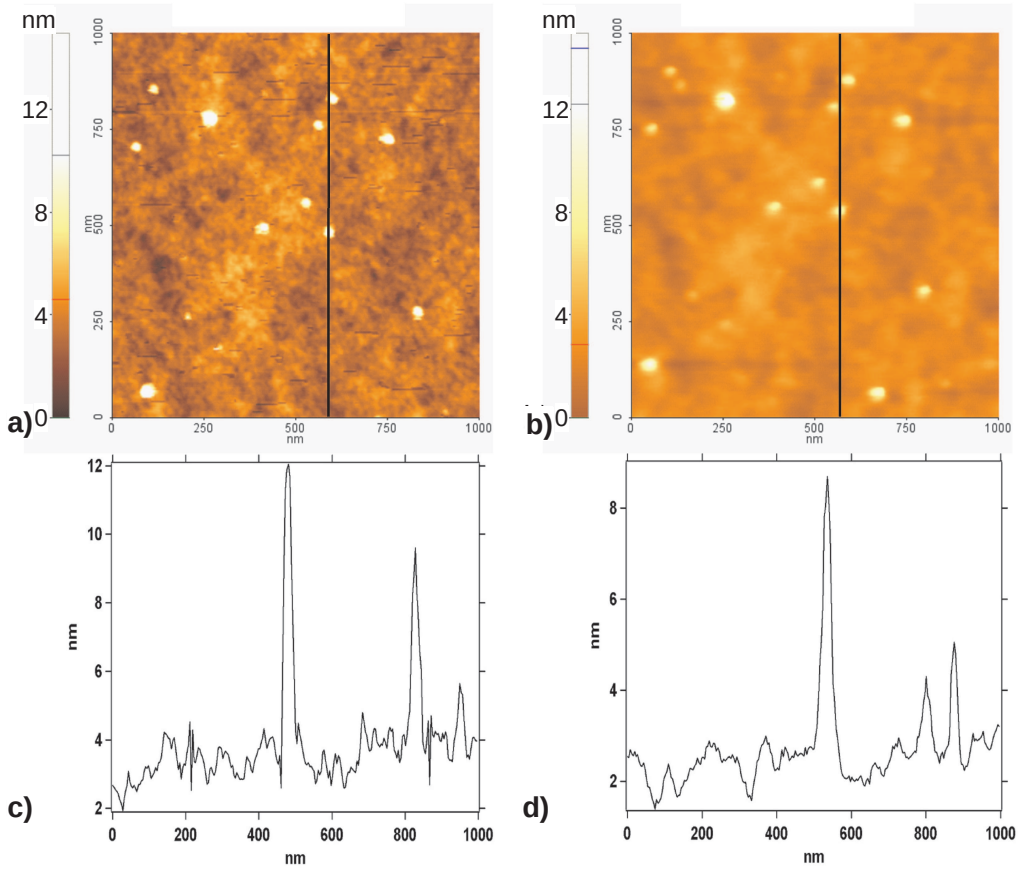

Figure 4.7: NC-AFM topographic image a sample before (a) and after (b) addition of 15 μl of TEMPOL in deionized water ($c = 0.1$ g/l). c) and d) show a profile along the black line displayed above.

detailed investigation, e.g. by direct measurement of the excited state lifetime was not possible. Yet, the results show that, if somewhat small, there is a finite interaction between molecules on the surface and about 50 % of the NV$^-$ centers.

4.2.2 Centers adjacent to N@C$_{60}$

In order to observe couplings between the NV$^-$ center and single electron spins with long spin relaxation time, we applied the same procedure as for the case of TEMPOL to a solution of N@C$_{60}$ in toluene. In addition, we used a pulsed-ODMR for enhanced detection capability. N@C$_{60}$ is a paramagnetic molecule [143] where the $S = 3/2$ electron spin is located on the nitrogen atom in the center of the carbon cage. The nitrogen atom is trapped only by the electrostatic potential

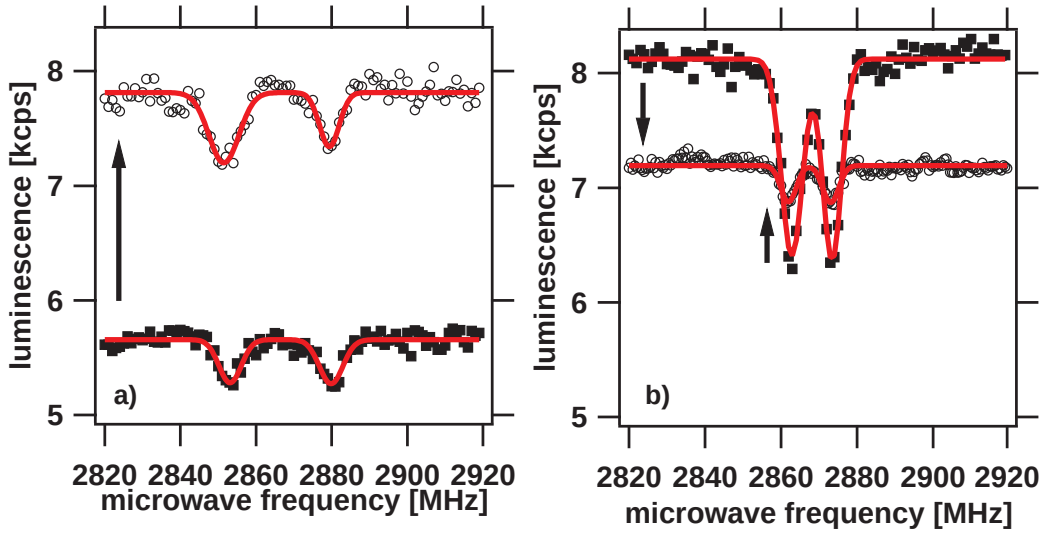

Figure 4.8: ODMR spectrum of two centers before (filled squares) and after (empty circles) addition of 15μl of TEMPOL dissolved in deionized water ($c = 0.1$ g/l). a) Considering the homogeneous increase of background luminescence of ~ 2 kcps, no significant change in ODMR contrast is observed. b) Strong quenching of the ODMR contrast (from 21 to 4 %). Note that, despite of the higher background, the overall luminescence of center b) is reduced.

and does not form any bindings to other atoms (see figure 4.9). The total spin results from 3 unbound electrons residing in the atomic 2p orbitals. Owing to the high symmetry of the molecule, the system does not exhibit any orbital angular momentum and only a small zero-field splitting which can usually be neglected. The hyperfine interaction to the nitrogen nucleus is about 15.7 MHz [143]. The electron spin that resides on the nitrogen atom is very well isolated from its environment, since it overlaps only slightly with its carbon cage. This results in a phase relaxation time of 50 μs at room temperature [144].
According to equation 4.1, compared to TEMPOL the dipolar interaction strength to other spins is increased due to the spin of 3/2 by a factor of 3. Using fullerenes also brings the advantage that the spin concentration can be tuned without affecting the rest of the experiment by using a mixture of endohedral and empty fullerenes. If the ratio between N@C_{60} and C_{60} (filling factor) is set appropriately it should be possible to observe a controlled coupling to a single endohedral fullerene. The optimal spin concentration was calculated by assuming a homogeneous distribution of N@C_{60} in the C_{60} lattice and setting the required distance between the N@C_{60} molecules so that the mean interaction between N@C_{60} molecules is

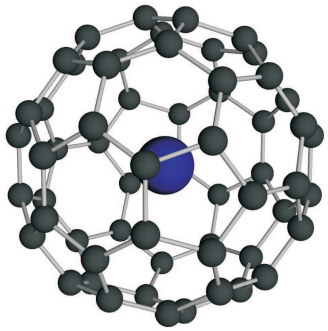

Figure 4.9: Molecular structure of the endehedral fullerene $N@C_{60}$. The nitrogen atom trapped within the fullerene does not form any covalent bonds with the carbon cage, resulting in a half filled 2p shell exhibiting an electron spin $S = 3/2$ according to Hund's rule.

smaller than the smallest $N@C_{60}$ -NV^- interaction observable [93].
From atomic force microscopy it is known that at room temperature C_{60} molecules are mobile on most surfaces. On the other hand, since the attractive interaction between fullerenes is very high due to π-π interactions, many C_{60} molecules will regroup in larger clusters which are immobilized. Clustering of fullerenes does not only occur on surfaces, but also in solution, if the concentration is too high [150, 151]. This is why a thin and more or less homogeneous layer of fullerenes is difficult to achieve at room temperature without chemical bindings to the surface, and the amount of fullerenes as well as the concentration in solution is very critical. From the threshold in CS_2 (60 mg/l, solubility 12 g/l [150]) and the solubility of fullerenes in toluene (2.8 g/l) this threshold can roughly be estimated to be at about 12 mg/l. It has to be noted that upon vaporization of the toluene the concentration of fullerenes temporarily increases above the value prepared.

Figure 4.10 shows a set of confocal microscopy images of a nanodiamond sample covered with increasing volume and concentration of fullerenes dissolved in toluene. Aside from a more or less homogeneous luminescence increase at low concentrations (0.1 to 1 mg/l) a sudden appearance of brightly luminescent fullerene clusters ($< 1\mu$m) can be observed in the case of a concentration higher than the clustering threshold in the solvent. The luminescence of the clusters exceeds the luminescence of a single NV center by a factor of 10 to 100. In addition, this luminescence is unstable and shows a fluctuating behavior resulting from (reversible) blinking and also (irreversible) bleaching of the fullerenes, making it impossible to

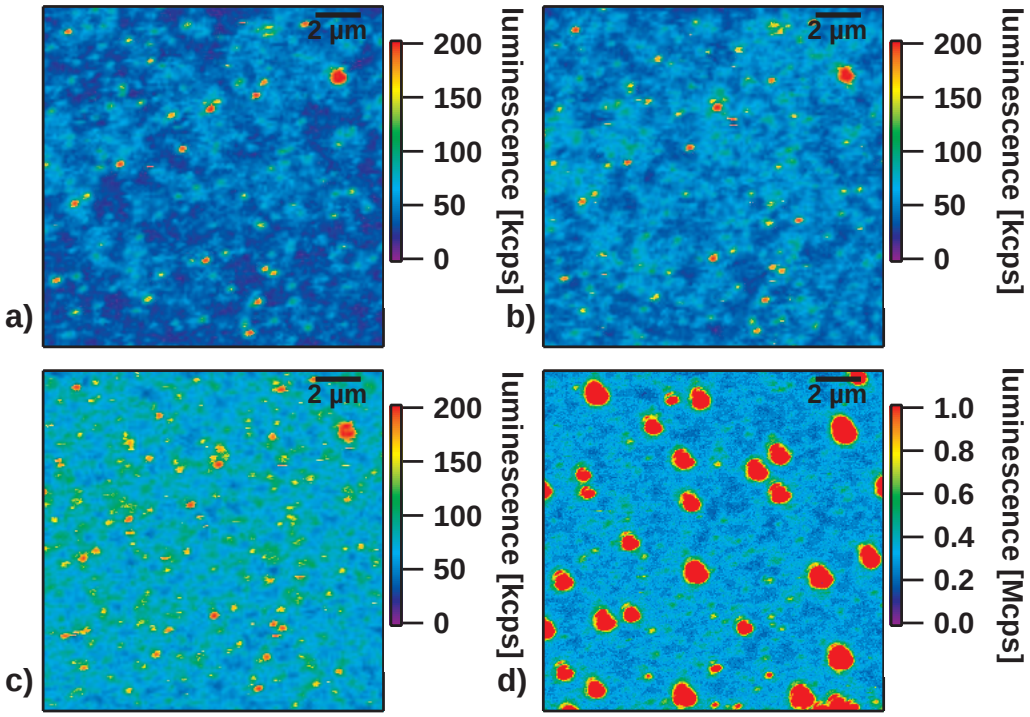

Figure 4.10: 15×15 μm^2 confocal microscopy images of a nanodiamond sample covered with C_{60} fullerenes. Laser power: 40 μW. a) without C_{60} , b) after addition of 45 μl of C_{60} in toluene ($c = 0.1$ mg/l); c) after further addition of 45 μl ($c = 1$ mg/l); d) after further addition of 15 μl ($c = 10$ mg/l). A different color scale was applied in (d).

observe ODMR. From our observations it can be concluded that a concentration of 1 mg/l should not be exceeded.
The observation of photobleaching raises questions about the optical stability of N@C_{60} in a laser field of high power density. Photoinduced de-trapping of N@C_{60} was already reported using pulsed UV laser excitation [152]. For green light the absorption cross section is much smaller. In order to test photostability, we performed an in-situ measurement of the cw epr signal, which is proportional to the spin density, using concentrated N@C_{60} solution in a W-Band spectrometer (Bruker E680) and a focussed high power cw laser (see figure 4.11). A complete decay of the spin signal in N@C_{60} within a few 10 minutes was observed. The power density in the decay experiment was comparable to what is expected in our confocal microscope. Still, the situation in our test experiment may vary somewhat from the conditions in a confocal measurement. We observed that after 30

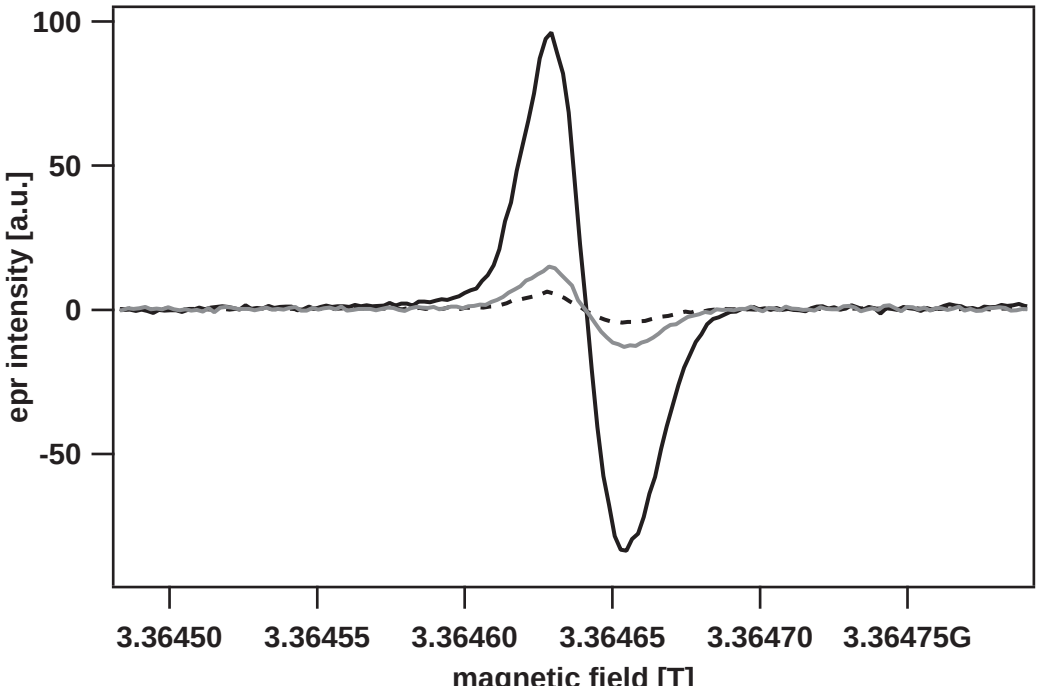

Figure 4.11: Decay of the epr signal of $N@C_{60}$ caused by high power laser irradiation. Only the center hyperfine line is displayed. solid line: untreated $N@C_{60}$; gray line: after 5 minutes irradiation at 532 nm (power density $\sim$ 7 MW/m^2); dashed line: after 5 minutes irradiation at 532 nm (power density $\sim$ 3.5 MW/m^2)

minutes, the heat of the laser lead to complete evaporation of the solvent. The resulting powder is expected to have a much larger absorption cross section for green light than single molecules, which is frequently observed in C_{60} films and explained by a reduced symmetry of C_{60} in a crystal [153]. This is why we cannot tell for sure what is the timescale for the photoinduced decay of isolated $N@C_{60}$ molecules. A second, more encouraging, control experiment using a green pulsed excitation source (0.3 J/pulse, 10 Hz) for 8 hours resulted only in a very minimal decay (< 5 %) of the epr signal.

For coupling experiments of $N@C_{60}$ and NV^- centers, initially a presumably optimal filling factor of 2 % was used, but in later experiments we used a higher filling factor (12 %). The experiment has been conducted on typically 10 to 15 centers multiple times, some by K. Hübener and J. Kniepert [93, 154] and some by the author. A complete list including experimental improvements is given in table 4.1. In the last experiment, a considerably higher resolution ($\sim$ 1 MHz) was

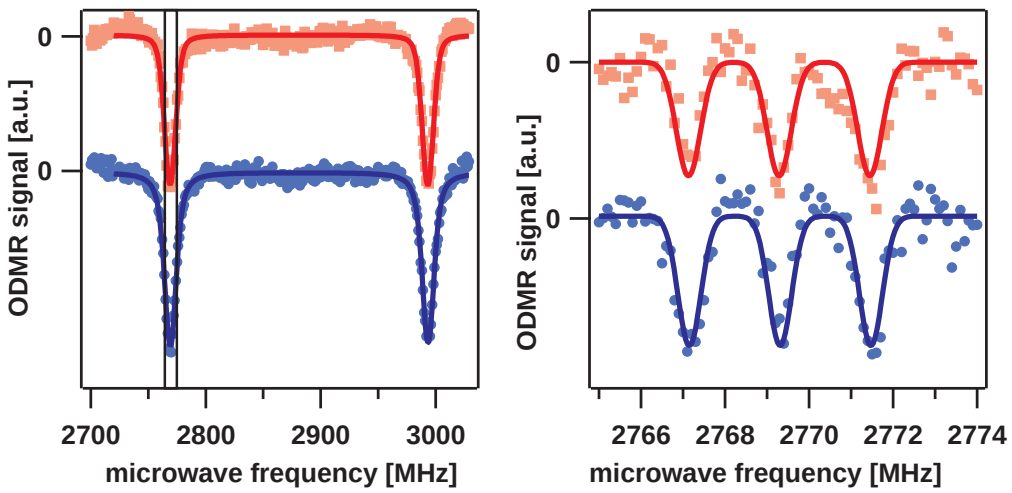

Figure 4.12: Continuous wave ODMR spectra of an NV$^-$ center before (upper traces) and after (lower traces) addition of 15 μl of N@C$_{60}$ dissolved in toluene ($c = 1$ mg/l, $f = 6$ %.). a) Overview spectrum. Laser power: ~ 50 μW, microwave power: ~ 1 W. b) Related high resolution spectrum of the low frequency peak, measured at attenuated power (laser: 10 dB, microwave: 20 dB attenuation).

achieved using low optical and microwave excitation (see 2.5.2). The ODMR signal of most centers was still observable after addition of the N@C$_{60}$ / C$_{60}$:toluene solution. Yet, in none of the experiments any significant change of the ODMR spectrum has been observed (see figure 4.12). This was also the case for the last experiment, where the resolution was improved by a factor of ten with respect to the previous experiments. On the other hand, in the last experiment only a small number of centers was investigated, caused by the strongly increased acquisition time at low excitation power (cf. chapter 2.5.2).

Table 4.1: List of coupling experiments on N@C$_{60}$ and NV$^-$ centers in nanodiamonds

No. of centers	concentration c	filling factor f	average resolution
17	1 mg/l	12	10 MHz
10	1 mg/l	2	10 MHz
14	10 mg/l	2	10 MHz
5	1 mg/l	12	1 MHz

4.2.3 Double electron-electron resonance experiments on coupled NV centers

Pulsed experiments provide a much better resolution than continuous wave spectra since they are not limited by inhomogeneous broadening, but by the true coherence time T_2. Furthermore, in the case of ODMR pulsed measurements avoid the problem of optical broadening if the laser is only active during the polarization and luminescence detection and not during the actual spin experiment. Double resonance experiments provide a very powerful tool in the observation of coupled spins of known g factor, since it is possible to excite very selectively the spin system in question only and thus identify the coupled system very accurately. For example, distinguishing nuclear and electron spins becomes very easy while this would need multiple measurements at different external fields if the coupling was observed by echo modulations (ESEEM) only. If the spin can be identified by its spectroscopic characteristics, it is preferable to use either a spin system with $S > 1/2$ and a nonzero zero-field splitting or a characteristic hyperfine structure in order to distinguish it from ordinary electron spins, dangling bonds or radicals. $N@C_{60}$ with its hyperfine triplet split by $A = 15.7$ MHz provides this feature.
The experiment was conducted together with G. Balasubramanian and F. Jelezko at Universität Stuttgart. For the experiment a low energy ion implanted single crystaline diamond (type IIa) [103] was used. Similar to section 4.2.2, a $N@C_{60}$ /C_{60} :toluene solution ($f = 17$ %, $c = 1$ mg/l) was spin-coated onto the acid cleaned [155] diamond after ultrasonic bath treatment for 25 minutes. The coherent control and NV^- spin detection was in analogy to our setup described in section 2.4.2 and 2.4.4. The pulse timing used is displayed in figure 4.13. The external magnetic field was set to 65 mT parallel to the NV^- symmetry axis, resulting in a $|0\rangle \rightarrow |-1\rangle$ transition frequency of 1040 MHz and a $|0\rangle \rightarrow |1\rangle$ transition frequency of about 4700 MHz. For the ODMR experiment, the $|0\rangle \rightarrow |-1\rangle$ transition was chosen for convenience. The particular strength and orientation of the magnetic field has the advantage that close to the so-called level anticrossing (LAC) regime (51.4 mT) the polarization of the NV^- spin can transfer to the $N@C_{60}$ spin by spin flip-flop processes [104], resulting in effective spin polarization of the $N@C_{60}$ molecule. This strongly increases the contrast of the ODMR experiment. For a $g \approx 2$ type spin like $N@C_{60}$ a resonance frequency of $2880 - 1040 = 1840$ MHz is expected. From Rabi nutations (see fig. 4.14a) a π pulse length of 18 ns was determined for the NV^- center spin. The Hahn echo decay time (see fig. 4.14b) of the center was very short ($\sim 1.4\mu$s) compared to what is typically expected for this type of diamond (400 μs [102]). This gives some evidence of the shallow nature of the defect investigated. On the other hand, a short T_2 is not very helpful for the experiment since it requires 'hard' (high power) microwave pulses due to the small time window given by phase relaxation. The

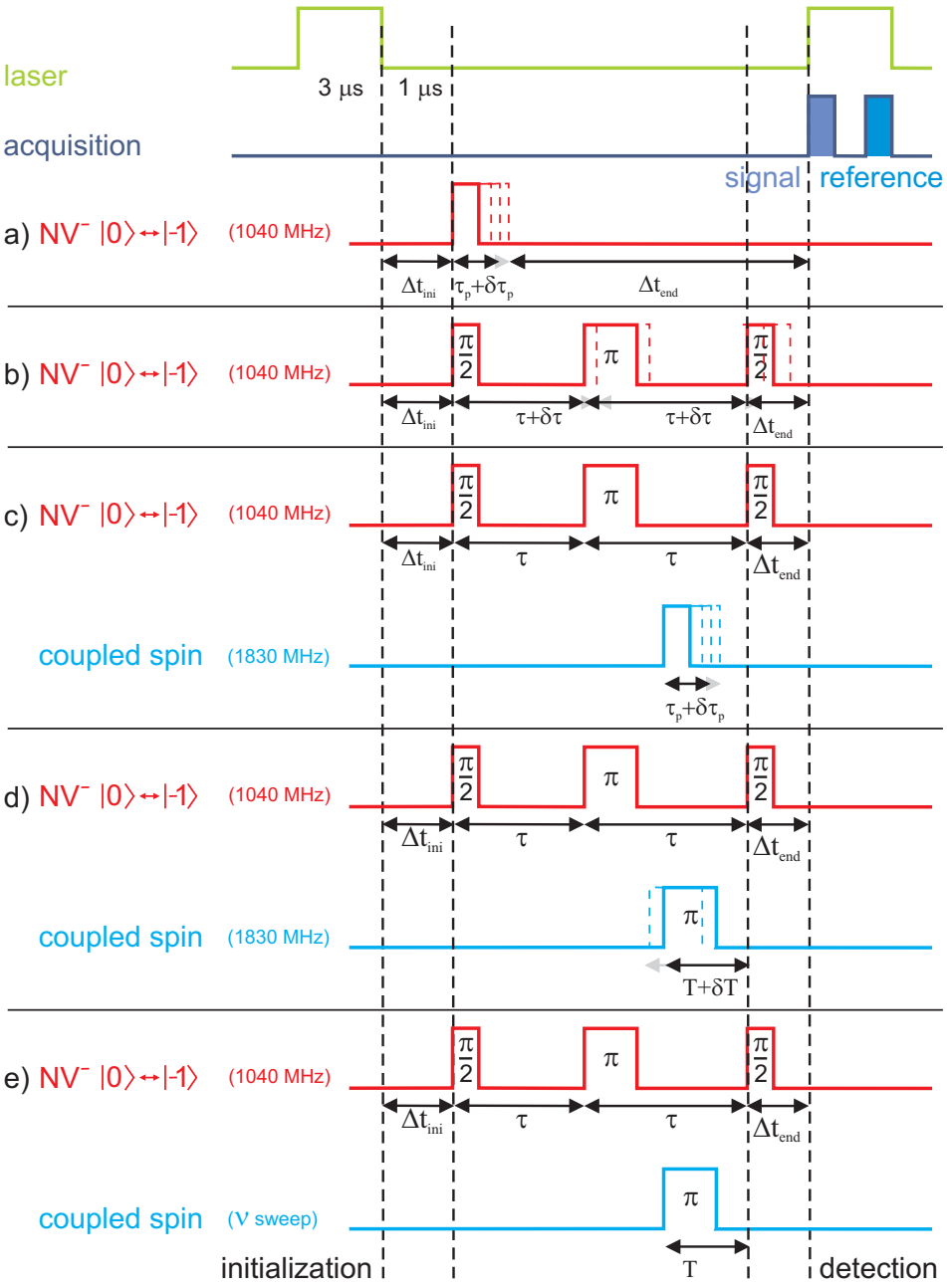

Figure 4.13: Pulse patterns of the doube electron electron resonance (DEER) experiment. a) Rabi nutation of the NV⁻ center, $\Delta t_{\mathrm{ini}} = 1\,\mu\mathrm{s}, \Delta t_{\mathrm{end}} = 50\,\mathrm{ns}$; b) Echo decay of the NV⁻ center; c) Rabi nutation of the coupled spin measured by the NV⁻ center, $\tau = 3\,\mu\mathrm{s}$; d) Echo decay of the coupled spin measured by the NV⁻ center; e) spectrum of the coupled spin measured by a frequency sweep with $\mathrm{T} = 2\,\mu\mathrm{s}$.

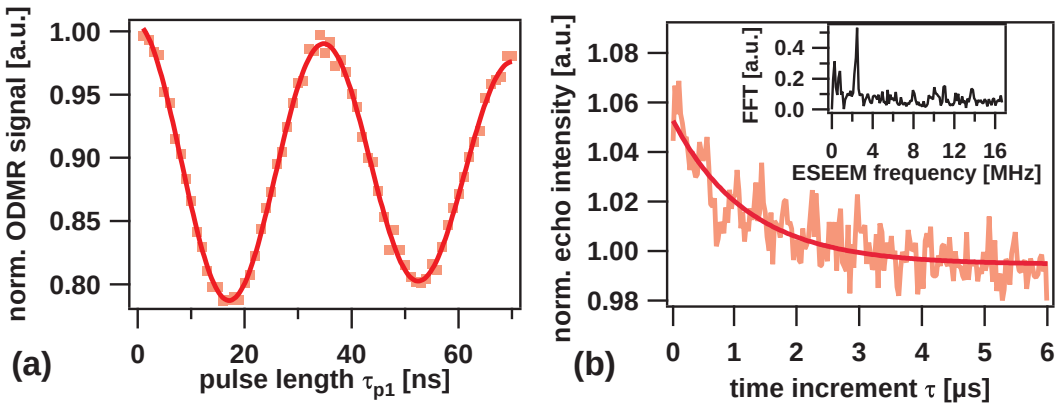

Figure 4.14: (a) Spin nutation of the $|-1\rangle \leftrightarrow |0\rangle$ transition of the NV$^-$ center used for DEER (see fig. 4.13a). (b) Spin echo decay of the same transition (see fig. 4.13b). The inset shows the FFT revealing ESEEM at 2.2 MHz induced by hyperfine coupling to the ^{14}N nucleus of the NV$^-$ center.

excitation width of such hard pulses will affect the resolution of the experiment. Now, between the refocussing pulse and the detection, a pulse with consecutive length on the 'guessed' second transition at 1840 MHz was applied. The resulting effect on the NV$^-$ center spin clearly shows a coherent behavior (see figure 4.15a). Thus, we can asume that we are able to observe the coherent nutations of a coupled electron spin (or spin ensemble) via its effect on the phase vector of the NV$^-$ center spin. Still, we are not able to tell if the spin in question is N@C$_{60}$ or another electron spin.
The echo decay of the second spin was measured in an analogous way (fig. 4.15b, for pulse timing, see fig. 4.13d). Within the small time window given by the coherence of the NV$^-$ center, no modulation was observed, which tells that the coupling strength must be smaller than 300 kHz.

Finally, to measure the spectrum of the unknown spin system, on the second microwave channel a π pulse sweeping in frequency was applied. A single uniformly broadened line of about 40 ± 7 MHz width was observed (see figure 4.16). This is however expected, as it roughly resembles the spectral resolution given by the excitation width of a 30 ns π pulse. More significantly, if also unfortunately, during this experiment the ODMR contrast suddenly dropped from about 3 % as expected from the echo amplitude to zero. No signal was observed when performing DEER experiments (fig. 4.13c-e), but a control experiment on the NV$^-$ center (fig. 4.13a) revealed the same contrast as before. Thus, we have to conclude that the NV$^-$ center is still present, but either the coupling is inactive, or the spin

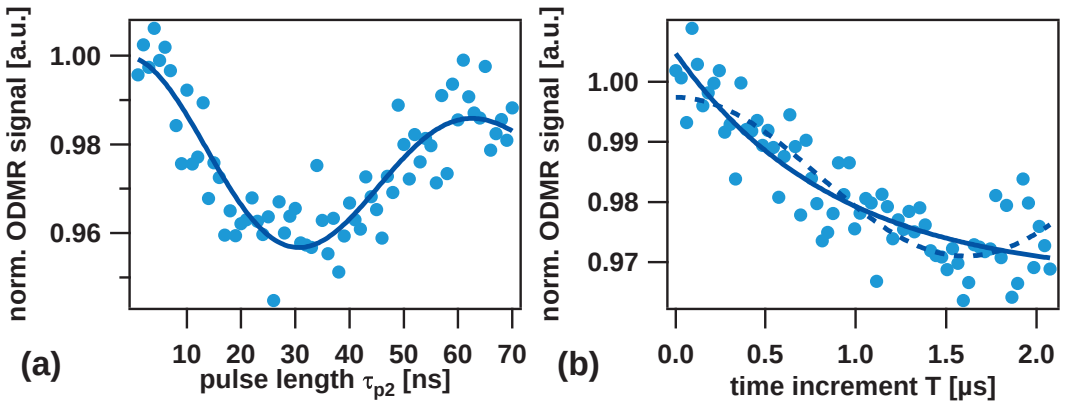

Figure 4.15: (a) Rabi nutation of a spin coupled to an NV$^-$ center observed by DEER (see fig. 4.13c). (b) Spin echo decay of the coupled spin (see fig. 4.13d). From the exponential fit (solid line) and cosine fit (dashed line) a upper bound for decay constant (1.1 MHz) and interaction strength (300 kHz) can be estimated.

(or spin ensemble) the coherent motion of which we were observing was quenched during the experiment.

Discussion

From our data we can conclude that we have observed a coherent coupling to one or multiple electron spins. Yet, we are not able to tell if the spin resides on N@C_{60}. An incomplete list of other candidates include: substitutional nitrogen in diamond, dangling bonds on the surface, holes on the diamond surface induced by water, C_{60}^- (all $S = 1/2$), and photoexcited triplet states, in particular in C_{60}. The suddenness of the loss of the DEER signal is probably the best evidence for a single spin and for N@C_{60} as well, since one would expect a spin ensemble to decay continuously. On the other hand, photobleaching of N@C_{60} is an effect that was already expected from our photostability measurements (compare figure 4.11). Moreover, the absence of ESEEM in figure 4.15d also fits into the picture, since N@C_{60} is a highly isotropic system. Unfortunately, none of these these considerations offer any solid proof. For such, as for any functional application, a non-photobleaching system with identical properties to N@C_{60} would be required. Still, probably the most important conclusion from this experiment lies in proving the superiority of DEER compared to the other strategies applied in observation of coupled electron spin systems.

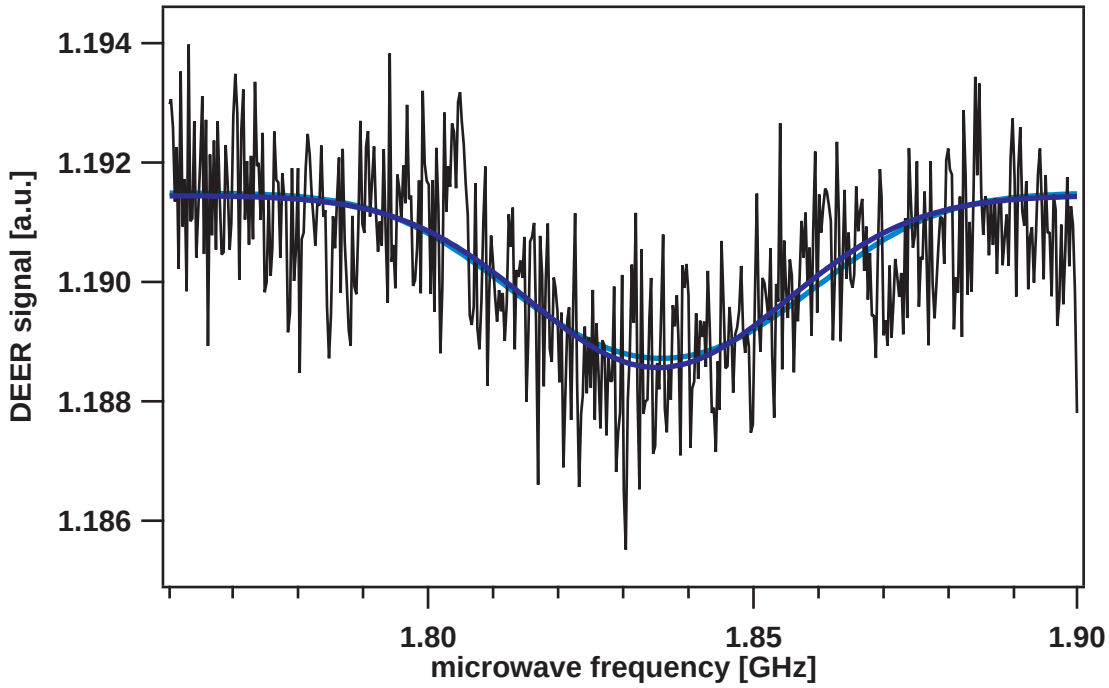

Figure 4.16: Spectrum of a spin coupled to an NV$^-$ center measured by DEER (compare fig. 4.13e). The blue line represents a single gaussian fit (FWHM 47 MHz) and the cyan line represents a fit by three gaussian lines at fixed distance of 15.7 MHz (FWHM 38 MHz), which corresponds to size and shape of the N@C_{60} hyperfine structure. From the π pulse length a resolution of 40 MHz is expected.

4.2.4 Chemical modification of C_{60} fullerenes for increased photo- and thermostability

Due to its large coherence, spin quantum number (3/2) and characteristic hyperfine splitting [143] $N@C_{60}$ seems to be an excellent candidate for coupling to nitrogen vacancy centers. In addition, the possibility to create a mixture of C_{60} and $N@C_{60}$, which are chemically almost completely identical molecules [156, 157] that can be distinguished only by their spin, allows one to tune the spin concentration without additional concerns of different chemistry or affinity to the surface. On the other hand, $N@C_{60}$ provides not only advantages but also disadvantages. One disadvantage is the nonzero C_{60} luminescence that was observed previously (see fig. 4.10). The reason for this luminescence is quite complicated. For single molecules, the quantum efficiency and absorption quotient for green light is very low since direct optical HOMO-LUMO excitation is forbidden by symmetry [158]. Yet, in the solid state the formation of charge transfer excitons induced by optical excitation using green light is possible. In addition, stress can reduce the symmetry of fullerenes, resulting in breaking of the selection rules and leading to enhanced phosphorescence [159].
Another disadvantage is that fullerenes have a very strong intermolecular interaction and high mobility at room temperature which allows them to form large clusters with increased luminescence [93, 150, 151]. This is a problem, since a thin homogeneous coverage of the surface (in ideal case a monolayer) is a desired key to a successful experiment. Even chemical bonding to the surface can not solve this problem, since it still may lead to clusters of fullerenes irremovably stacked atop the chemically bound monolayer[154].
Another problem is that ODMR requires high irradiation densities. It could be shown [152] that due to photoexcitation of C_{60}, the nitrogen radical can attack a π bond of the C_{60} cage and escape the interior of the fullerene, resulting in vanishing of the paramagnetic properties. The same process can be induced not only by light, but it is also thermally activated at moderate temperatures ($> 200°C$) [160].

Interestingly, all these difficulties have a common origin, which is the wealth of double bonds in the fullerene that leads to an extended aromatic system. Breaking only a few of these bonds so that the conjugated system is divided into smaller subsystems will result in an efficient inhibition of the major escape process, while at the same time shifting the absorption wavelength to lower values. Furthermore, if breaking of the bonds is realized by large chemical groups binding to the fullerene, these groups can act as a spacer that reduces mobility and clustering at the same time. Finally, if the side groups attached to the C_{60} cage are carefully selected and if use is made of regio-selective chemistry of fullerenes[161], such functionalization

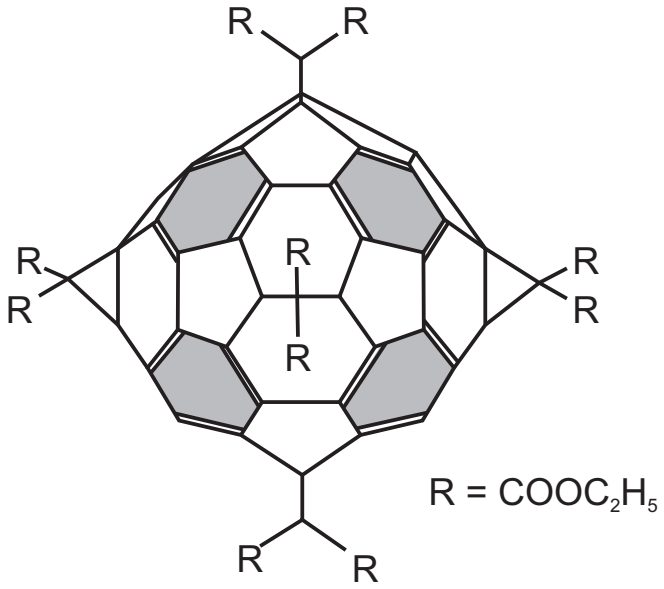

Figure 4.17: Chemical structure of $C_{66}R_{12}$ (atoms on the backside are not shown). The grey shaded areas mark the residual aromatic rings, which are isolated from each other.

can be used for grafting (i.e. covalent bonding) of N@C_{60} to the diamond surface.

The chemistry of fullerenes is well understood and there are many ways to chemically synthesize adducts of fullerenes. Due to the chemical and temperature restrictions when using N@C_{60} we have decided to use a regioselective Bingel reaction [162]. This reaction is known to preserve the N@C_{60} spin [163] and to spontaneously proceed at room temperature. A maximum of 6 side groups can bind to C_{60} by forming a cyclopropene ring from a former double bond. This results in the fullerene hexakisadduct $C_{66}R_{12}$ ([164, 165], see fig. 4.17). For our purpose, we chose R = C_2H_5 (ethyl) for being a small non-aromatic side group. The reaction scheme is given in figure 4.18. The reaction is based on a reversible Diels-Alder addition of 9,10-dimethylanthracene (DMA) that acts as a template by chemically activating the sites where the final modification is desired to take place. After this reaction a nucleophilic addition of bromomalonate to a double bond of the fullerene results in a cyclopropane ring. The regioselectivity of the reaction is not perfect. Aside from the highly symmetric hexakis adduct isomers of lesser adducts will form, which show a spacial configuration that does not allow for further reaction to the end product. These still show absorption in the green range and have to be removed from the hexakis adduct by a flash column and/or

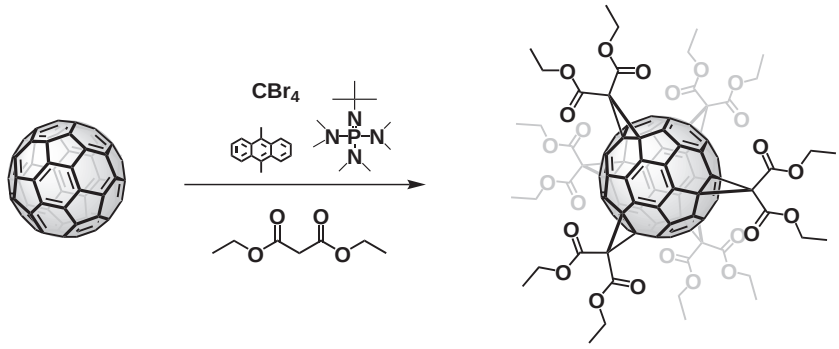

Figure 4.18: Synthesis of the fullerene hexakisadduct.

Table 4.2: List of chemicals used for two syntheses of $C_{66}(COOC_2H_5)_{12}$

	C_{60}	DMA	phosphacene	CBr_4	diethylmalonate	toluene
molar ratio N	1	10	15	10	15	-
mass m_1 (mg)	200	572	975	920	667 (632 μl)	150 ml
mass m_2 (mg)	0.5	1.43	2.44	3.45	1.67 (1.59 μl)	10 ml

normal phase HPLC.

Synthesis of $C_{66}(COOC_2H_5)_{12}$

The complete chemical reaction operates under nitrogen atmosphere at room temperature. The reaction vessel has to be shielded from light in order to avoid irreversible addition of DMA to C_{60} . First, 200 mg of N@C_{60} /C_{60} was dissolved in 100 ml of water-free toluene. Then, 572 mg of DMA (ACROS) in 50 ml toluene was added and stirred for two hours to ensure complete addition of the template to the fullerenes. After that, 920 mg of CBr_4 (Aldrich) and 667 mg (632 μl) diethylmalonate (ACROS) were added to form bromomalonate *in situ*. Finally, 975 mg of phosphacene was slowly added using a syringe, starting the Bingel reaction. The reaction was monitored during two days while continuously stirring. The formation of the products was observed using thin film chromatography.

The desired product was separated from other products and purified further in two steps, first by flash chromatography using an ethylacetate/toluene mixture with an increasing fraction of ethylacetate ranging from 0 to 6 %. As a second step, high performance liquid chromatography (HPLC) was applied using a Nucle-

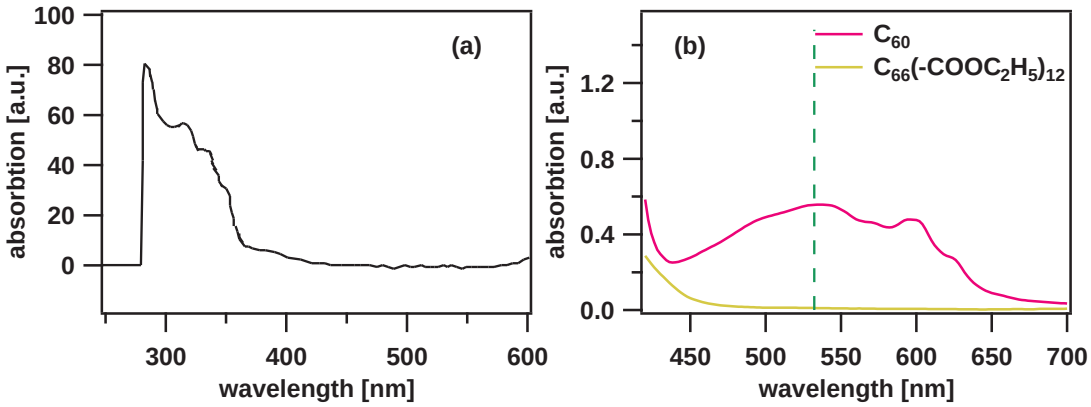

Figure 4.19: (a) Absorption spectrum of $C_{66}(COOC_2H_5)_{12}$. (b) Absorption spectra of 1 mg/l C_{60} and $C_{66}(COOC_2H_5)_{12}$. The dashed green line marks the ODMR excitation wavelength (532 nm).

osil (50-5) analytic normal phase column and toluene as eluent. The peak of the hexakisadduct was observed at 20 minutes retention time. After purification, the hexakisadduct was analyzed by proton-, carbon- and heteronuclear multiple bond coherence (HMBC) nuclear magnetic resonance (see appendix). The product was a bright yellow powder and the reaction yield was 23.3 % . No absorption could be observed at 532 nm (see fig. 4.19.)

In addition, since it was not known whether all or or just a small ratio of $N@C_{60}$ is preserved the total spin concentration of the mixture had to be checked by extracting small portions of 50 microliters from the reaction and measuring the total spin concentration using analytic HPLC and continuous wave epr. The two critical chemical steps are the Diels-Alder addition of DMA and the nucleophilic attack of the base. Both processes were monitored individually (see fig. 4.20). From the result it was evident that $N@C_{60}$ is preserved at least by more than 90 percent during these reaction stages. The slight reduction of the signal after addition of DMA might be due to chemical losses, but it could also be attributed to baseline drift or changes in relaxation behavior of the spin after addition of DMA, which will also influence the epr signal intensity. Using both high power cw laser irradiation (6 Watts, 514 nm) for 1 hour, and pulsed laser exitation (532 nm, 0.3 J/pulse, 10 Hz) for 8 hours, no decay of the epr signal was observed.

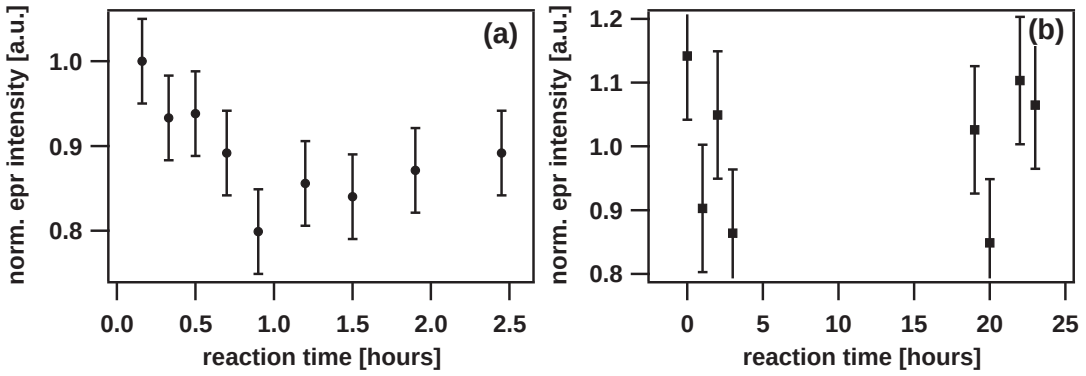

Figure 4.20: Monitoring of the spin density of endohedral fullerenes during the critical chemical reaction stages. (a) N@C_{60} + DMA, (b) N@C_{60} + Phosphacene. Note that the absolute density between figures (a) and (b) cannot be compared.

4.3 Summary and discussion

We have observed that the spin of an NV$^-$ center in some of the nanodiamonds is able to respond to the environment by means of decoherence and quenched luminescence, but removal of the amorphous carbon layer surrounding the particles is required. In particular, water on the surface plays an important role in decoherence. This decoherence effect was used to determine qualitatively, whether a 'deep' or 'shallow' center is present. A quantitative analysis of the center depth will require electronically pure crystals with better intrinsic coherence. The nature of the water-induced decoherence process has to be investigated in further detail. Furthermore, the spin label TEMPOL has a strong quenching effect on the luminescence and ODMR contrast of some (about half) of the centers. This can be explained by inhibition of the spin polarizing mechanism (as for example induced by spin mixing), or by enhanced non-radiative excitation decay rates.
Coupling of single paramagnetic molecules to an NV$^-$ center has proven more difficult. On the one hand, CW spectroscopy does not provide the resolution needed to resolve a coupling by magnetic dipolar interaction. One the other hand, the optical stability of N@C_{60} is not sufficient for the radiation densities needed for excitation of the NV$^-$ center. Still, we were able to observe a coupling to another g=2 electron spin by DEER techniques. Due to low coherence of the center investigated and due to spontaneous (and abrupt) quenching of the coupled spin during the experiment, it was not possible to identify the spin unambiguously. In addition, we cannot tell for sure if the spin was a single one, or an ensemble of spins, since the epr signal was quenched during the measurement. Still, one can

surmise that this was probably the case, because seemingly the signal died all-at-once, which is unlikely for the ensemble case. In addition, the optically induced quenching of the spin seems to hint to $N@C_{60}$, again, but this is mere speculation. To overcome disadvantages of $N@C_{60}$ in a coupling experiment, in particular background luminescence, photoinduced decay, thermally induced decay and clustering, we have synthesized a fullerene hexakisadduct that has similar spin properties to $N@C_{60}$, but a strongly reduced aromatic system. Spin losses during the chemical reaction and purification seem to be negligibly small. For future coupling experiments, employing DEER and using the fullerene hexakisadduct synthesized here seems very promising.

Chapter 5

Realization of the refined Deutsch-Jozsa (rDJ) algorithm using the NV^- center spin system

As discussed in earlier sections, the NV^- center in diamond is an exceptional qubit candidate, since the coherence of the electron spin is preserved for very long times at room temperature. Despite the many breakthroughs in quantum control and readout, and despite the demonstration of entanglement to nuclear spins in particular, no actual quantum algorithm has been performed, yet. This is somewhat surprising, since a combination of an electron spin with multiple nuclear spins has been proposed as an elementary building block for larger quantum architectures. On the other hand, it is even more interesting that, although the NV^- exhibits a total spin of one, in all experiments only a 2-dimensional subspace of the full Hamiltonian of the center has been used. Exploiting the full richness of the spin Hamiltonian, one can implement rudimentary quantum operations even on an isolated NV^- center.

In this chapter, we present a room-temperature implementation of a quantum algorithm, i.e., the refined Deutsch-Jozsa (rDJ) algorithm [166], using a single NV^- center. The rDJ algorithm is the simplified version of the original Deutsch-Jozsa algorithm [33], one of the most frequently mentioned quantum algorithms. As the first proposed quantum algorithm, the Deutsch-Jozsa algorithm has been employed in different systems to demonstrate the exponential speedup in distinguishing constant from balanced functions with respect to the corresponding classical algorithm. For example, it has been carried out experimentally in nuclear magnetic resonance systems [16], in quantum dot systems [167, 168], by linear optics [169], and by trapped ions [170]. Compared to the original Deutsch-Jozsa algorithm, the refined version [166] removes the qubit for the evaluation of the function, which anyhow remains unchanged during the algorithm implementation.

As a result, it can reduce the required qubit resources but still maintain the superiority due to quantum power over the corresponding classical algorithm.

5.1 Description of the refined Deutsch-Jozsa algorithm

5.1.1 The two qubit Deutsch-Jozsa algorithm

The "Problem of Deutsch" [32] was one of the first 2-qubit quantum algorithms proposed in 1985. Later the problem was generalized to a function which takes an arbitrary number of bits for input by David Deutsch and Richard Jozsa [33]. Although being of little practical use this algorithm is one of the first examples of a quantum algorithm that is exponentially faster than any possible deterministic classical algorithm. Its purpose is to determine if a binary function $f : \{0,1\} \rightarrow \{0,1\}$ is constant ($f(0) = f(1)$) or balanced ($f(0) \neq f(1)$). An often used picture of what this could achieve is a test to verify if a coin is fake (has two equal sides) or fair (two distinguishable sides). To underline the advantage of the quantum algorithm it is usually considered that any evaluation of that function (analogous to throwing the coin) is "expensive", e.g. time consuming. Since a quantum algorithm allows the evaluation of a superposition of states (quantum parallelism) only one execution of the function is necessary to get an answer to the particular question. The original quantum circuit of the Deutsch-Jozsa algorithm is shown in Fig. 5.1. Its key elements are *(a)* preparation of superposition states $\frac{1}{2}(|0\rangle + |1\rangle)$ via Hadamard gates

$$\mathbf{H} = \frac{1}{\sqrt{2}} \begin{pmatrix} 1 & 1 \\ 1 & -1 \end{pmatrix} \tag{5.1}$$

applied to an initial pure state, *(b)* evaluation of the function in question using a f-controlled-NOT gate, *(c)* projection of the result back into eigenstates and *(d)* measurement of one qubit.
Using the density matrix formalism [89] and the eigenbase $\{|00\rangle, |01\rangle, |10\rangle, |11\rangle\}$, the initial state is

$$\rho_{\text{ini}} = \begin{pmatrix} 0 & 0 & 0 & 0 \\ 0 & 1 & 0 & 0 \\ 0 & 0 & 0 & 0 \\ 0 & 0 & 0 & 0 \end{pmatrix} \quad . \tag{5.2}$$

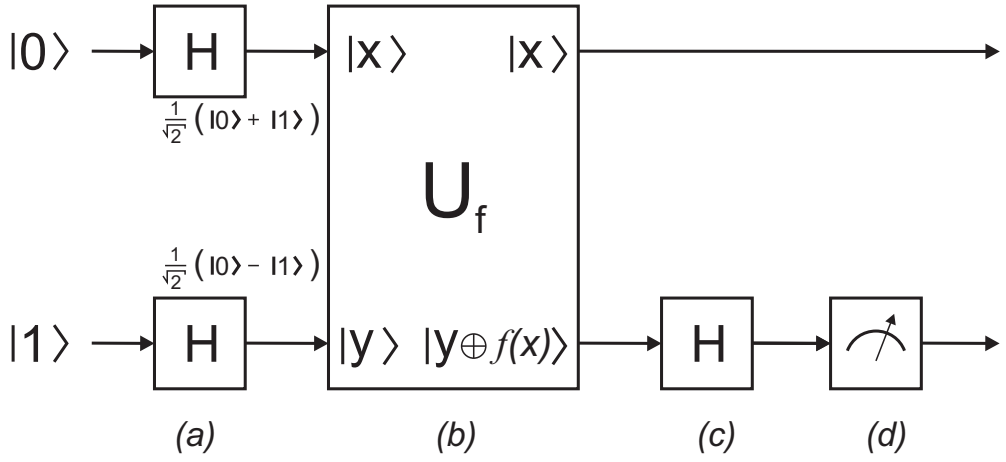

Figure 5.1: Quantum circuit of the Deutsch-Jozsa algorithm using only one input and one target bit.

In consequence, after the preparation of superposition the new state becomes

$$\rho_{\mathrm{a}} = (\mathbf{H} \otimes \mathbf{H})\, \rho_{\mathrm{ini}}\, (\mathbf{H} \otimes \mathbf{H})^{\dagger} = \frac{1}{4} \begin{pmatrix} 1 & -1 & 1 & -1 \\ -1 & 1 & -1 & 1 \\ 1 & -1 & 1 & -1 \\ -1 & 1 & -1 & 1 \end{pmatrix} \quad . \tag{5.3}$$

Four possible functions are available, two constant ($f(0) = 0$ or 1) and two balanced functions, namely the identity ($f(0) = 0 \mathrm{and} f(1) = 1$) and the NOT-function ($f(1) = 0$ and $f(0) = 1$). The operator of the function that results in the output $|\, x\, y \oplus f(x)\rangle$ can be written in a general form

$$\mathbf{F} = \begin{pmatrix} \overline{f(0)} & f(0) & 0 & 0 \\ f(0) & \overline{f(0)} & 0 & 0 \\ 0 & 0 & \overline{f(1)} & f(1) \\ 0 & 0 & f(1) & \overline{f(1)} \end{pmatrix} \quad . \tag{5.4}$$

Transformation of ρ_{a} (equation 5.3) using this matrix yields

$$\rho_{\mathrm{b}} = \mathbf{F} \rho_{\mathrm{a}} \mathbf{F}^{\dagger} =$$

$$\frac{1}{4}\begin{pmatrix} \left(\overline{f(0)}-f(0)\right)^2 & -\left(\overline{f(0)}-f(0)\right)^2 & \left(\overline{f(0)}-f(0)\right)\left(\overline{f(1)}-f(1)\right) & -\left(\overline{f(0)}-f(0)\right)\left(\overline{f(1)}-f(1)\right) \\ -\left(\overline{f(0)}-f(0)\right)^2 & \left(\overline{f(0)}-f(0)\right)^2 & -\left(\overline{f(0)}-f(0)\right)\left(\overline{f(1)}-f(1)\right) & \left(\overline{f(0)}-f(0)\right)\left(\overline{f(1)}-f(1)\right) \\ \left(\overline{f(0)}-f(0)\right)\left(\overline{f(1)}-f(1)\right) & -\left(\overline{f(0)}-f(0)\right)\left(\overline{f(1)}-f(1)\right) & \left(\overline{f(1)}-f(1)\right)^2 & -\left(\overline{f(1)}-f(1)\right)^2 \\ -\left(\overline{f(0)}-f(0)\right)\left(\overline{f(1)}-f(1)\right) & \left(\overline{f(0)}-f(0)\right)\left(\overline{f(1)}-f(1)\right) & -\left(\overline{f(1)}-f(1)\right)^2 & \left(\overline{f(1)}-f(1)\right)^2 \end{pmatrix}$$

$$= \frac{1}{4}\begin{pmatrix} 1 & -1 & (-1)^{f(0)\oplus f(1)} & -(-1)^{f(0)\oplus f(1)} \\ -1 & 1 & -(-1)^{f(0)\oplus f(1)} & (-1)^{f(0)\oplus f(1)} \\ (-1)^{f(0)\oplus f(1)} & -(-1)^{f(0)\oplus f(1)} & 1 & -1 \\ -(-1)^{f(0)\oplus f(1)} & (-1)^{f(0)\oplus f(1)} & -1 & 1 \end{pmatrix} \tag{5.5}$$

The symbol $\oplus$ represents the addition modulo 2 (XOR gate), which is 0 if both inputs are equal and 1 in all other cases. Since no entanglement is present this matrix can be separated into the two one-qubit states

$$\rho_{\mathrm{b}} = \frac{1}{2}\begin{pmatrix} 1 & -1 \\ -1 & 1 \end{pmatrix} \otimes \frac{1}{2}\begin{pmatrix} 1 & (-1)^{f(0)\oplus f(1)} \\ (-1)^{f(0)\oplus f(1)} & 1 \end{pmatrix} \tag{5.6}$$

Another Hadamard operation on the second qubit projects the off-diagonal elements into eigenstates

$$\rho_{\mathrm{c}} = \frac{1}{2}\begin{pmatrix} 1+(-1)^{f(0)\oplus f(1)} & 0 \\ 0 & 1-(-1)^{f(0)\oplus f(1)} \end{pmatrix} \tag{5.7}$$

From this it can be seen that measurement of the output qubit will result in $|\,0\rangle$ if, and only if $f(0) \oplus f(1) = 0$, which means the function is constant. If the function is balanced the resulting state will be $|\,1\rangle$.

5.1.2 The refined Deutsch-Jozsa algorithm

It was later demonstrated by D. Collins *et al.* [166] that the algorithm can be experimentally tested without the need of a control qubit which usually has the function of preserving unitary (two-way) operation. They proposed a refined Deutsch-Jozsa algorithm (see Fig. 5.2), where the f-controlled-NOT gate can be replaced by multiple single qubit gates. While this is not enough to actually implement the algorithm itself it represents a "test-bed" to validate the correct outcome of the algorithm. The general algorithm needs a one qubit phase rotation. In order to implement such a gate the presence of an auxiliary level is sufficient. Such a level exists in the case of a triplet system where the two possible allowed transitions can be selectively driven. In this case it can be shown that operation on one transition is equivalent to a controlled phase gate (cPhase) on the other transition. By using the $|\,0\rangle$, $|\,-1\rangle$ subsystem as qubit and $|\,1\rangle$ as auxiliary level we define the necessary gates the following way:

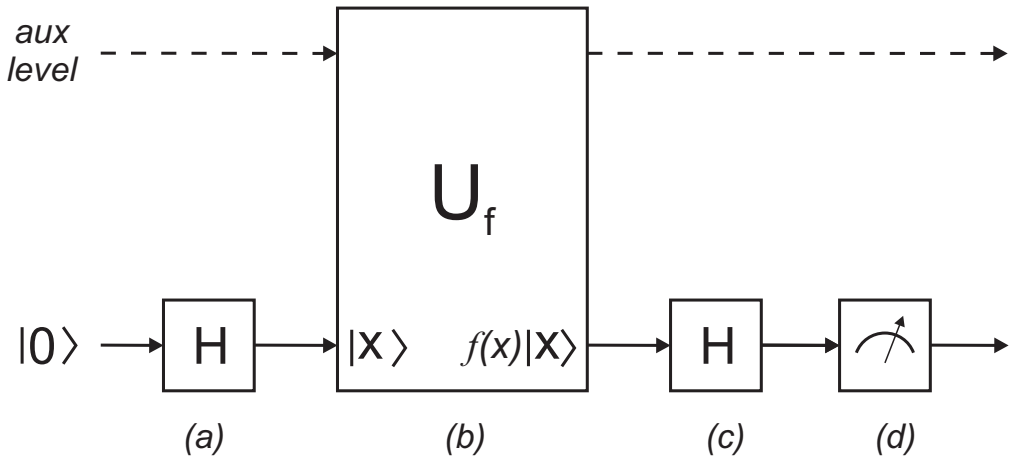

Figure 5.2: Quantum circuit of the refined Deutsch-Jozsa algorithm. The dashed line represents the auxiliary level that is initialized as 0 and used as "phase dump".

The Hadamard gate is replaced by a selective $\frac{\pi}{2}$ pulse ($\sqrt{\mathbf{Y}}$) on the $|0\rangle \rightarrow |-1\rangle$ transition. This is because qubit rotations around the X or Y axis are experimentally easier to implement. The only difference lies in the fact that $\mathbf{H}^2 = \mathbf{E} \neq \mathbf{Y}$. Here, $\mathbf{E}$ is the identity matrix. For simplifying reasons we define the rotational axis as Y which keeps the qubit vector in the real plane. Thus we obtain:

$$\sqrt{\mathbf{Y}} = \left(\begin{array}{c|cc} 1 & 0 & 0 \\ \hline 0 & & \\ 0 & & \exp\left(-i\frac{\pi}{4}\mathbf{S_y}\right) \end{array}\right) = \frac{1}{\sqrt{2}} \begin{pmatrix} \sqrt{2} & 0 & 0 \\ 0 & 1 & -1 \\ 0 & 1 & 1 \end{pmatrix} \tag{5.8}$$

The Pauli Y Gate is successively implemented by the corresponding π pulse:

$$\mathbf{Y} = \left(\begin{array}{c|cc} 1 & 0 & 0 \\ \hline 0 & & \\ 0 & & \exp\left(-i\frac{\pi}{2}\mathbf{S_y}\right) \end{array}\right) = \begin{pmatrix} 1 & 0 & 0 \\ 0 & 0 & -1 \\ 0 & 1 & 0 \end{pmatrix} \tag{5.9}$$

and a complete 2π rotation is given by

$$\mathbf{Y}^2 = \left(\begin{array}{c|cc} 1 & 0 & 0 \\ \hline 0 & & \\ 0 & & \exp\left(-i\pi\mathbf{S_y}\right) \end{array}\right) = \begin{pmatrix} 1 & 0 & 0 \\ 0 & -1 & 0 \\ 0 & 0 & -1 \end{pmatrix} \quad . \tag{5.10}$$

In order to implement an equivalent to a 2-qubit operation, e.g. controlled gates the auxiliary level has to be used. It can be shown that a 2π rotation on the auxiliary transition

$$\mathbf{Z} = \left(\begin{array}{cc|c} & & 0 \\ \exp\left(-i\pi\mathbf{S_y}\right) & & 0 \\ \hline 0 & 0 & 1 \end{array}\right) = \begin{pmatrix} -1 & 0 & 0 \\ 0 & -1 & 0 \\ 0 & 0 & 1 \end{pmatrix} \tag{5.11}$$

is equivalent to a phase change by $-\pi$ in the qubit subspace (also called Pauli Z gate), which is experimentally difficult to apply using microwave pulses resonant on the qubit transition only. Thus all elements used in the refined Deutsch-Jozsa algorithm can be experimentally implemented by multi-frequency epr on two transitions. The four possible functions are given the following way:

$f(0)$	$f(1)$	Operator	Gates
0	0	$\mathbf{Z}$	$\mathbf{Z}$
0	1	$\mathbf{E}$	none
1	0	$-\mathbf{E}$	$\mathbf{Y}^2$
1	1	$-\mathbf{Z}$	$\mathbf{Y}^2,\ \mathbf{Z}$

This can be described by a generalized matrix

$$\mathbf{F} = \begin{pmatrix} -(-1)^{f(0)\oplus f((1)} & 0 & 0 \\ 0 & (-1)^{f(0)} & 0 \\ 0 & 0 & -(-1)^{f(1)} \end{pmatrix} \quad . \tag{5.12}$$

The initial state is $|\, m_s = 0\rangle$. Following the quantum circuit diagram shown in Fig. 5.2, we get

$$\rho_{\mathrm{ini}} = \begin{pmatrix} 0 & 0 & 0 \\ 0 & 1 & 0 \\ 0 & 0 & 0 \end{pmatrix} \quad ; \tag{5.13}$$

$$\rho_{\mathrm{a}} = \sqrt{\mathbf{Y}}\rho_{\mathrm{ini}}\sqrt{\mathbf{Y}}^{\dagger} = \frac{1}{2}\begin{pmatrix} 0 & 0 & 0 \\ 0 & 1 & 1 \\ 0 & 1 & 1 \end{pmatrix} \quad ; \tag{5.14}$$

$$\rho_{\mathrm{b}} = \mathbf{F}\rho_{\mathrm{a}}\mathbf{F}^{\dagger} = \frac{1}{2}\begin{pmatrix} 0 & 0 & 0 \\ 0 & 1 & (-1)^{f(0)\oplus f(1)} \\ 0 & (-1)^{f(0)\oplus f(1)} & 1 \end{pmatrix} \quad ; \tag{5.15}$$

$$\rho_{\mathrm{c}} = \sqrt{\mathbf{Y}}\rho_{\mathrm{b}}\sqrt{\mathbf{Y}}^{\dagger} = \begin{pmatrix} 0 & 0 & 0 \\ 0 & 1-(-1)^{f(0)\oplus f(1)} & 0 \\ 0 & 0 & 1+(-1)^{f(0)\oplus f(1)} \end{pmatrix} \tag{5.16}$$

In consequence, after measurement of the spin projection in the qubit subspace the algorithm has the same (but inverted) output as the Deutsch-Jozsa algorithm (see equation 5.7). Note that, if needed, the result can be simply inverted by another Pauli Y gate (e.g. a π pulse) in the qubit subspace.

5.2 Implementation of the refined Deutsch-Jozsa (rDJ) algorithm using the NV^- center spin system

Following the scheme described in section 5.1 we realized the refined Deutsch-Jozsa algorithm by encoding both a qubit and an auxiliary state in the $S = 1$ electron spin of an NV center in a nanodiamond (see fig. 5.3a). The experiment was performed in close collaboration with USTC (Hefei, China). Aside from a few irrelevant details, the setup used was the same as described in section 2.4. Also the nanodiamonds were provided by FU Berlin and prepared as described earlier. The presence of a single NV center was verified by autocorrelation (fig. 5.3b), which clearly showed $g^2(\tau = 0) < 0.5$. At zero field the center exhibited a non-axial zero-field splitting of $D = 2.8583$ GHz and $E = 6.6$ MHz because of the strain induced by its vicinity to the surface, which assures that all degeneracies of the triplet ground state are lifted. In order to minimize unwanted excitation by off-resonance pulses and prolong the phase relaxation time by detuning of the surrounding spin bath [105], an external static magnetic field of 20 G was applied (see fig. 5.3c).

From Rabi nutation experiments (data not shown) the nutation frequencies of the ($|0\rangle \leftrightarrow |1\rangle$) auxiliary and ($|0\rangle \leftrightarrow |-1\rangle$) qubit transition were determined to be 6.94 MHz and 6.58 MHz. This results in a π pulse length of 76 ns and 72 ns, respectively. The nutation decay indicated a T_2^* of both transitions of 850 ns. T_2 measured by Hahn echo decay was $2.9 \pm 0.3\,\mu$s (see fig. 5.3d). T_1 was about $93\,\mu$s.

The technical realization of the algorithm (see fig. 5.4) can be separated into different stages. First, the initial state $\rho_{\text{ini}} = |0\rangle\langle 0|$ is prepared with $> 90\%$ probability [40] by a 5 μs long 532 nm laser pulse. After the pulse a 5 μs waiting period is included to ensure that the system is in the electronic ground state and excitations of potentially existing nearby systems contributing to luminescence background have decayed. After initialization a superposition state of the qubit sublevels (ρ_{a}) is generated by a selective $\frac{\pi}{2}$ pulse. The f-controlled gate operations U_{f_1} to U_{f_4} were implemented by combinations of 2π pulses for the four possible cases (see fig. 5.4), resulting in the respective cases of ρ_{b}. Here, using the auxiliary state $|1\rangle$ was necessary in order to apply a π phase shift to the state $|0\rangle$, which

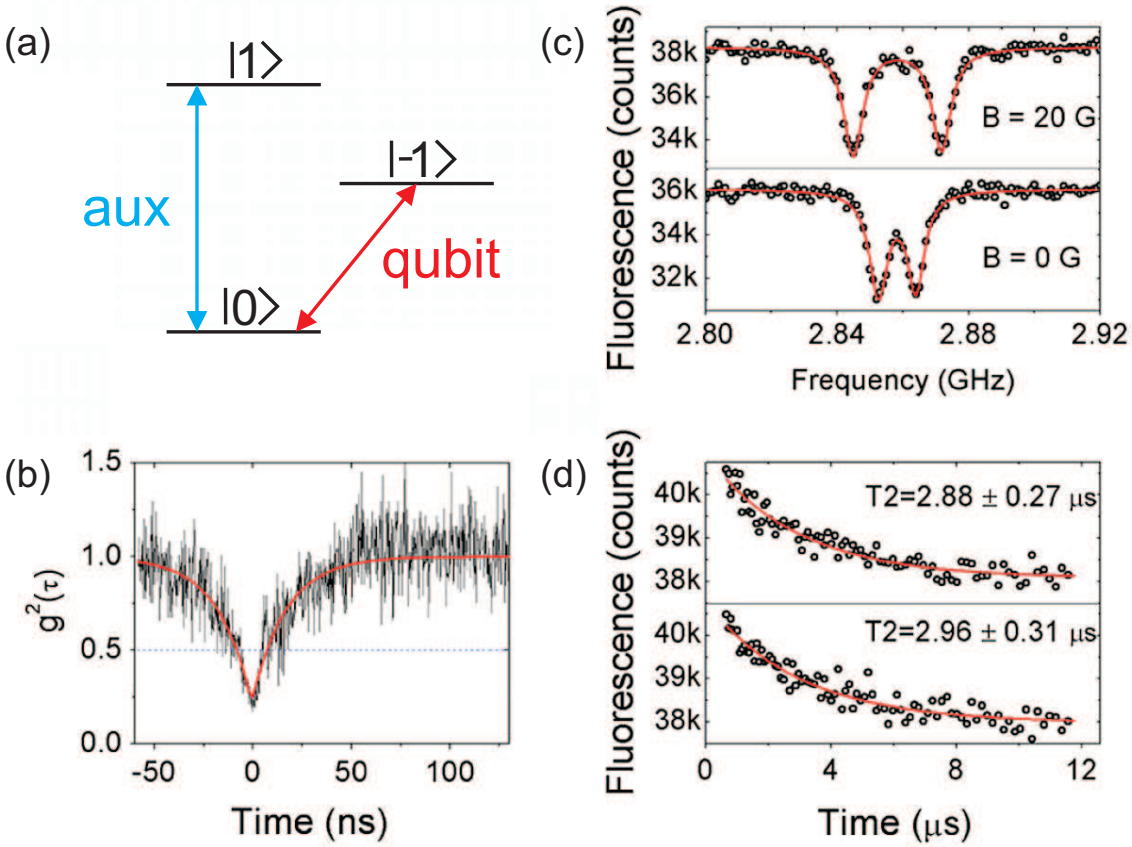

Figure 5.3: (a) Energy level diagram of the electronic ground state showing the definition of the qubit and auxiliary transition. (b) Fluorescence autocorrelation function, confirming that the nanocrystal contains a single NV center. The red curve is the exponential fit to the experimental data. (c) Optically detected magnetic resonance spectra for the single NV center, where the upper and the lower curves represent, respectively, the cases with and without the external static magnetic field (10^4 averages). Lorentzian peaks (red lines) were fitted to the experimental spectra (black circles). (d) T_2 times measured by selective excitation in the presence of an external static magnetic field, where the upper (lower) curve shows the echo decay corresponding to the transition between $|0\rangle$ to $|-1\rangle$ ($|1\rangle$).

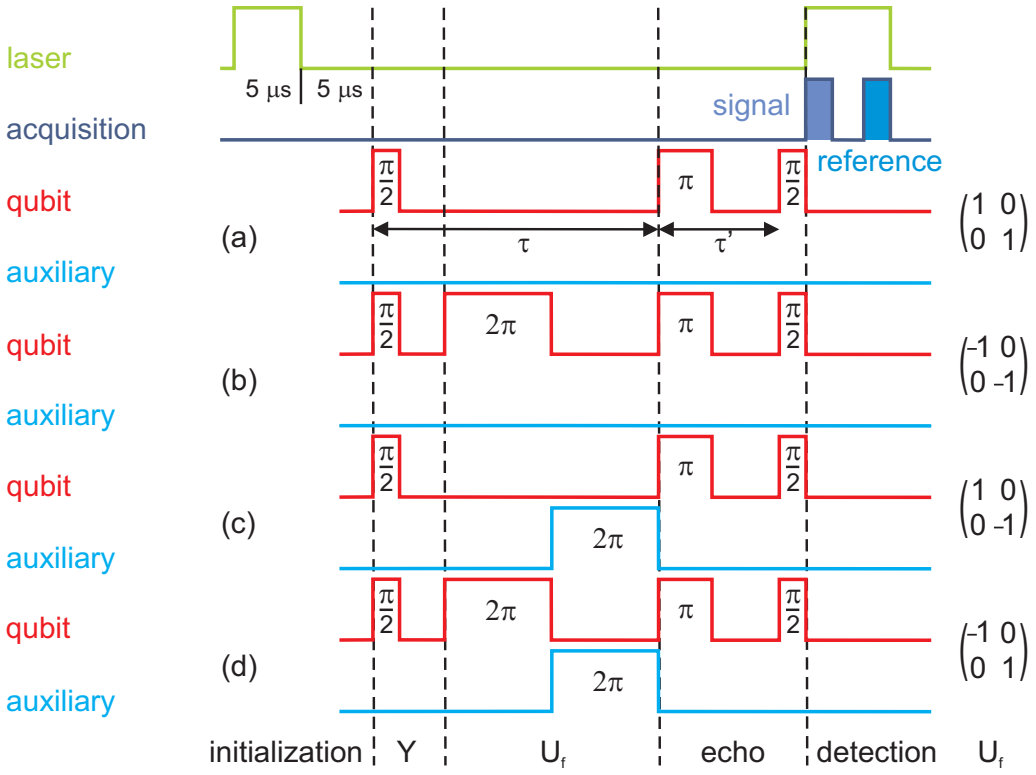

Figure 5.4: Diagram of the experimental pulse sequences used to realize the rDJ algorithm. The 532 nm laser (green line) is used to initialize the state of the NV center to $|0\rangle$ and is shut off during implementation of the algorithm. Then the laser is switched on again for detection. The signal is normalized using a reference signal at the end of the laser pulse where the spin is repolarized (blue line). Two microwave channels drive the qubit (red) and auxiliary (cyan) transition selectively. The first $\frac{\pi}{2}$ pulse is used to generate a superposition state in the qubit. The operations $U_{f_1}, U_{f_2}, U_{f_3}$ and U_{f_4} are realized by combinations of 2π pulses, as shown between the two vertical dashed lines. The detection of the result of the rDJ algorithm is realized by measuring the echo amplitude at 2τ. For better clarity the whole echo is reconstructed varying τ'.

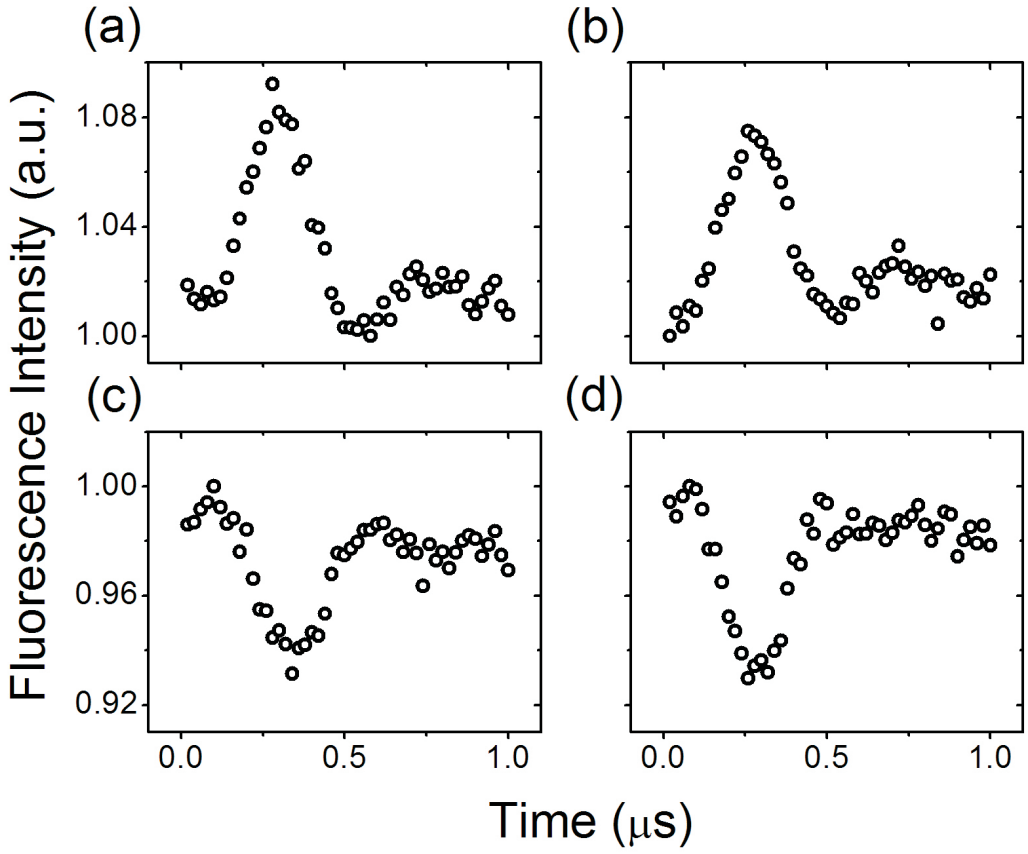

Figure 5.5: Output of the rDJ algorithm as detected by spin echoes. Positive echoes(a) and (b) correspond to the constant functions U_{f_1} and U_{f_2} respectively, while negative echoes (c) and (d) indicate the balanced function U_{f_3} and U_{f_4}, respectively. Each echo was averaged 10 million times.

is equivalent to a π rotation about Z axis in the subspace spanned by $|0\rangle$ and $|-1\rangle$ ([171], see eqn. 5.11). The total time interval for evaluation of U_f (between vertical dashed lines) was fixed to be 296 ns. To overcome the detrimental effect due to the short FID time ($T_2^* \approx 830$ ns) and to invert the signal to match the logic described earlier, the detection of the output based on a stimulated spin echo employed another π pulse, where the interval τ' between the π and $\pi/2$ pulses is varied for the echo to be recorded.

Figure 5.5 shows the results of the implementation of the rDJ algorithm, where the positive [figs. 5.5a) and 5.5b)] and the negative echoes [figs. 5.5c) and 5.5d)] correspond to the constant and balanced functions, respectively. A positive echo indicates a resulting state of $|0\rangle$ while a negative echo is equivalent to $|\pm 1\rangle$.

The quantitative result shows the expected pattern given by the values of ρ_c. In addition to the overall sign of the echo, a slight modulation can be seen that can be assigned to hyperfine interaction to the ^{14}N nucleus [39]. This interference from hyperfine interaction is responsible for slight differences in the echo amplitudes and is difficult to separate from the effects due to the finite length of the rDJ implementation. Since the latter is less than 300 ns, which is, however, still much shorter than T_2 ($2.9 \approx \mu$s), the effect from T_2 can be estimated to be 10% . The effect from FID during the pulses is greater and can be estimated by comparing the echo amplitudes in fig. 5.5. For a 2π rotation one gets a mean of 18% amplitude loss, which results in 33% loss in the worst case of driving both transitions (d).

5.3 Summary and discussion

In summary, we have achieved a pure-state quantum algorithm implementation at room temperature using a single solid-state quantum system. With respect to other systems for coherently manipulating individual spins, an implementation without cryogenic requirements greatly reduces the experimental challenge for building an actual quantum computer. However, a full demonstration of the power of quantum algorithms requires high coherence and large-scale quantum computing. The first can simply be achieved by using isotopically enriched high quality bulk diamond. Compared to the coherence time of 2.9 μs observed in our case, up two milliseconds of coherent computing is possible in the latter case. Consequently, instead of about 10 subsequent gates that can be applied in our case, application of about 10.000 gates seems feasible, which might be enough to compute relevant problems. On the other hand, scaling up the system might be achieved by optically coupling of spatially separate NV^- centers by putting the centers in optical cavities, which enhances both the zero phonon line and the collection efficiency of the emitted photons. Considerable efforts have been made in this respect [140, 141, 172, 173]. Nevertheless, our present experiment has clearly shown the unique opportunity provided by NV^- centers to study interesting physics and application of single spins and also demonstrated the great potential of the NV^- center for quantum computing. In particular use of the triplet nature of the spin system enables a new degree of freedom in future diamond quantum processing architectures.

Chapter 6

Scanning probe magnetometry using a single electron spin

One of the interesting applications arising from the ability to detect single spins is to measure magnetic fields by the size of the electron Zeeman interaction [56]. A single spin magnetic field probe offers a spatial resolution determined by the size of its spin wave function and a sensitivity (field resolution at given integration time) given by the spectroscopic resolution. Considering the size and coherence of the NV^- center in diamond, the performance of such a probe can be expected to be comparable or even superior [61] to the most sensitive magnetic sensors available, such as superconducting quantum interference devices (SQUIDs) [54, 55] and magnetic-resonance force microscopy (MRFM) [174, 175], with the added benefit of room-temperature operation. In contrast to the widely used magnetic force microscopy (MFM [176]), single spin magnetometry can be made independent of magnetic field gradients, and allows to measure absolute vector fields.
In 2008, it was first suggested by C. Degen to use the NV^- center as a magnetic field probe [177]. This proposal was followed by a series of studies regarding experimental realization [41, 57, 58, 178, 179] and theoretical developments of different measurement modes [59, 60, 180, 181]. In these studies, one can distinguish between different concepts of realization. On the one hand, there are scanning probe configurations using only a single defect center [41, 57, 58]. On the other hand, there are multiplexing approaches where many NV centers are read out simultaneously [59, 178, 179]. While this offers fast acquisition and full reconstruction of the magnetic field vectors, it is inherently limited in field resolution by dipolar interaction between the NV centers, which causes decoherence and line-broadening, and in spatial resolution by the optical diffraction limit. Moreover, elaborate post-processing of the data is necessary. Single-center scanning probes, on the other hand, provide significantly higher resolution in field and space, but this approach was considered too slow for imaging due to the inherently limited signal strength

[179]. Indeed, although contour lines corresponding to a single constant magnetic field were made visible in scanning confocal fluorescence images [57], true field images were so far obtained only with the multi-center approach [178, 179]. In all of these imaging-related studies, the full ODMR spectrum was acquired for each pixel using continuous (cw) irradiation.

Alternate ways to magnetic field sensing based on pulsed excitation and detection schemes have been proposed but not yet used for imaging, although experiments have demonstrated the soundness of the sensing principles [41, 58, 137]. While echo-based methods provide a better field sensitivity, they are only sensitive to periodically alternating fields which oscillate fast compared the decoherence rate. Static magnetic structures can be imaged only if the NV^- spin is mounted on an oscillating tip. Then, similar to the widely used MFM technique [176], only strong field gradients can be measured. For weaker gradients, those methods are less suited and the echo-free technique of Ramsey fringes [182] can be used instead. In all of these pulsed-ESR methods, pulsed light excitation and detection is required in addition to pulsed microwave channels.

Here we present an alternative experimental approach to measure static fields with a single spin scanning probe, which uses only continuous optical excitation and frequency-modulated microwaves and is thus far less demanding in resources. Our approach offers a sensitivity comparable with the related pulsed technique (Ramsey fringes) and allows the measurement of absolute vector fields. Furthermore, this method can be seamlessly integrated as a "tracking and surveying" mode in combination with the echo approaches if higher sensitivities are needed.

6.1 Principle and performance of the single spin resonance lock

It is easy to see from the Hamiltonian of the diamond electron spin (see eqn. 2.7) that for an exact determination of the local field strength B_{eff} along the symmetry axis of the NV center, only knowledge of the resonance position of one of the two allowed electron spin transitions is necessary as long as the zero-field spectrum of the center is known. In order to constantly track the resonance position without measurement of the complete spectrum, we use a modification of the field-frequency lock (fig. 6.1a)) known from magnetic resonance [183].

We use a rectangular frequency modulation (FM) of the microwave, created using two alternately switched and equally leveled signal sources

$$\nu(t) = \bar{\nu} + \nu_{mod}\Sigma\left[\cos(2\pi r_{mod}t)\right], \tag{6.1}$$

where $\bar{\nu}$ is the central frequency, ν_{mod} the modulation amplitude, r_{mod} the modulation rate, and Σ is the sign function. In our detection, we use a software lock-in

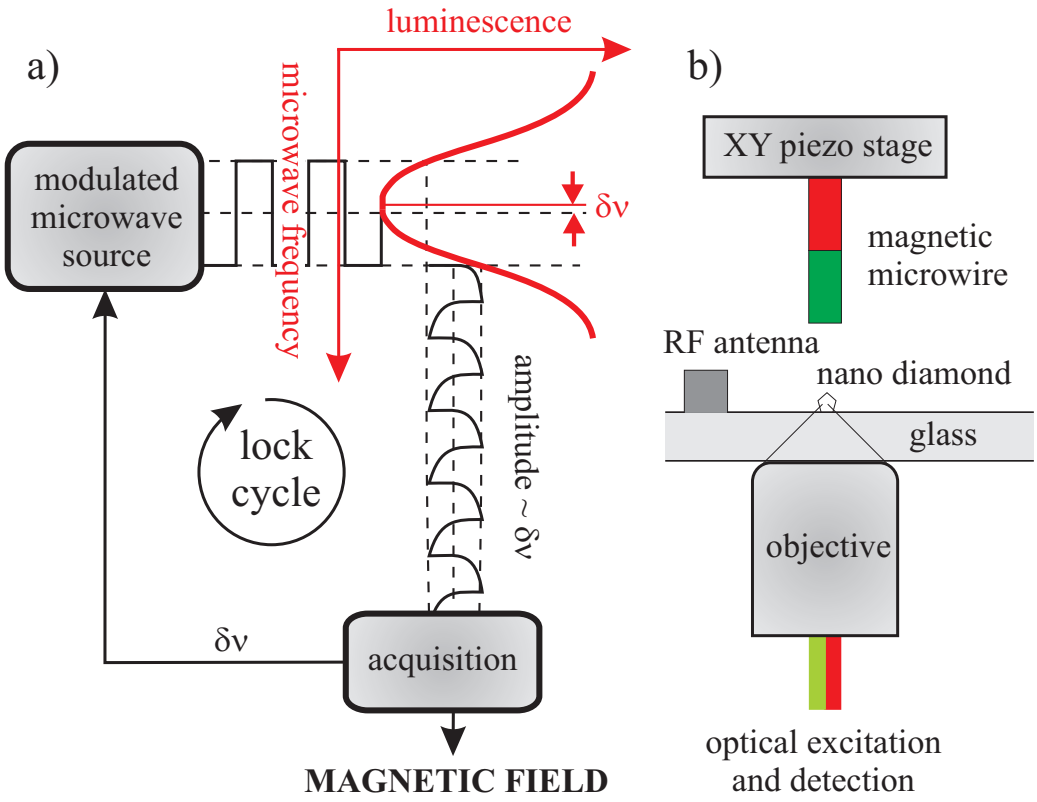

Figure 6.1: (color online) (a) A single NV spin responds to a frequency-modulated microwave close to resonance with a luminescence modulation proportional to the frequency offset. The luminescence is recorded via lock-in principle and used for frequency correction and local magnetic field calculation. a) A 100 μm magnetized steel wire is scanned over a nano-diamond containing a NV center. The microwave is generated by an antenna $\sim 100\,\mu$m apart.

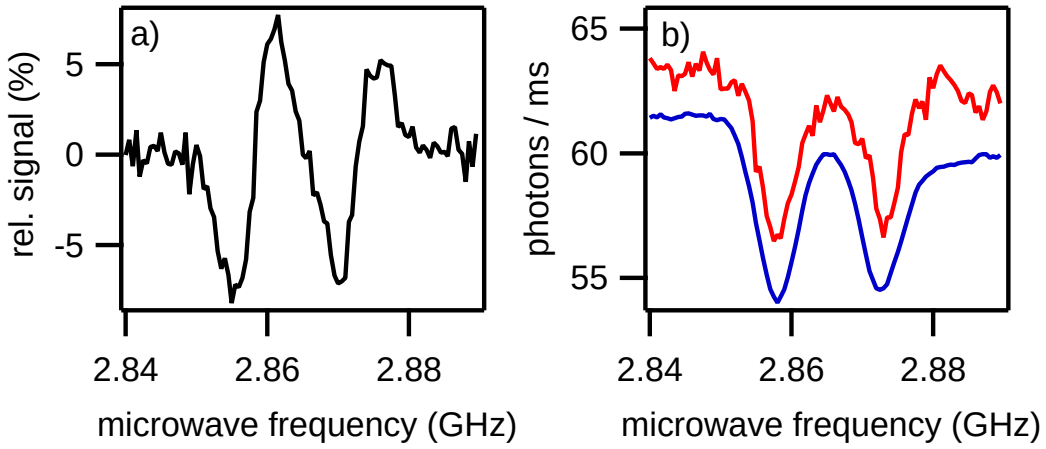

Figure 6.2: ODMR spectrum of a NV center with $E \neq 0$. (a) FM detected signal, $r_{mod} = 100$ kHz, $\nu_{mod} = 2.5$ MHz (b) integral of (a) (lower trace), CW signal (upper trace) shown for comparison. The sampling time was 100 ms per point for all measurements.

resulting in a signal proportional to the first derivative of the spectrum $L(\nu)$,

$$S(\bar{\nu}) \propto 2\nu_{mod}\frac{\partial L}{\partial \bar{\nu}} \tag{6.2}$$

as long as the modulation amplitude is small compared to the width of the peak (Fig. 6.2a)). The original spectrum can be obtained by integration resulting in a smoother curve compared to a straightforward CW measurement (Fig. 6.2b)). In case of unbiased photon shot noise this corresponds to an increased signal-to-noise ratio (SNR). One should note that the higher SNR is accompanied by a loss of spectral resolution, which is limited by ν_{mod}.

The speed of our technique relies on a fast modulation of the ODMR signal. One of the great advantages of the NV center is that its luminescence is not only spin-dependent but is also able to follow a change in $|S_z|$ within less than a microsecond. This is due to the fact that moderate laser illumination creates high spin polarization in a microsecond (see fig. 2.13) while the typical inverse Rabi nutation frequency is in the same order of magnitude (see fig. 2.14). For simplicity, in this study we consider a phase relaxation time T_2^* of a microsecond (as is the case for our type Ib nanodiamonds), so that coherent effects can be neglected. This allows us to operate at $r_{mod} = 100$ kHz, a value common in conventional electron spin resonance. The dependence of the signal amplitude $|S|$ on r_{mod} is shown in fig. 6.3, showing that the practical limitation is given by the repolarization rate.

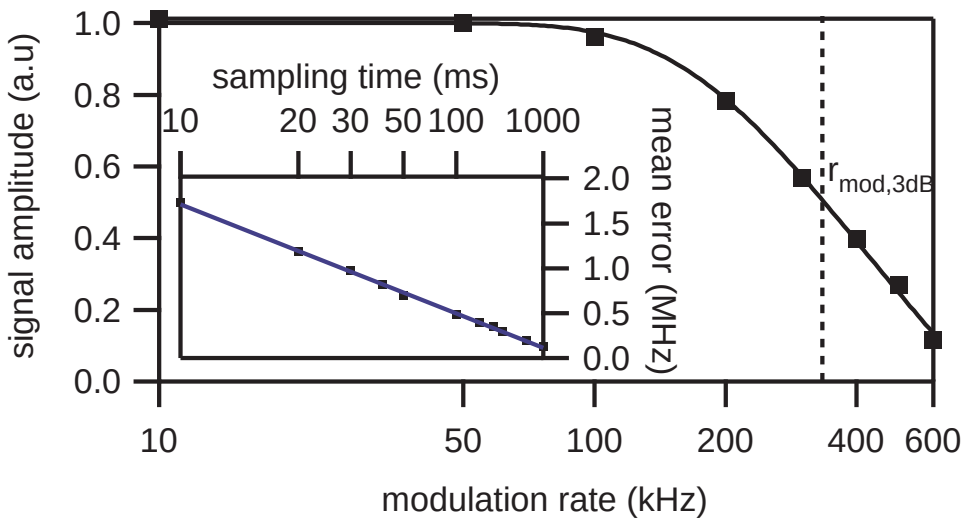

Figure 6.3: Amplitude dependence of the modulation detected signal on the modulation rate, showing a response time $\tau_{3dB} = 1/2r_{mod,3dB} = 1.5\,\mu$s ($P_{RF} = 1\,$W, $P_{Laser} = 50\,\mu$W at objective entry). The inset shows the mean error in the resonance frequency derived from the signal after averaging multiple modulation cycles. The results are in excellent agreement with a photon shot noise of 170 kHz $/\sqrt{\text{Hz}}$.

A response time $\tau_{3dB} \simeq 1.5\,\mu$s can be estimated based on the criterion of a 3 dB attenuation of the signal.

Applying Eq. (6.2) to a gaussian peak, it follows that a signal measured for a fixed microwave center frequency, but slightly off resonance, is proportional to the frequency offset. The true resonance position, and hence the magnetic field via Eq. 2.7, can be calculated. It is thus possible with our approach to locate and follow the resonance position of the NV center precisely with millisecond reaction time provided that the resonance position does not change more than the FWHM of the ODMR peak between two regulation cycles. A realtime field measurement can be conducted by continuously adjusting and recording the microwave frequency using this signal.

6.2 Sensitivity and speed

We now discuss the precision and speed of our method in terms of sensitivity $\eta = \delta B\sqrt{T}$, defined by the field error δB at given measurement time T. For a standard deviation σ of the measurement and a general repetition rate r (here:

$r = 2r_{mod}$, in pulsed techniques, $r = 1/t$ with $t =$ interrogation time, e.g., the spacing of Ramsey $\pi/2$ pulses) one obtains for any method in the photon shot noise limit [59]

$$\eta = \frac{\sigma}{\sqrt{r} dS/dB} \tag{6.3}$$

where dS/dB is the signal response to a change in the magnetic field. For d.c. measurements, a limit $r = 1/T_2^*$ obtains. Considering similar signal contrast and noise level at equal experimental conditions, and neglecting the photon collection duty cycle which is one in our case and close to one using pulsed methods at high repetition rate, any difference in sensitivity can be attributed to dS/dB. For the Ramsey fringe method, $dS/dB = \gamma T_2^*$ [59]. In our approach, assuming an inhomogeneously broadened line $S(\omega) = \exp\left[-\ln 2 \left(\omega T_2^*\right)^2\right]$ and an optimal modulation amplitude $\nu_{mod} = \sqrt{2/\ln 2}/T_2^*$, we find

$$\frac{dS}{dB} = \sqrt{\frac{8 \ln 2}{e}} \gamma T_2^* \approx 1.4 \, \gamma T_2^*. \tag{6.4}$$

We conclude that our method shows comparable and even slightly improved performance compared to Ramsey fringes, leading to a theoretical sensitivity better than 1 $\mu\mathrm{T}/\sqrt{\mathrm{Hz}}$ (see [59] for details). Our measured sensitivity shown in fig. 6.3 is somewhat reduced due to experimental issues, i.e., lower signal contrast due to weaker microwave field and optical broadening due to high laser power. The latter can be avoided using an alternating optical/microwave excitation pattern. In this study, we decided to keep the implementation as simple as possible in order to emphasize a potential advantage of our method; although we used two pulse-switched microwave generators and time-triggered detection for convenience, an easier technical implementation is possible using only a single modulated microwave source and phase-synchronized detection of a diode current.

A realtime resonance tracking of both transitions during an uncalibrated independently driven magnetic field ramp created by an external magnet is shown in Fig. 6.4. The result is in perfect agreement with the Zeeman splitting expected and shows the excellent linearity of the probe in a broad field range. Note that in our experiment that range (2.4 to 3.4 GHz) it is given by the bandwidth of the involved microwave components. For tracking we employed a locking algorithm in which $S(\nu)$ is measured for a time T and the microwave center frequency is adjusted by the factor calculated from the modulated spectrum measured at zero field. Locking of the resonance position is achieved as long as the frequency changes between two measurements are smaller than the peak width. Faster changes will eventually lead to no further correction since the signal derivative is zero both at the peak maximum and far away from it (at the baseline). This marks the breakdown of the lock. Yet, as long as the peak is still locked the mechanism now enables us to track

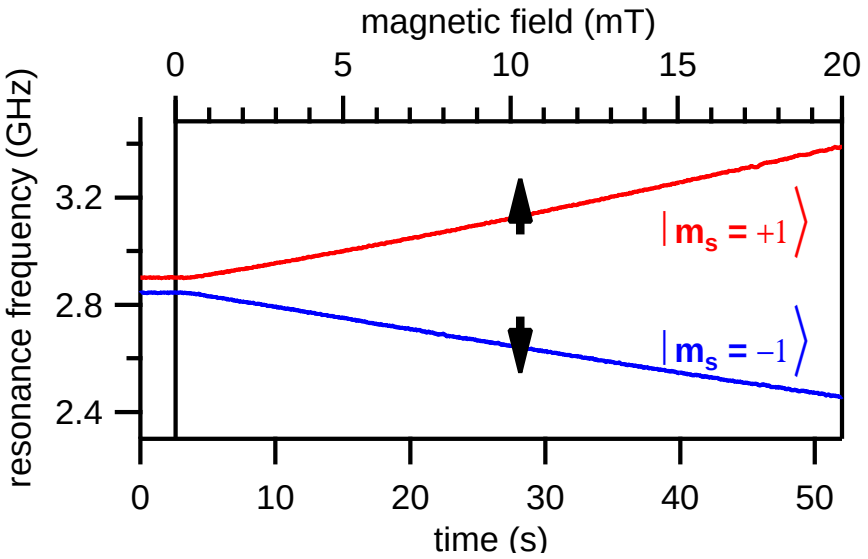

Figure 6.4: Spin transition frequencies vs. external field strength measured by tracking the resonance positions during a magnetic field sweep (sampling rate 25 Hz).

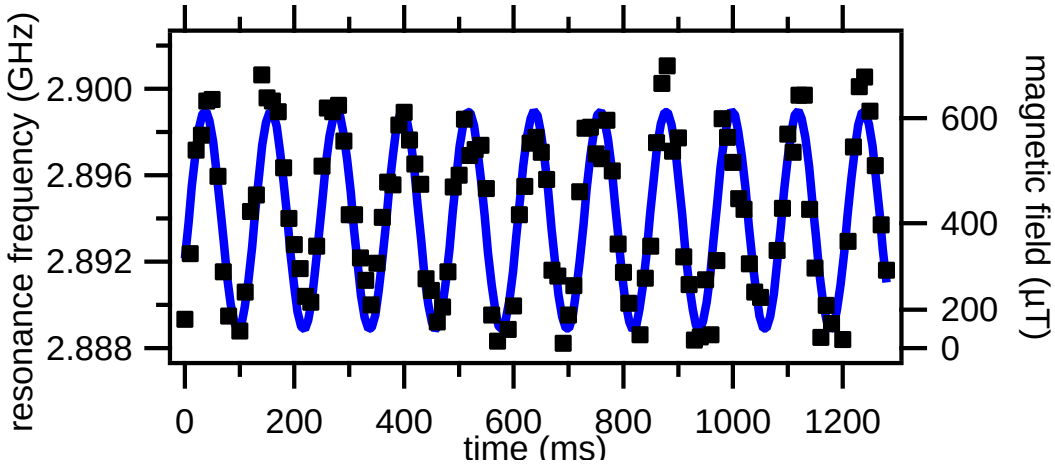

Figure 6.5: Realtime measurement of an ac magnetic field. f_{ac} was 8.3 Hz corresponding to a maximum magnetic field gradient of ~ 10 mT/s (sampling rate 100 Hz).

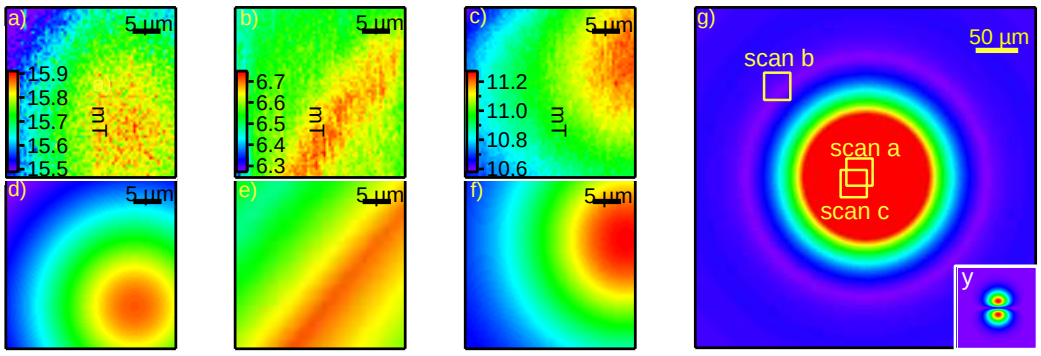

Figure 6.6: Magnetic field images taken with single NV centers. (a) NV axis normal to xy-plane ($\theta = 0°$), (b) NV axis projection on xy-plane along x, pointing slightly downwards ($\phi = 0°$, $\theta = 100°$), (c) $\phi = -60°$ (clockwise), $\theta = 45°$, (d)-(f) simulation of (a)-(c) assuming a simple dipole model (Eq. 6.5), no $B_x S_x$ components have been taken into account, (g) simulation of the normal magnetic field showing the scan areas, the inset shows an in-plane field component.

the resonance position over time. The response time is ultimately limited by the photon output and signal contrast of the color center. Taking typical values for a NV center (200 photons per ms, signal contrast $\alpha = 0.2$), the ultimate theoretical limit is ~ 0.2 ms, because $\sqrt{2}/\alpha^2$ photons are needed for a SNR of 1.

For a speed test simulating imaging conditions we applied an ac magnetic field with variable frequency f_{ac} (fig. 6.5). f_{ac} was set to the maximum value where the probe could still follow the field without interruptions due to lock break-off and can be used to estimate the maximum line frequency of a scanning probe measurement. Higher sampling rates than the one used here will lead to even higher scanning frequencies, but here we were limited by the dead time of the counter card used for fluorescence readout.

6.3 Scanning probe magnetic field imaging

Having now determined speed, range, and sensitivity of our probe, we measured the stray magnetic field of a 100 μm diameter steel wire magnetized along its axis. The wire was mounted on a XY piezoscanner placed above the sample containing nanodiamonds. The distance to the sample was about 100 μm. The scan was taken using an integration time of 150 ms per point. Due to the limited range of the piezo-scanner, only small areas of the whole field were measured. We measured several points of interest using different centers with known axis direction (Fig. 6.6). Each

measurement took about 20 minutes for two 64x64 pixel images (back- and forth scan direction). No external field was applied during the experiment. The NV center axes were determined via realtime field measurements while rotating an external magnet; this was done in absence of the sample in order to avoid changes in magnetization. Assuming the wire to behave like a magnetic point dipole at this distance, we simulated its magnetic field using

$$\vec{B} = \frac{\mu_0}{4\pi} \frac{3\vec{r}(\vec{m} \cdot \vec{r}) - \vec{m}r^2}{r^5} \quad . \tag{6.5}$$

The measured areas showed excellent agreement to the simulation. Comparing results from different centers of the same area we could find good agreement of the overall strength of the measured fields. For example by comparing the field maximum in scan (a) and (c) one finds that $B_z = B(\text{scan a}) = B(\text{scan c})/\cos(\theta_c = 45°)$, thus confirming the direction of the magnetic field vectors below the wire pointing perfectly perpendicular to the plane.

6.4 Summary and discussion

In conclusion, we have demonstrated a robust and fast responding implementation of a magnetic field measurement using a single spin in diamond. We have shown that a single spin in diamond is well suited for use in a scanning probe microscope and that also directional information can be obtained with little effort. Our approach allows to take precise 2D field images, in principle with nanometer resolution, at ambient conditions within a few minutes. This might open up fascinating new insights in cell biology, imaging of currents in nanoelectronics and the domain behavior of magnetic nanostructures. The only issue remaining for substantial increase in local resolution is a better distance control to the sample, e.g. reliable fabrication of nanodiamonds on an AFM tip, which is currently under development elsewhere [184–186].

Chapter 7

Summary and Conclusions

The purpose of the presented work was to bring the NV^- defect center in diamond and the endohedral fullerene $N@C_{60}$, both exhibiting extraordinary coherent spin systems, one step closer towards quantum application of single spins. Two of the most important applications currently under discussion are quantum information science and sensing of magnetic fields. Since for many applications near-surface centers are of fundamental interest, we focussed our study on centers in small nano-particles of 25 nm average diameter.

With the newly constructed setup we are able to polarize, coherently manipulate and measure the spin of single NV^- centers in nanodiamonds, given that the distance between the centers is larger than the optical diffraction limit. The mechanisms underlying spin polarization and spin detection by difference in photoluminescence intensity can be quantitatively understood with the help of a 5-level model that considers the transition rates between the electronic and spin levels under laser and microwave excitation. We observed coherent coupling to intrinsic nuclear spins by epr line splitting and spin echo modulations. The resolution of coupling frequencies down to 100 kHz is limited solely by the coherence of NV^- center spin, which is significantly lower (a few μs) in nanodiamonds than in electronic grade bulk diamond (0.4 ms), where decoherence is mediated by nuclear spins only. Studying the relaxation behavior, we observed a decay of the Hahn echo that is initially squared-exponential, and becomes sub-exponential for long evolution time. The behavior can be described by the theory of spectral diffusion in a strongly interacting spin bath. This leads to the conclusion that in our samples, a strongly coupled electron spin bath is present.

A small magnetic field can increase coherence by a factor of 10, with little impact of the field orientation. The same effect can be achieved by second-order dynamic decoupling using two refocussing π pulses. At higher and well-aligned fields as well as when using higher level dynamic decoupling (Uhrig or periodic), we observed no further increase of coherence, which indicates the presence of a

persistent source of decoherence that constrains T_2 to a maximum of a few tens of microseconds.
In addition to internal sources of decoherence (e.g. electron spins from dangling bonds and substitutional nitrogen), for centers close to the surface of the nanoparticles, coherence is limited by sources present outside of the diamond. We have observed that the spin of an NV^- center in some of the nanodiamonds is able to respond to the environment by means of decoherence and quenched luminescence. In particular, water on the surface can cause decoherence, as was observed in investigations on nanodiamonds in a wet gas flow. Furthermore, the spin label TEMPOL has a strong quenching effect on the luminescence and ODMR contrast of some (about half) of the centers. This can be explained by inhibition of the spin polarizing mechanism (as for example induced by spin mixing), or by enhanced non-radiative excitation decay rates.
Attempts to couple a single $N@C_{60}$ molecule to an NV^- center have proven difficult and could not yet be brought to an unambiguous conclusion. On the one hand, CW spectroscopy does not provide the resolution needed to resolve a coupling by magnetic dipolar interaction. One the other hand, the optical stability of $N@C_{60}$ is not sufficient for the radiation densities needed for excitation of the NV^- center. Still, we were able to observe a coupling to an external g=2 electron spin by double electron electron resonance (DEER) techniques. There are several, if weak, experimental indications that this spin resided on $N@C_{60}$. To overcome the challenges posed by $N@C_{60}$ in a coupling experiment, in particular background luminescence, photoinduced decay, thermally induced decay and clustering, we have synthesized a fullerene hexakisadduct that has similar spin properties to $N@C_{60}$. Spin losses during the chemical reaction and purification seem to be negligibly small. For future coupling experiments, using DEER and the fullerene hexakisadduct synthesized here seems very promising.
Furthermore, using a single isolated NV center, we have achieved a pure-state implementation of the refined Deutsch-Jozsa algorithm at room temperature. This represents the first implementation of a quantum algorithm on a single quantum system at room temperature. While the coherence of $T_2 = 2.9\mu\ s$ allowed subsequent application of less than ten gate operations, our experiment has clearly shown the unique opportunity provided by NV^- centers to study interesting physics and application of single spins and also demonstrated the great potential of the NV^- center for quantum computing. In particular use of the triplet nature of the spin system enables a new degree of freedom in future diamond quantum processing architectures.
Finally, we have used the NV center to demonstrate a robust and fast responding implementation of a magnetic field measurement. Our approach allows to take precise 2D field images, in principle with nanometer resolution, at ambient con-

ditions within a few minutes. The field sensitivity achieved in our experiment was 6 $\mu\mathrm{T}/\sqrt{\mathrm{Hz}}$, while $\sim 1\mu\mathrm{T}/\sqrt{\mathrm{Hz}}$ seems reachable with the presented approach that uses only continuous optical and chopped microwave excitation, and is hence considerably less onerous in resource requirements than other similar efforts. We imaged the same area using differently orientated centers. This allowed to partially reconstruct the field orientation. Our spatial resolution could not be fully determined yet due to the large distance between probe and sample that was unavoidable due to technical reasons. Yet, we have shown that a single spin in diamond is well suited for use in a scanning probe microscope and that also directional information can be obtained with little effort.

Outlook

While our experimental results confirm the excellent qubit properties of the NV center in diamond, they also show apparent constrictions of low-grade nanodiamonds. For scanning probe magnetometry using techniques limited in field resolution by T_2^*, these nanodiamonds are well suited. Resolving magnetic fields with atomic resolution at ambient conditions might open up fascinating new insights in cell biology (e.g imaging of neural activity), imaging of currents in nanoelectronics, and the domain behavior of magnetic nanostructures. Here, the ultimate goal would be nuclear magnetic resonance imaging exhibiting atomic resolution. For this, an optimal control of the distance to the sample is required, e.g. by reliable fabrication of nanodiamonds on an AFM tip, or injection of nanodiamonds into living cells.
For quantum computing, a longer coherence time than measured in our samples is desirable. Aside from quantum information, surface effects and coupling to paramagnetic molecules can be studied in greater detail using centers in diamond with fewer intrinsic defects. By carefully investigating the effect of water on the diamond surface, one could probably even quantitatively determine the depth of the center. Here, the best choice would be using NV centers shallowly implanted in electronic grade diamond. Given that the defect concentration is low enough, our setup is in principle able to resolve single spins in bulk diamond as well. In a preliminary study, we observed NV^- centers in low energy ion implanted electronic grade chemical vapor deposition diamond (element6 cvd, data not shown), but no solid proof of single centers was found, yet.

So, the question remains, assuming we have highly coherent shallow implanted single NV centers readily at hand, and assuming we can even couple them with molecules to small 'mini-computers', can we now finally build a scalable quantum

computer? Maybe. The big experimental challenge remaining will be to coherently couple and entangle these systems with each other. Using dipolar coupling only will, due to the small range of a few nanometers of the magnetic dipolar interaction, at some point require incredible control over material purity and spatial configuration. Furthermore, optical addressing of individual systems will become increasingly challenging. Super-resolution techniques, for example stimulated emission depletion (STED) microscopy or fluorescence lifetime microscopy (FLM) can be exploited, providing a resolution of better than 10 nm. This in practice allows for selective spin detection of two single defect centers coupled by dipolar interaction. In order to induce interactions between centers that are separated by a larger distance, an indirect interaction between two centers, for example by coupling to plasmons can be used. Yet, one has to consider that such a pattern can likely lead to new sources of decoherence. Another way to transfer the quantum information over larger distances is given by encoding it to photons ('flying qubits'). Still, efficient coupling to single photons requires a large improvement of optical cavities, since high quality factors are needed due to the spectrally broad luminescence of the centers. Finding a defect center in diamond with similar ODMR contrast and photoemission plus sharper luminescence lines might be another choice. A good part of the advantages of the NV^- center arises from diamond properties. Since there are more than 500 defect centers available, maybe an even better system can be found.

In order to shorten terms derived from equation system (2.1) we define the following rates for better clarity (all units in $[\mathrm{s}^{-1}]$):

$$\begin{aligned} L &= \rho_L B_{\mathrm{opt}} \\ R &= \rho_{\mathrm{rf}} B_{\mathrm{rf}} \\ A &= A_{\mathrm{opt}} \\ P &= p_{\mathrm{ISC,xy}} \end{aligned}$$

Thus, equation 2.6 can be written as

$$[E_{xy} + E_z]_{P_{\mathrm{rf}}=0} A_{\mathrm{opt}} = \frac{AL}{A + 2L} \quad . \tag{1}$$

Furthermore, under microwave excitation one holds

$$[E_{xy} + E_z]_{\rho_{\mathrm{rf}}\neq 0} A_{\mathrm{opt}} = \frac{kP(4AR + L(4R + P) + 2RP)}{4A^2kR + A(k(12LR + LP + 4RP) + LRP) + L(2k(4LR + LP + 3RP) + LRP)} \tag{2}$$

Calculating the ODMR contrast using equation 2.5 we get

$$\begin{aligned} &\frac{\left([E_{xy} + E_z]_{\rho_{\mathrm{rf}}=0} - [E_{xy} + E_z]_{\rho_{\mathrm{rf}}\neq 0}\right)}{\left([E_{xy} + E_z]_{\rho_{\mathrm{rf}}=0} + [E_{xy} + E_z]_{\rho_{\mathrm{rf}}\neq 0}\right)} = \\ &- \frac{R\left(2A^2k + A(2k(2L + P) + LP) + LP(2k + L)\right)}{6A^2kR + A(2k(10LR + LP + 3RP) + LRP) + L(2k(8LR + 2LP + 5RP) + LRP)} \end{aligned} \tag{3}$$

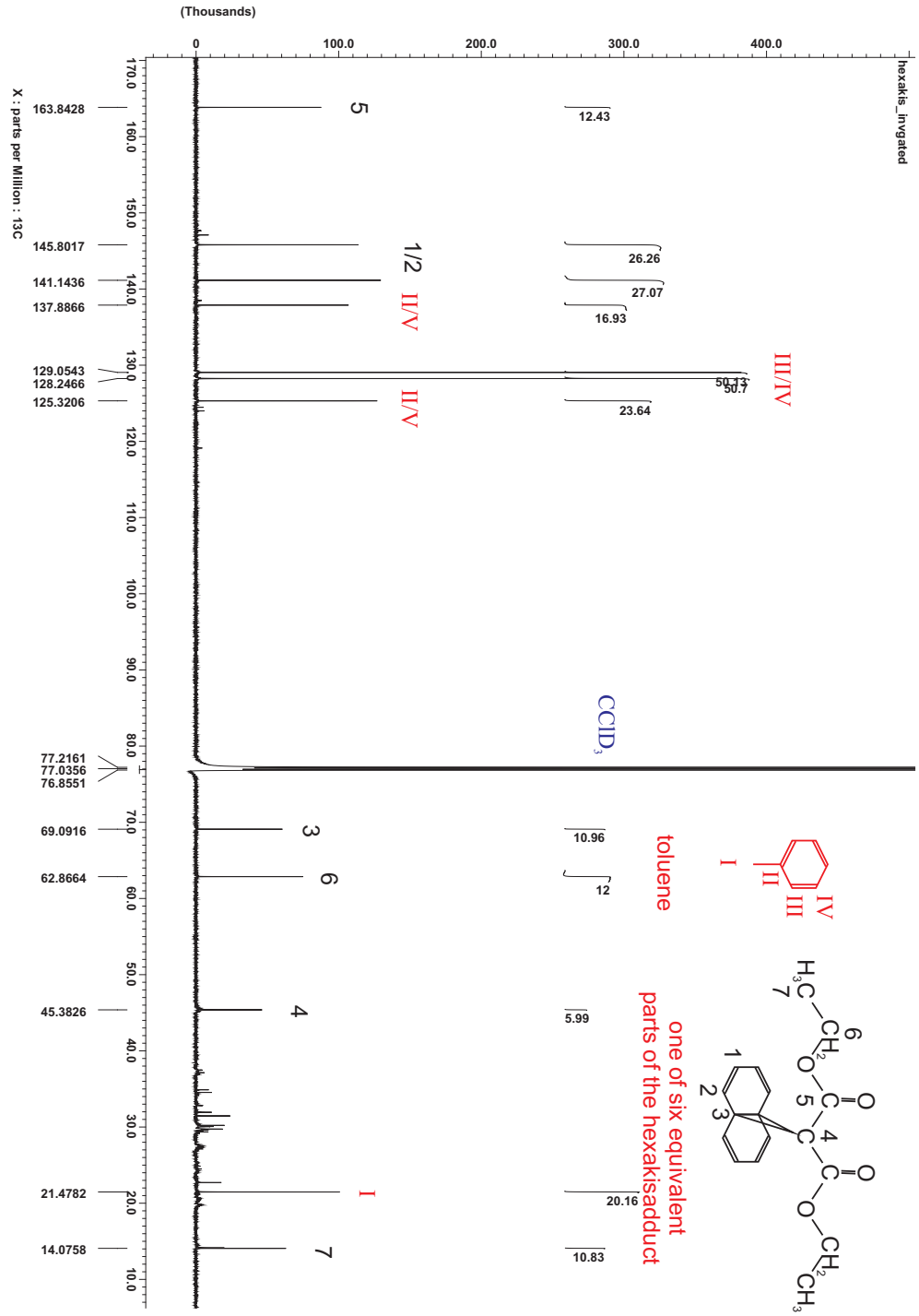

Figure 1: Carbon-13 NMR spectrum of the fullerene hexakisadduct desolved in $CClD_3$ including the peak asignments to the carbon sites of $C_{66}(COOC_2H_5)_{12}$ and traces of toluene.

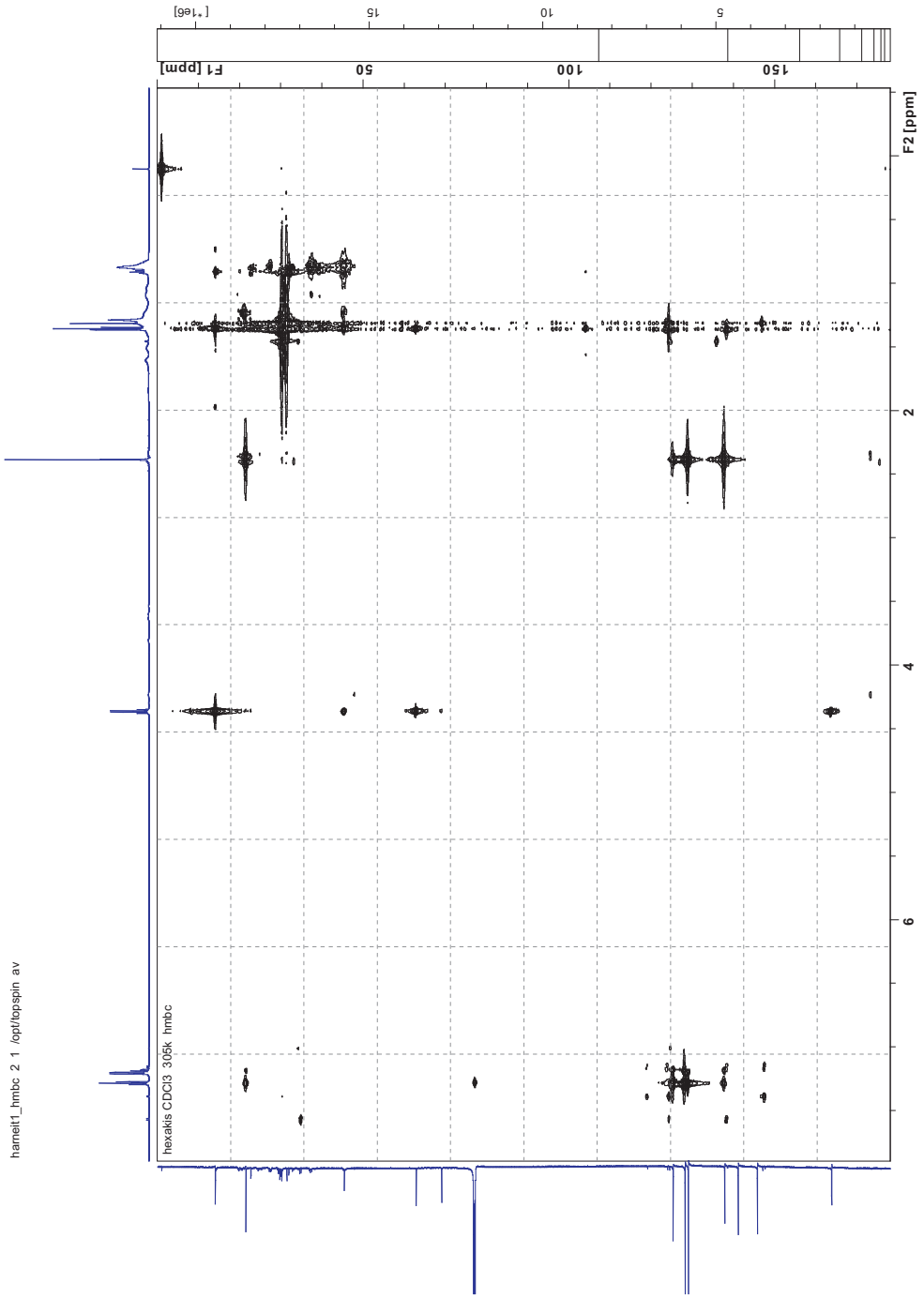

Figure 2: 2-dimensional heteronuclear multiple bond coherence (HMBC) spectrum of the fullerene hexakisadduct desolved in $CClD_3$

Acknowledgements

Finally, I like to thank all people involved directly or indirectly in my thesis. First, my gratitude is expressed to the students and collaborators who contributed directly to this work.

Bachelor students

- I thank David Quandt for design and construction of the electromagnet used in the ODMR setup [100].
- Furthermore, I thank Dorothea Scheunemann for her contribution in understanding spin loss during the formation of the endohedral fullerene hexakisadduct [187].
- Clemens Bachmair has contributed in the ODMR study of atmospheric effects on NV centers [188].
- Annett Wünschmann has experimentally explored various effects regarding the magnetic field [189].

Diploma and PhD students

- Christoph Oelmüller and Kati Hübener are greatly acknowledged for their pioneer work constructing the first cw ODMR setup in the group [93, 94].
- Thanks Juliane Kniepert for shortening the long nights while looking out for any evidence of coupled N@C_{60} molecules to NV centers and helping out with the USTC collaboration. [154].
- I greatly acknowledge the programming work performed by Björn Reimer who provided the backbone to our measurement software.
- Jiahui Yang (now at USTC, again) introduced the idea of Uhrig dynamic decoupling to us and has contributed to multiple experiments on dynamic decoupling.

Collaborators

- Great thanks goes to Fedor Jelezko (Uni Stuttgart) and his group members for fruitful discussions and generously sharing their know-how. In particular Gopalakrishnan Balasubramanian is acknowledged for the combined

AFM/confocal and DEER measurements and Boris Naydenov for preparation of a shallow implanted diamond sample.

- The group of Prof. Jiangfeng Du is acknowledged for fruitful collaboration in experimentally performing the refined Deutsch-Jozsa algorithm.

- Konstantinos Fostiropoulos (Helmholz-Zentrum Berlin) is greatly acknowledged for providing advice and access to his laboratories that have been used for sample preparations.

- The group of Prof. Bittl (FU Berlin) in general, and Marc Brecht and Jana Nieder in particular have contributed valuable equipment for test experiments. Till Biskup assisted in measuring triplet epr on N@C_{60} which verified its photochemical decay.

- Cinzia Casiraghi (FU Berlin) conducted the Raman measurements on nanodiamonds.

- I thank Prof. Andreas Hirsch and Frank Hörmann (U Erlangen) for their help and support in the synthesis of the fullerene hexakisadduct.

Referees and supervisors

- I am very grateful to my supervisor Dr. Wolfgang Harneit for providing the topic of this work and his constant support and advice. Almost everything I learned within the last years I owe to him.

- I thank Prof. U. Alexiev for kindly accepting the function of the second referee.

- In addition, I want to to express my gratitude towards Prof. J. Wrachtrup (U Stuttgart) for acting as the third referee, his invitation to visit his group and in particular the helpful discussion we had at the DPG meeting '09.

Further acknowledgements

- Thanks to my fellow PhD student Sebastian Schäfer for all the very exciting discussions we had on about any topic imaginable.

- Our former technicians Rainer Döring and Olga Bässler have to be acknowledged for teaching me how to get things running the right (and safe) way.

Acknowledgements

- Very personal thanks go to my beloved wife Kirsten who revised my perspective of the world again and again and gave me not only two lovely children, but also a better reason to live for over the past few years.
- Last but not least I want to thank my parents for their ongoing strong support of my studies and life in any way a son can possible imagine.

Bibliography

[1] W.E. Moerner and L. Kador. Optical-detection and spectroscopy of single molecules in a solid. *Phys. Rev. Lett.*, 62(21):2535, 1989. **permalink**.

[2] M. Orrit and J. Bernard. Single Pentacene Molecules Detected by Fluorescence Excitation in a Para-Terphenyl Crystal. *Phys. Rev. Lett.*, 65(21):2716, 1990. **permalink**.

[3] J. Cibert, P.M. Petroff, G.J. Dolan, S.J. Pearton, A.C. Gossard, and J.H. English. Optically detected carrier confinement to one and zero dimensions in GaAs quantum-well wires and boxes. *Appl. Phys. Lett.*, 49(19):1275, 1986. **permalink**.

[4] M.A. Reed, J.N. Randall, R.J. Aggarwal, R.J. Matyi, T.M. Moore, and A.E. Wetsel. Observation of discrete electronic states in a zero-dimensional semiconductor nanostructure. *Phys. Rev. Lett.*, 60(6):535, 1988. **permalink**.

[5] Ch. Sikorski and U. Merkt. Spectroscopy of electronic states in InSb quantum dots. *Phys. Rev. Lett.*, 62(18):2164, 1989. **permalink**.

[6] A. Steane. The ion trap quantum information processor. *App. Phys. B*, 64: 623, 1997. **permalink**.

[7] P. Treutlein, P. Hommelhoff, T. Steinmetz, T. W. Hansch, and J. Reichel. Coherence in microchip traps. *Phys. Rev. Lett.*, 92:203005, 2004. **permalink**.

[8] Kerry J. Vahala. Optical microcavities. *Nature*, 424:839, 2003. **permalink**.

[9] G.S. Solomon, M.C. Larson, and J.S. Harris. Electroluminescence in vertically aligned quantum dot multilayer light-emitting diodes fabricating by growth-induced islanding. *Appl. Phys. Lett.*, 69(13):1897, 1996. **permalink**.

[10] R. Dingle, W. Wiegmann, and C. H. Henry. Quantum States of Confined Carriers in Very Thin $Al_xGa_{1-x}As$-GaAs-$Al_xGa_{1-x}As$ Heterostructures. *Phys. Rev. Lett.*, 33:827, 1974. **permalink**.

[11] A. P. Alivisatos. Semiconductor clusters, nanocrystals, and quantum dots. *Science*, 271:933, 1996. **permalink**.

[12] P. Benioff. Quantum-mechanical hamilton models of turning machines. *J. Stat. Phys.*, 29:515, 1982. **permalink**.

[13] R.F. Feynmann. Quantum mechanical computers. *Opt. News*, 11:11, 1985. **permalink**.

[14] D.G. Cory, M. Price, W. Maas, E. Knill, R. Laflamme, W.H. Zurek, T.F. Havel, and S.S. Somaroo. Experimental quantum error correction. *Phys. Rev. Lett.*, 81:2152, 1998. **permalink**.

[15] Jonathan A. Jones, Michele Mosca, and Rasmus H. Hansen. Implementation of a quantum search algorithm on a quantum computer. *Nature*, 393:344, 1998. **permalink**.

[16] Isaac L. Chuang, Lieven M. K. Vandersypen, Xinlan Zhou, Debbie W. Leung, and Seth Lloyd. Experimental realization of a quantum algorithm. *Nature*, 393:143, 1998. **permalink**.

[17] M. A. Nielsen, E. Knill, and R. Laflamme. Complete quantum teleportation using nuclear magnetic resonance. *Nature*, 396:52, 1998. **permalink**.

[18] L.M.K. Vandersypen, M. Steffen, G. Breyta, C.S. Yannoni, M.H. Sherwood, and I.L. Chuang. Experimental realization of shor's quantum factoring algorithm using nuclear magnetic resonance. *Nature*, 414:883, 2001. **permalink**.

[19] Lieven M. K. Vandersypen, Matthias Steffen, Gregory Breyta, Costantino S. Yannoni, Mark H. Sherwood, and Isaac L. Chuang. Experimental realization of shor's quantum factoring algorithm using nuclear magnetic resonance. *Nature*, 414:883, 2001. **permalink**.

[20] R. Hanson, L. P. Kouwenhoven, J. R. Petta, S. Tarucha, and L. M. K. Vandersypen. Spins in few-electron quantum dots. *Rev. Mod. Phys.*, 79: 1217, 2007. **permalink**.

[21] D. Press, T. D. Ladd, B. Y. Zhang, and Y. Yamamoto. Complete quantum-control of a single quantumdot spin using ultrafast optical pulses. *Nature*, 456:218, 2008. **permalink**.

[22] B.E. Kane. A silicon-based nuclear spin quantum computer. *Nature*, 393: 133, 1998. **permalink**.

[23] Mark A. Eriksson, Mark Friesen, Susan N. Coppersmith, Robert Joynt, Levente J. Klein, Keith Slinker, Charles Tahan, P. M. Mooney, J. O. Chu, and S. J. Koester. Spin-based quantum dot quantum computing in silicon. *Quantum Information Processing*, 3:133, 2004. **permalink**.

[24] T. D. Ladd, D. Maryenko, Y. Yamamoto, E. Abe, and K. M. Itoh. Coherence time of decoupled nuclear spins in silicon. *Phys. Rev. B*, 71:14401, 2005. **permalink**.

[25] C. Langer et al. Long-lived qubit memory using atomic ions. *Phys. Rev. Lett.*, 95:060502, 2005. **permalink**.

[26] E. Knill et al. Randomized benchmarking of quantum gates. *Phys. Rev. A*, 77:012307, 2008. **permalink**.

[27] J. Benhelm, G. Kirchmair, C. F. Roos, and R. Blatt. Towards fault-tolerant quantum computing with trapped ions. *Nature Physics*, 4:463, 2008. **permalink**.

[28] J. C. F. Matthews, A. Politi, A. Stefanov, and J. L. OBrien. Manipulation of multiphoton entanglement in waveguide quantum circuits. *Nature Photonics*, 3:346, 2009. **permalink**.

[29] Alexander Shnirman, Gerd Schön, and Ziv Hermon. Quantum manipulations of small josephson junctions. *Phys. Rev. Lett.*, 79:2371, 1997. **permalink**.

[30] Y. Nakamura, Yu. A. Pashkin, and J. S. Tsai. Coherent control of macroscopic quantum states in a single-cooper-pair box. *Nature*, 398:786, 1999. **permalink**.

[31] D. P. DiVincenzo. The physical implementation of quantum computation. *Fortschritte der Physik*, 48:771, 2000. **permalink**.

[32] David Deutsch. The church-turing principle and the universal quantum computer. *Proceedings of the Royal Society of London A*, 400:97, 1985. URL `http://www.qubit.org/resource/deutsch85.pdf/deutsch85quantum.pdf`.

[33] David Deutsch and Richard Jozsa. Rapid solutions of problems by quantum computation. *Proceedings of the Royal Society of London A*, 439:553, 1992. **permalink**.

[34] S. Goldwasser, editor. *Proceedings of the 35th Annual Symposium on the Foundations of Computer Science*, Los Alamitos, CA, 1994. IEEE Computer Society Press.

[35] L. K. Grover. Quantum mechanics helps in searching for a needle in a haystack. *Phys. Rev. Lett.*, 79:325, 1997. **permalink**.

[36] Peter W. Shor. Scheme for reducing decoherence in quantum computer memory. *Phys. Rev. A*, 52:2493, 1995. **permalink**.

[37] J. Harrison, M.J. Sellars, and N.B. Manson. Optical spin polarisation of the n-v centre in diamond. *J. Luminescence*, 107:245, 2004. **permalink**.

[38] A. Gruber et al. Scanning confocal optical microscopy and magnetic resonance on single defect centers. *Science*, 276(5321):2012, 1997. **permalink**.

[39] F. Jelezko, T. Gaebel, I. Popa, A. Gruber, and J. Wrachtrup. Observation of coherent oscillations in a single electron spin. *Phys. Rev. Lett.*, 92(7):076401, 2004. **permalink**.

[40] F. Jelezko and J. Wrachtrup. Single defect centres in diamond: A review. *phys. stat. sol.*, 203:3207, 2007. **permalink**.

[41] Gopalakrishnan Balasubramanian et al. Ultralong spin coherence time in isotopically engineered diamond. *Nature Mat.*, 8(5):383, 2009. **permalink**.

[42] Spear and Dismukes. *Synthetic Diamond - Emerging CVD Science and Technology*. Wiley, NY, 1994.

[43] J. Meijer, B. Burchard, M. Domhan, C. Wittmann, T. Gaebel, I. Popa, F. Jelezko, and J. Wrachtrup. Generation of single color centers by focused nitrogen implantation. *Appl. Phys. Lett.*, 87:261909, 2005. **permalink**.

[44] P. Neumann, N. Mizuochi, F. Rempp, P. Hemmer, H. Watanabe, S. Yamasaki, V. Jacques, T. Gaebel, F. Jelezko, and J. Wrachtrup. Multipartite entanglement among single spins in diamond. *Science*, 320:1326, 2008. **permalink**.

[45] B. B. Buckley, G. D. Fuchs, L. C. Bassett, and D. D. Awschalom. Spin-light coherence for single-spin measurement and control in diamond. *Science*, 330: 1213, 2010. **permalink**.

[46] Philipp Neumann, Johannes Beck, Matthias Steiner, Florian Rempp, Helmut Fedder, Philip R. Hemmer, Jörg Wrachtrup, and Fedor Jelezko. Single-shot readout of a single nuclear spin. *Science*, 329:542, 2010. **permalink**.

[47] P. Neumann, R. Kolesov, B. Naydenov, J. Beck, F. Rempp, M. Steiner, V. Jacques, G. Balasubramanian, M. L. Markham, D. J. Twitchen, S. Pezzagna, J. Meijer, J. Twamley, F. Jelezko, J. . Wrachtrup, F. Jelezko, and

J. Wrachtrup. Quantum register based on coupled electron spins in a room-temperature solid. *Nature Physics*, 6:249, 2010. **permalink**.

[48] A. Young, C. Y. Hu, L. Marseglia, J. P. Harrison, J. L. OBrien, and J. G. Rarity. Cavity enhanced spin measurement of the ground state spin of an nv center in diamond. *New Journal of Physics*, 11:013007, 2009. **permalink**.

[49] Janik Wolters, Andreas W. Schell, Günter Kewes, Nils Nüsse, Max Schoengen, Henning Döscher, Thomas Hannappel, Bernd Löchel, Michael Barth, and Oliver Benson. Enhancement of the zero phonon line emission from a single nitrogen vacancy center in a nanodiamond via coupling to a photonic crystal cavity. *Appl. Phys. Lett.*, 97:141108, 2010. **permalink**.

[50] Roman Kolesov, Bernhard Grotz, Gopalakrishnan Balasubramanian, Rainer J. Sthr, Aurlien A. L. Nicolet, Philip R. Hemmer, Fedor Jelezko, and Jörg Wrachtrup. Waveparticle duality of single surface plasmon polaritons. *Nature Physics*, 5:470, 2009. **permalink**.

[51] N.B. Manson and R.L. McMurtrie. Issues concerning the nitrogen-vacancy center in diamond. *J. Luminescence*, 127:98, 2007. **permalink**.

[52] C. Bradac, T. Gaebel, N. Naidoo, M. J. Sellars, J. Twamley, L. J. Brown, A. S. Barnard, T. Plakhotnik, A. V. Zvyagin, and J. R. Rabeau. Observation and control of blinking nitrogenvacancy centres in discrete nanodiamonds. *Nature Nanotechnology*, 56:1, 2010. **permalink**.

[53] B. D. Josephson. The discovery of tunnelling supercurrents. *Rev. Mod. Phys.*, 46:251, 1974. **permalink**.

[54] R.C. Black et al. Magnetic Microscopy Using A Liquid-Nitrogen Cooled YBa2Cu3O7 Superconduction Quantum Interference Device. *Appl. Phys. Lett.*, 62:2128, 1993. **permalink**.

[55] Amit Finkler et al. Self-aligned nanoscale squid on a tip. *Nano Lett.*, 10(3): 1046, 2010. **permalink**.

[56] B Chernobrod and G Berman. Spin microscope based on optically detected magnetic resonance. *J. Appl. Phys.*, 97:014903, 2005. **permalink**.

[57] Gopalakrishnan Balasubramanian et al. Nanoscale imaging magnetometry with diamond spins under ambient conditions. *Nature*, 455(7213):648, 2008. **permalink**.

[58] J. R. Maze et al. Nanoscale magnetic sensing with an individual electronic spin in diamond. *Nature*, 455(7213):644, 2008. **permalink**.

[59] J. M. Taylor et al. High-sensitivity diamond magnetometer with nanoscale resolution. *Nature Phys.*, 4(10):810, 2008. **permalink**.

[60] L. T. Hall et al. Sensing of fluctuating nanoscale magnetic fields using nitrogen-vacancy centers in diamond. *Phys. Rev. Lett.*, 103(22):220802, 2009. **permalink**.

[61] C. L. Degen. Nanoscale magnetic microscopy with single spins. *Nature Nanotech.*, 3:643, 2008. **permalink**.

[62] Lilian Childress Benjamin Smeltzer and Adam Gali. 13c hyperfine interactions in the nitrogen-vacancy centre in diamond. *New Journal of Physics*, 13:025021, 2011. **permalink**.

[63] J. E. Field. *The Properties of Diamond*. Academic Press: London and New York, 1979.

[64] Diamond Materials GmbH (Fraunhofer IAF). The cvd diamond booklet. online, Freiburg, GERMANY, 2008. URL `http://www.diamond-materials.com/download`.

[65] Gordon Davies, Simon C. Lawson, Alan T. Collins, Alison Mainwood, and Sarah J. Sharp. Vacancy-related centers in diamond. *Phys. Rev. B*, 46:13157, 1992. **permalink**.

[66] F. Treussart, V. Jacques, E. Wu, T. Gacoin, P. Grangier, and J.-F. Roch. Photoluminescence of single colour defects in 50nm diamond nanocrystals. *Physica B*, 376:926, 2006. **permalink**.

[67] J. P. Goss, R. Jones, S. J. Breuer, P. R. Briddon, and S. Öberg. The twelve-line 1.682 ev luminescence center in diamond and the vacancy-silicon complex. *Phys. Rev. Lett.*, 77(14):3041–3044, 1996. **permalink**.

[68] N. B. Manson, J. P. Harrison, and M. J. Sellars. Nitrogen-vacancy center in diamond: Model of the electronic structure and associated dynamics. *Phys. Rev. B*, 74(10):104303, 2006. **permalink**.

[69] A S Zyubin, A M Mebel, M Hayashi, H C Chang, and S H Lin. Quantum Chemical Modeling of Photoadsorption Properties of the Nitrogen-Vacancy Point Defect in Diamond. *J. Comput. Chem.*, 30:119, 2008. **permalink**.

[70] VA Pushkarchuk, SY Kilin, AP Nizovtsev, AL Pushkarchuk, VE Borisenko, C von Borczyskowski, and AB Filonov. Ab initio modeling of the electronic and spin properties of the [NV](-) centers in diamond nanocrystals. *Optics and Spectroscopy*, 99(2):245, 2005. **permalink**.

[71] M. W. Doherty, N. B. Manson, P. Delaney, and L. C. L. Hollenberg. The negatively charged nitrogen-vacancy centre in diamond: the electronic solution. *N. J. Phys.*, 13:025019, 2011. **permalink**.

[72] Y Dumeige, F Treussart, R Alleaume, T Gacoin, JF Roch, and P Grangier. Photo-induced creation of nitrogen-related color centers in diamond nanocrystals under femtosecond illumination. *J. Luminescence*, 109(2):61–67, 2004. **permalink**.

[73] N.B. Manson and J.P. Harrison. Photo-ionization of the nitrogen-vacancy center in diamond. *Diamond and Related Materials*, 14(10):1705, 2005. **permalink**.

[74] Charles Santori, Paul E. Barclay, Kai-Mei C. Fu, and Raymond G. Beausoleil. Vertical distribution of nitrogen-vacancy centers in diamond formed by ion implantation and annealing. *Phys. Rev. B*, 79:125313, 2009. **permalink**.

[75] L. Rondin, G. Dantelle, A. Slablab, F. Grosshans, F. Treussart, P. Bergonzo, S. Perruchas, T. Gacoin, M. Chaigneau, H.-C. Chang, V. Jacques, and J.-F. Roch. Surface-induced charge state conversion of nitrogen-vacancy defects in nanodiamonds. *Phys. Rev. B*, 82:115449, 2010. **permalink**.

[76] Boris Naydenov, Friedemann Reinhard, Anke Laemmle, V. Richter, Rafi Kalish, Ulrika F. S. D'Haenens-Johansson, Mark Newton, Fedor Jelezko, and Joerg Wrachtrup. Increasing the coherence time of single electron spins in diamond by high temperature annealing. *Appl. Phys. Lett.*, 97:242511, 2010. **permalink**.

[77] M. V. Hauf, B. Grotz, B. Naydenov, M. Dankerl, S. Pezzagna, J. Meijer, F. Jelezko, J. Wrachtrup, M. Stutzmann, F. Reinhard, and J. A. Garrido. Chemical control of the charge state of nitrogen-vacancy centers in diamond. *Phys. Rev. B*, 83:081304, 2011. **permalink**.

[78] J. P. D. Martin. Fine structure of excited 3e state in nitrogen-vacancy centre of diamond. *J. Luminescence*, 81(4):237, 1999. **permalink**.

[79] N.R.S. Reddy, N.B. Manson, and E.R. Krauz. Two-laser spectral hole burning in a colour centre in diamond. *J. Luminescence*, 38:46, 1987. **permalink**.

[80] L J Rogers, S Armstrong, M J Sellars, and N B Manson. Infrared emission of the nv centre in diamond: Zeeman and uniaxial stress studies. *New J. Phys.*, 10:103024, 2008. **permalink**.

[81] A. P. Nizovtsev, S. Ya. Kilin, F. Jelezko, I. Popa, A. Gruber, and J. Wrachtrup. Nv centers in diamond: spin-selective photokinetics, optical ground-state spin alignment and hole burning. *Physica B: Cond. Mat.*, 340-342:106, 2003. **permalink**.

[82] P Neumann, R Kolesov, V Jacques, J Beck, J Tisler, A Batalov, L Rogers, N B Manson, G Balasubramanian1, F Jelezko, and J Wrachtrup. Excited-state spectroscopy of single nv defects in diamond using optically detected magnetic resonance. *New J. Phys.*, 11:013017, 2009. **permalink**.

[83] Christian Kurtsiefer, Sonja Mayer, Patrick Zarda, and Harald Weinfurter. Stable solid-state source of single photons. *Phys. Rev. Lett.*, 85(2):290, 2000. **permalink**.

[84] M. Steiner, P. Neumann, J. Beck, F. Jelezko, and J. Wrachtrup. Universal enhancement of the optical readout fidelity of single electron spins at nitrogen-vacancy centers in diamond. *Phys. Rev. B*, 81:035205, 2010. **permalink**.

[85] Joerg Wrachtrup. Defect center room-temperature quantum processors. *PNAS*, 107:9479, 2010. **permalink**.

[86] Xing-Fe He, P.T.H. Fisk, and Manson N.B. Zeeman quantum beat in nuclear quadrupole resonance probed by raman heterodyne spectroscopy. *J. Luminescence*, 53:68, 1992. **permalink**.

[87] R. J. Epstein, F. M. Mendoza, Y. K. Kato, and D. D. AWSCHALOM. Anisotropic interactions of a single spin and dark-spin spectroscopy in diamond. *Nature Physics*, 1:94, 2005. **permalink**.

[88] Ngoc Diep Lai et al. Influence of a static magnetic field on the photoluminescence of an ensemble of nitrogen-vacancy color centers in a diamond single-crystal. *Appl. Phys. Lett.*, 95(13):133101, 2009. **permalink**.

[89] Arthur Schweiger and Gunnar Jeschke. *Principles of pulse electron paramagnetic resonance*. Oxford University Press, 2001.

[90] A. Abragam. *Principles of Nuclear Magnetism*. Oxford University Press, Oxford, 1961.

[91] Charles P. Poole. *Electron Spin Resonance*. Dover, NY (reprint of 2nd edition, Wiley & Sons, NY, 1983), 2nd edition, dover edition 1996 edition, 1996.

[92] John A. Weil and James R. Bolton. *Electron Paramagnetic Resonance*. John Wiley & Sons, Inc., 2007.

[93] Kati Huebener. *Molekulare Spintronik mit endohedralen Fullerenen: Anordung und Spindetection*. PhD thesis, Freie Universitaet Berlin, Juli 2008.

[94] Christoph Oelmueller. Aufbau eines Messplatzes zur optischen Detektion magnetischer Resonanz an NV- Zentren in Diamant. Diploma thesis, Freie Universitt Berlin, Oktober 2007.

[95] Marvin Minski, 1961. Patent No. US 3013467.

[96] James Pawley, editor. *Handbook of Biological Confocal Microscopy*. Springer, New York, second edition, 1995.

[97] C. J. R. Sheppard, D. M. Hotton, and David Shotton. *Confocal Laser Scanning Microscopy*. BIOS Scientific Publishers, 1997.

[98] Alberto Diaspro, editor. *Confocal and Two-Photon Microscopy: Foundations, Applications and Advances*. Wiley-Liss, New York, 2001.

[99] R. H. Webb. Confocal optical microscopy. *Rep. Prog. Phys.*, 59:427, 1996. **permalink**.

[100] David Quandt. Aufbau eines Magnetsystems zur Magnetresonanzmessung an Einzelzentren. Bachelor's thesis, Freie Universitaet Berlin, Mai 2009.

[101] Stefan Stoll and Arthur Schweiger. Easyspin, a comprehensive software package for spectral simulation and analysis in epr. *J. Magn. Reson.*, 178:42, 2006. **permalink**.

[102] L. Childress, M. V. Gurudev Dutt, J. M. Taylor, A. S. Zibrov, F. Jelezko, J. Wrachtrup, P. R. Hemmer, and M. D. Lukin. Coherent dynamics of coupled electron and nuclear spin qubits in diamond. *Science*, 314:281, 2006. **permalink**.

[103] J. R. Rabeau, P. Reichart, G. Tamanyan, D. N. Jamieson, S. Prawer, F. Jelezko, T. Gaebel, I. Popa, M. Domhan, and J. Wrachtrup. Implantation of labelled single nitrogen vacancy centers in diamond using 15n. *Appl. Phys. Lett.*, 88:023113, 2006. **permalink**.

[104] T Gaebel, M Domhan, I Popa, C Wittmann, P Neumann, F Jelezko, JR Rabeau, N Stavrias, AD Greentree, S Prawer, Meijer J, J Twamley, PR Hemmer, and J Wrachtrup. Room-temperature coherent coupling of single spins in diamond. *Nature Physics*, 2:408, 2006. **permalink**.

[105] J. R. Maze, J. M. Taylor, and M. D. Lukin. Electron spin decoherence of single nitrogen-vacancy defects in diamond. *Phys. Rev. B*, 78(9):094303, 2008. **permalink**.

[106] I. Popa, T. Gaebel, M. Domhan, C. Wittmann, F. Jelezko, and J. Wrachtrup. Energy levels and decoherence properties of single electron and nuclear spins in a defect center. *Phys. Rev. B*, 70:201203, 2004. **permalink**.

[107] X.-F. He, N. B. Manson, and P.T. H. Fisk. Paramagnetic resonance of photoexcited n-v defects in diamond. ii. hyperfine interaction with the 14n nucleus. *Phys. Rev. B*, 47:8816, 1993. **permalink**.

[108] F. Jelezko, T. Gaebel, I. Popa, M. Domhan, A. Gruber, and J. Wrachtrup. Observation of coherent oscillation of a single nuclear spin and realization of a two-qubit conditional quantum gate. *Phys. Rev. Lett.*, 93:130501, 2004. **permalink**.

[109] Adam Gali. Identification of individual ^{13}c isotopes of nitrogen-vacancy center in diamond by combining the polarization studies of nuclear spins and first-principles calculations. *Phys. Rev. B*, 80:241204, 2009. **permalink**.

[110] F. R. L. Schoening and L. A. Vermeulen. X-ray measurement of the debye temperature for diamond at low temperatures. *Solid State Communications*, 7:15, 1969. **permalink**.

[111] J. M. Kikkawa and D. D. Awschalom. Resonant spin amplification in n-type gaas. *Phys. Rev. Lett.*, 80:4313, 1998. **permalink**.

[112] K. M. Salikhov and Yu. D. Tsvetkov. *Time Domain Electron Spin Resonance*, chapter Electron Spin-Echo Studies of Spin-Spin Interactions in Solids, pages 231–277. John Wiley and Sons, NY, 1979.

[113] J. R. Klauder and P. W. Anderson. Spectral diffusion decay in spin resonance experiments. *Phys. Rev.*, 125:912–932, 1962. **permalink**. Seminal Paper on T2 Spectral Diffusion Theory.

[114] Rogerio de Sousa and S. Das Sarma. Theory of nuclear-induced spectral diffusion: Spin decoherence of phosphorus donors in si and gaas quantum dots. *Phys. Rev. B*, 68:115322, 2003. **permalink**.

[115] W. M. Witzel, Rogerio de Sousa, and S. Das Sarma. Quantum theory of spectral-diffusion-induced electron spin decoherence. *Phys. Rev. B*, 72: 161306, 2005. **permalink**.

[116] P. L. Stanwix, L. M. Pham, J. R. Maze, D. Le Sage, T. K. Yeung, P. Cappellaro, P. R. Hemmer, A. Yacoby, M. D. Lukin, and R. L. Walsworth. Coherence of nitrogen-vacancy electronic spin ensembles in diamond. *Phys. Rev. B*, 82:201201, 2010. **permalink**.

[117] H.Y. Carr and E.M. Purcell. Effects of diffusion on free precession in nuclear magnetic resonance experiments. *Physical Review*, 94:630, 1954. **permalink**.

[118] J. R. Harbridge, S. S. Eaton, and G. R. Eaton. Comparison of electron spin relaxation times measured by carrpurcellmeiboomgill and two-pulse spin-echo sequences. *Journal of Magnetic Resonance*, 164:4453, 2003. **permalink**.

[119] N. C. Nielsen, C. Kehlet, S. J. Glaser, and N. Khaneja. *Optimal Control Methods in NMR Spectroscopy*. Encyclopedia of Magnetic Resonance. John Wiley & Sons, Ltd., 2010. **permalink**.

[120] K. Khodjasteh and D. A. Lidar. Fault-tolerant quantum dynamical decoupling. *Phys. Rev. Lett.*, 95:180501, 2005. **permalink**.

[121] O. Kern and G. Alber. Controlling quantum systems by embedded dynamical decoupling schemes. *Phys. Rev. Lett.*, 95:250501, 2005. **permalink**.

[122] L. F. Santos and L. Viola. Enhanced convergence and robust performance of randomized dynamical decoupling. *Phys. Rev. Lett.*, 97:150501, 2006. **permalink**.

[123] Michael J. Biercuk, Hermann Uys, Aaron P. VanDevender, Nobuyasu Shiga, Wayne M. Itano, and John J. Bollinger. Optimized dynamical decoupling in a model quantum memory. *Nature*, 458:996–1000, 2009. **permalink**.

[124] Jiangfeng Du, Xing Rong, Nan Zhao, Ya Wang, Jiahui Yang, and R. B. Liu. Preserving electron spin coherence in solids by optimal dynamical decoupling. *Nature*, 461:1265–1268, 2009. **permalink**.

[125] J. S. Waugh and C. H. Wang. Multiple spin echoes in dipolar solids. *Phys. Rev.*, 162:209–216, 1967. **permalink**.

[126] G. de Lange, Z. H. Wang, D. Riste, V. V. Dobrovitski, and R. Hanson. Universal dynamical decoupling of a single solid-state spin from a spin bath. *Science*, 330:60, 2010. **permalink**.

[127] C. A. Ryan, J. S. Hodges, and D. G. Cory. Robust decoupling techniques to extend quantum coherence in diamond. *Phys. Rev. Lett.*, 105:200402, 2010. **permalink**.

[128] Boris Naydenov, Florian Dolde, Liam T. Hall, Chang Shin, Helmut Fedder, Lloyd C. L. Hollenberg, Fedor Jelezko, and Jörg Wrachtrup. Dynamical decoupling of a single-electron spin at room temperature. *Phys. Rev. B*, 83: 081201, 2011. **permalink**.

[129] W. M. Witzel and S. DasSarma. Concatenated dynamical decoupling in a solid-state spin bath. *Phys. Rev. B*, 78:241303, 2007. **permalink**.

[130] G. S. Uhrig. Keeping a Quantum Bit Alive by Optimized π-Pulse Sequences. *Phys. Rev. Lett.*, 98:100504, 2007. **permalink**.

[131] K. Khodjasteh, K. A. Lidar, and L. Viola. Arbitrarily accurate dynamical control in open quantum systems. *Phys. Rev. Lett.*, 104:090501, 2010. **permalink**.

[132] L. T. Hall, C. D. Hill, J. H. Cole, and L. C. L. Hollenberg. Ultra-sensitive diamond magnetometry using optimal dynamic decoupling. *Phys. Rev. B*, 82:045208, 2010. **permalink**.

[133] G. S. Uhrig. Concatenated control sequences based on optimized dynamic decoupling. *Phys. Rev. Lett.*, 102:120502, 2009. **permalink**.

[134] R. Hanson, V. V. Dobrovitski, A. E. Feiguin, O. Gywat, and D. D. Awschalom. Coherent dynamics of a single spin interacting with an adjustable spin bath. *Science*, 320:352, 2008. **permalink**.

[135] K. Khodjasteh and K. A. Lidar. Performance of deterministic dynamical decoupling schemes: Concatenated and periodic pulse sequences. *Phys. Rev. A*, 75:062310, 2007. **permalink**.

[136] S. Pasini and G. S. Uhrig. Optimized dynamical decoupling for power-law noise spectra. *Phys. Rev. A*, 81:012309, 2010. **permalink**.

[137] Chang Shin et al. Sub-optical resolution of single spins using magnetic resonance imaging at room temperature in diamond. *J. Luminescence*, 130(9): 1635 – 1645, 2010. **permalink**.

[138] Steven Prawer and Andrew D. Greentree. Diamond for quantum computing. *Science*, 320:1601, 2008. **permalink**.

[139] T. D. Ladd, F. Jelezko, R. Laflamme, Y. Nakamura, C. Monroe, and J. L. O/'Brien. Quantum computers. *Nature*, 464:45, 2010. **permalink**.

[140] Michael Barth, Stefan Schietinger, Sabine Fischer, Jan Becker, Nils Nusse, Thomas Aichele, Bernd Lochel, Carsten Sonnichsen, and Oliver Benson. Nanoassembled plasmonic-photonic hybrid cavity for tailored light-matter coupling. *Nano Letters*, 10:891, 2010. **permalink**.

[141] S. Schietinger, T. Schröder, and O. Benson. One-by-one coupling of single defect centers in nanodiamonds to high-q modes of an optical microresonator. *Nanoletters*, 8:3911, 2008. **permalink**.

[142] D. Marcos, M. Wubs, J. M. Taylor, R. Aguado, M. D. Lukin, and A. S. Sørensen. Coupling nitrogen-vacancy centers in diamond to superconducting flux qubits. *Phys. Rev. Lett.*, 105:210501, 2010. **permalink**.

[143] T. Almeida Murphy, Th. Pawlik, A. Weidinger, M. Höhne, R. Alcala, and J.-M. Spaeth. Observation of atomlike nitrogen in nitrogen-implanted solid c60. *Phys. Rev. Lett.*, 77:1075, 1996. **permalink**.

[144] Wolfgang Harneit. Fullerene-based electron-spin quantum computer. *Phys. Rev. A*, 65:032322, 2002. **permalink**.

[145] J Meijer, S. Pezzagna, T. Vogel, B. Burchard, HH. Bukow, IW. Rangelow, Y. Sarov, H. Wiggers, I. Pluemmel, F. Jelezko, J. Wrachtrup, F. Schmidt-Kaler, W. Schnitzler, and K. Singer. Towards the implanting of ions and positioning of nanoparticles with nm spatial resolution. *Applied Physics A*, 91:567, 2008. **permalink**.

[146] S. Prawer, K. W. Nugent, D. N. Jamieson, J. O. Orwa, L. A. Bursill, and J. L. Peng. The raman spectrum of nanocrystalline diamond. *Chem. Phys. Lett.*, 332:93, 2000. **permalink**.

[147] S.M. Pimenov, V.V. Kononenko, V.G. Ralchenko, V.I. Konov, S. Gloor, W. Lthy, H.P. Weber, and A.V. Khomich. Laser polishing of diamond plates. *Applied Physics A*, 69:81, 1999. **permalink**.

[148] Ray Freeman. *Spin Choreography*, chapter 11, page 335. Oxford University Press, 2003.

[149] A. Goto, J. C. Scaiano, and L. Maretti. Photolysis of an alkoxyamine using intramolecular energy transfer from a quinoline antenna-towards photoinduced living radical polymerization. *Photochem. Photobiol. Sci.*, 6:833, 2007. **permalink**.

[150] Alok D. Bokare and Archita Patnaik. Microscopic diffusion model applied to c60 fullerene fractals in carbon disulphide solution. *J. Chem. Phys.*, 119: 4529, 2003. **permalink**.

[151] Alok D. Bokare and Archita Patnaik. Self-organization of c60 nanoparticles in carbon disulfide solution. *J. Phys. Chem. B*, 107:6079, 2003. **permalink**.

[152] Burkhard Goedde. *Synthese und Spektroskopie angereicherter stickstoffendohedraler Fullerene*. PhD thesis, Universität Darmstadt, 2001.

[153] Masao Ichida, Arao Nakamura, Hisanori Shinohara, and Yahachi Saitoh. Observation of triplet state of charge-transfer excitons in c60 thin film. *Chem. Phys. Lett.*, 289:579, 1998. **permalink**.

[154] Juliane Kniepert. Optisch detektierte Magnetresonanz an NV-Zentren in Diamant. Diploma thesis, Freie Universitaet Berlin, Oktober 2008.

[155] Julia Tisler et al. Fluorescence and Spin Properties of Defects in Single Digit Nanodiamonds. *ACS Nano*, 3(7):1959, 2009. **permalink**.

[156] Tomohiro Suetsuna, Nita Dragoe, Wolfgang Harneit, Alois Weidinger, Hidekazu Shimotani, Seitaro Ito, Hidenori Takagi, and Koichi Kitazawa. Separation of n2@c60 and n@c60. *Chemistry European Journal*, 8:5079, 2002. **permalink**.

[157] Peter Jakes, Klaus-Peter Dinse, Carola Meyer, Wolfgang Harneit, and Alois Weidinger. Purification and optical spectroscopy of n@c60. *Phys. Chem. Chem. Phys.*, 5:4080, 2003. **permalink**.

[158] H. W. Kroto, J. R. Heath, S. C. O'Brien, R. F. Curl, and R. E. Smalley. C60: Buckminsterfullerene. *Nature*, 318:162, 1985. **permalink**.

[159] Tomiyuki Tsubo and Keiichiro Nasu. Theory for exciton effects on light absorption spectra of f.c.c. type c60 crystal. *Solid State Communications*, 91:907, 1994. **permalink**.

[160] M. Waiblinger, K. Lips, W. Harneit, and A. Weidinger. Thermal stability of the endohedral fullerenes nac60 , nac70 , and pac60. *Phys. Rev. B*, 63: 045421, 2000. **permalink**.

[161] Uwe Reuther, Torsten Brandmueller, Wolfgang Donaubauer, Frank Hampel, and Andreas Hirsch. A highly regioselective approach to multiple adducts of c60 governed by strain minimization of macrocyclic malonate addends. *Chemistry, A European Journal*, 8(10):2261, 2002. ISSN 1521-3765. **permalink**.

[162] Carsten Bingel. Cyclopropanierung von fullerenen. *Chemische Berichte*, 126: 1957, 1993. **permalink**.

[163] Elke Dietel, Andreas Hirsch, Bjoern Pietzak, Markus Waiblinger, Klaus Lips, Alois Weidinger, Andrea Gruss, and Klaus-Peter Dinse. Atomic nitrogen encapsulated in fullerenes: Effects of cage variations. *J. Am. Chem. Soc.*, 121:2432, 1999. **permalink**.

[164] Andreas Hirsch, Iris Lamparth, and Thomas Groesser. Regiochemistry of multiple additions to the fullerene core: Synthesis of a th-symmetric hexakisadduct of c60 with bis(ethoxycarbonyl)methylene. *J. Am. Chem. Soc.*, 116:9385, 1994. **permalink**.

[165] Iris Lamparth, Cacilia Maichle - Mossmer, and Andreas Hirsch. Reversible Template-Directed Activation of Equatorial Double Bonds of the Fullerene Framework: Regioselective Direct Synthesis, Crystal Structure, and Aromatic Properties of Th-C66(COOEt)12. *Angew. Chem. Int. Ed.*, 34:1607, 1995. **permalink**.

[166] David Collins, K. W. Kim, and W. C. Holton. Deutsch-jozsa algorithm as a test of quantum computation. *Phys. Rev. A*, 58(3):R1633, 1998. **permalink**.

[167] P. Bianucci et al. Experimental realization of the one qubit deutsch-jozsa algorithm in a quantum dot. *Phys Rev. B*, 69:161303, 2004. **permalink**.

[168] M. Scholz et al. Deutsch-jozsa algorithm using triggered single photons from a single quantum dot. *Phys. Rev. Lett.*, 96:180501, 2006. **permalink**.

[169] M. Mohseni et al. Experimental application of decoherence-free subspaces in an optical quantum-computing algorithm. *Phys. Rev. Lett.*, 91:187903, 2003. **permalink**.

[170] S. Gulde et al. Implementation of the deutschjozsa algorithm on an ion-trap quantum computer. *Nature*, 421:48, 2003. **permalink**.

[171] G. S. Agarwal, M. O. Scully, and H. Walther. Inhibition of decoherence due to decay in a continuum. *Phys. Rev. Lett.*, 86(19):4271, 2001. **permalink**.

[172] C. F. Wang, R. Hanson, D. D. Awschalom, E. L. Hu, T. Feygelson, J. Yang, and J. E. Butler. Fabrication and characterization of two-dimensional photonic crystal microcavities in nanocrystalline diamond. *Appl*, 91:201112, 2007. **permalink**.

[173] C. F. Wang, Y-S. Choi, , J. C. Lee, E. L. Hu, J. Yang, and J. E. Butler. Observation of whispering gallery modes in nanocrystalline diamond microdisks. *Appl. Phys. Lett.*, 90:081110, 2007. **permalink**.

[174] H. J. Mamin et al. Nuclear magnetic resonance imaging with 90-nm resolution. *Nature Nanotech.*, 2(5):301, 2007. **permalink**.

[175] D Rugar et al. Single spin detection by magnetic resonance force microscopy. *Nature*, 430(6997):329, 2004. **permalink**.

[176] Y. Martin and H. K. Wickramasinghe. Magnetic imaging by force microscopy with 1000 [a-ring] resolution. *Appl. Phys. Lett.*, 50(20):1455, 1987. **permalink**.

[177] C. L. Degen. Scanning magnetic field microscope with a diamond single-spin sensor. *Appl. Phys. Lett.*, 92:243111, 2008. **permalink**.

[178] B. J. Maertz et al. Vector magnetic field microscopy using nitrogen vacancy centers in diamond. *Appl. Phys. Lett.*, 96(9):092504, 2010. **permalink**.

[179] S. Steinert et al. High sensitivity magnetic imaging using an array of spins in diamond. *Rev. Sci. Inst.*, 81:043705, 2010. **permalink**.

[180] Jared H. Cole and Lloyd C. L. Hollenberg. Scanning quantum decoherence microscopy. *Nanotech.*, 20(49):495401, 2009. **permalink**.

[181] P. Cappellaro and M. D. Lukin. Quantum correlation in disordered spin systems: Applications to magnetic sensing. *Phys Rev. A*, 80(3):032311, 2009. **permalink**.

[182] Norman F. Ramsey. A molecular beam resonance method with separated oscillating fields. *Phys. Rev.*, 78:695, 1950. **permalink**.

[183] GE Maciel, PD Ellis, and DC Hoefer. Carbon-13 Chemical Shifts Of Carbonyl Group .V. Observation Of Deuterium Isotope Effect Using Carbon-13 Field-Frequency Lock. *J. Phys. Chem.*, 71(7):2160, 1967. **permalink**.

[184] T. van der Sar et al. Nanopositioning of a diamond nanocrystal containing a single nitrogen-vacancy defect center. *Appl. Phys. Lett.*, 94(17):173104, 2009. **permalink**.

[185] E. Ampem-Lassen et al. Nano-manipulation of diamond-based single photon sources. *Opt. Express*, 17(14):11287, 2009. **permalink**.

[186] Aurelien Cuche et al. Grafting fluorescent nanodiamonds onto optical tips. *J. Nanophotonics*, 4:043506, 2010. **permalink**.

[187] Dorothea Scheunemann. Photostabile N@C60 Molekuele fuer die optische Spindetektion. Bachelor's thesis, Freie Universitaet Berlin, Juni 2009.

[188] Clemens Bachmair. Aeussere Einfluesse auf Spins in Diamant. Bachelor's thesis, Freie Universitaet Berlin, Mai 2010.

[189] Annett Wuenschmann. Spin-Spin-Kopplung von NV-Zentren in Nanodiamanten mit ihrer Umgebung. Bachelor's thesis, Freie Universitaet Berlin, Oktober 2010.

[190] Kati Huebener, Rolf Simon Schoenfeld, Juliane Kniepert, Christoph Oelmueller, and Wolfgang Harneit. Odmr of nv centers in nano-diamonds covered with n@c60. *phys. stat. sol. (b)*, 245:2013, 2008. **permalink**.

[191] Fazhan Shi, Xing Rong, Nanyang Xu, Ya Wang, Jie Wu, Bo Chong, Xinhua Peng, Juliane Kniepert, Rolf-Simon Schoenfeld, Wolfgang Harneit, Mang Feng, and Jiangfeng Du. Room-temperature implementation of the deutsch-jozsa algorithm with a single electronic spin in diamond. *Phys. Rev. Lett.*, 105:040504, 2010. **permalink**.

[192] Rolf Simon Schoenfeld and Wolfgang Harneit. Real time magnetic field sensing and imaging using a single spin in diamond. *Phys. Rev. Lett.*, 106: 030802, 2011. **permalink**.

List of Figures

List of publications

Parts of this work have already been published in advance in different journals. First, some of the early preliminary results and theory of couplings between $N@C_{60}$ and the NV^- center (see chapter 4) have been published as

[190] Kati Huebener, Rolf Simon Schoenfeld, Juliane Kniepert, Christoph Oelmueller and Wolfgang Harneit:
ODMR of NV centers in nano-diamonds covered with $N@C_{60}$, physica status solidi (b) **245**, No. 10,2013-2017 (2008)

The work about the refined Deutsch-Josza algorithm on the NV^- center (see chapter 6) has been published as

[191] Fazhan Shi, Xing Rong, Nanyang Xu, Ya Wang, Jie Wu, Bo Chong, Xinhua Peng, Juliane Kniepert, Rolf-Simon Schoenfeld, Wolfgang Harneit, Mang Feng, and Jiangfeng Du:
Room-Temperature Implementation of the Deutsch-Jozsa Algorithm with a Single Electronic Spin in Diamond, Physical Review Letters **105**, 040504 (2010)

Finally, some experimental results and theory regarding field frequency locked magnetic sensing using a single NV center (see chapter 7) can be found in

[192] Rolf Simon Schoenfeld and Wolfgang Harneit:
Real Time Magnetic Field Sensing and Imaging Using a Single Spin in Diamond, Physical Review Letters **106**, 030802 (2011)